

Investigation on Formability of Tailor Welded Blanks prepared by Friction Stir Welding Process

A DISSERTATION

SUBMITTED IN PARTIAL FULFILLMENT OF THE REQUIREMENTS FOR THE
AWARD OF THE DEGREE

OF

MASTER OF TECHNOLOGY

IN

PRODUCTION AND INDUSTRIAL ENGINEERING

Submitted by

Subhajit Konar

2K17/PIE/15

Under the supervision of

Dr. Vijay Gautam

Professor

(Mechanical Engineering Department)



DEPARTMENT OF MECHANICAL ENGINEERING

DELHI TECHNOLOGICAL UNIVERSITY

(Formerly Delhi College of Engineering)

Bawana Road, Delhi-110042

JULY, 2019

DELHI TECHNOLOGICAL UNIVERSITY
(Formerly Delhi College of Engineering)
Bawana Road, Delhi-110042

CANDIDATE'S DECLARATION

I, **Subhajit Konar**, Roll No. 2K17/PIE/15 of M.Tech (Production and Industrial Engineering), hereby certify that the project Dissertation titled “ **Investigation on Formability of Tailor Welded Blanks prepared by Friction Stir Welding Process**” which is submitted by me to the Department of Mechanical Engineering, Delhi Technological University, Delhi in partial fulfilment of the requirement for the award of the degree of the Master of Technology, is original and not copied from any source without proper citation. This work has not previously formed the basis for the award of any Degree, Diploma Associateship, Fellowship or other similar title or recognition.

Place: Delhi

Subhajit Konar

Date:

2K17/PIE/15

M.Tech (Production and Industrial Engineering)

Delhi Technological University

MECHANICAL ENGINEERING DEPARTMENT

DELHI TECHNOLOGICAL UNIVERSITY

(Formerly Delhi College of Engineering)

Bawana Road, Delhi-110042

CERTIFICATE

I hereby certify that the Project Dissertation titled “**Investigations on Formability of Tailor Welded Blanks Prepared by Friction Stir Welding Process**” which is submitted by **SUBHAJIT KONAR**, 2K17/PIE/15, Mechanical Engineering Department, Delhi Technological University, Delhi in partial fulfilment of the requirement for the award of the degree of Master of Technology, is a record project work carried out by the student under my supervision. To the best of my knowledge this work has not been submitted in part or full for any Degree or Diploma to this University or elsewhere.

Place: Delhi

Date:

Dr. VIJAY GAUTAM**SUPERVISOR**

Professor

Department of Mechanical Engineering

Delhi Technological University

ACKNOWLEDGEMENT

First of all, I wish to convey my deep gratitude and sincere thanks to my M.Tech supervisor, Prof. Vijay Gautam for giving me an opportunity to pursue this research work at Delhi Technological University. I feel very fortunate that I got an opportunity to work under his supervision. His guidance and support helped me during every single step of my carrier. I learned many technical aspects from him along with the living morals to lead a fruitful life. He is a great teacher, motivator, honest and a very gentleman. Without his technical guidance, inspiration, constant encouragement it wouldn't be possible for me to achieve the success. Discussions with him always have been a source of great motivation to take up challenges and overcome them. It has been a real pleasure working with him.

I would like to thank Sh. Om Prakash, Sh. Tek Chand, Sh. Virender Sharma, Sh. Net Ram, Sh. Girish Anand, Sh. Sanjay Gupta, Sh. Lallan for the guidance and invaluable help throughout my research work.

I express my gratitude towards my dear friends for their presence in DTU throughout my two years of journey. It was a pleasant, inspiring and a memorable experience to me.

I express my unfailing love and gratitude towards my caring father Jagannath Konar, and my loving mother Sandhya Konar for their constant prayers to almighty and blessing me to pursue M.Tech, without their support it was impossible for me to carry out the entire journey. I would like to thank to all of my brothers and sisters for their love and support.

SUBHAJIT KONAR

2K17/PIE/15

M.Tech (Production and Industrial Engineering)

Delhi Technological University

ABSTRACT

Tailored Welded Blank (TWB) is prepared by welding two or more blanks having same or different thickness of different mechanical properties or coatings in a single plane prior to forming. Welding can be performed as per manufacturer choice. In this project Friction Stir Welding process has been chosen to weld the Aluminium blank. Aluminium alloys that have been used for the preparation of TWBs are AA5083 and AA6082, both having same thickness. After the fabrication of TWBs, testing has been performed on the specimens to check the mechanical properties of the welded blank Tensile properties, formability of the sheet has been recorded and modelling and simulation has been carried out to predict the formability of the Tailor Welded blanks. Low density and high specific energy absorption performance and good specific strength are its most important properties. Aluminium is also resistant to corrosion and can be recycled to its pure form. To prepare a TWB, it is quite cumbersome to weld Aluminium blanks by conventional welding processes. Friction stir welding (FSW) came with the solution regarding joining aluminium alloys as a solid-state joining process. Noor Zaman Khan et al. 2017 had studied the mechanical and microstructural behaviour of friction stir welded similar and dissimilar blanks of different aluminium alloys, reveals high hardness due to grain refinement at the stirring zone with a sustainable joint efficiency. The FSW process incorporates joining by material locking due to its stirring mechanism. FSW, being a solid-state joining process, avoids the various defects due to formation of porosity, blow holes, poor solidification etc. The excessive plastic deformation at elevated temperature during FSW produces equiaxed recrystallized grains which are responsible for the higher strength and lower formability of the weld zone. To enhance the formability of the Tailor Welded Blanks, warm forming is a better option.

TABLE OF CONTENTS

Title	Page No.
Candidate's Declaration	ii
Certificate	iii
Acknowledgement	iv
Abstract	v
Table of Contents	vi
List of Figures	ix
List of Tables	xiv
Chapter 1 INTRODUCTION	1
1.1 Aluminium alloys	2
1.2 Aluminium alloys application in automobile body parts	5
1.3 Sheet materials for weight reduction of autobody	7
1.4 Aluminium alloys application in TWBs	9
1.5 Characteristics of aluminium alloy sheets	10
1.6 Work hardening of aluminium alloys	10
1.6.1 Stages of work hardening	11
1.6.2 Precipitation strengthening	12
1.6.3 Annealing	13
1.7 Fundamental principles of friction stir welding	15
1.7.1 Heat generation	15
1.7.2 Material flow	16
1.8 Forming limit diagram	19
1.8.1 Important material parameters which affect formability	21
Chapter 2 REVIEW OF LITERATURE AND OBJECTIVES OF THE PRESENT WORK	22
2.1 Literature review	22
2.2 Research gap & motivation	31
Chapter 3 METHODOLOGY	32

Title	Page No.
3.1 Material selection	32
3.2 Tensile properties	32
3.3 Finding of annealing temperature of aa6082-T6	34
3.4 Annealing of aa6082-T6 sheets	34
3.5 Pilot experiment to get the optimum speed, feed for FSW	34
3.5.1 Analysis of the input data for FSW and Tensile properties of Weld beads	35
3.5.2 Taguchi Method	35
3.6 Friction Stir Welding of aa5083-O and aa6082- O	37
3.6.1 Friction Stir Welding machine	37
3.6.2 Friction Stir Welding Tool	39
3.6.3 Process Parameters	39
3.7 Annealing of welded sheets	40
3.8 Tensile properties of annealed and non-annealed welded sheets	40
3.9 Microstructure preparation of the specimen	40
3.9.1 Mounting of the specimen	40
3.9.2 Polishing	41
3.10 Micro-hardness measurement of the FSW sheet prior and after annealing	41
3.11 Preparation of specimen for stretch forming operation	42
3.11.1 Laser cutting of the samples	43
3.12 Design and fabrication of die-punch-holder setup for formability test	45
3.12.1 Stretch forming operation	45

3.12.2 Dome height measurement of the formed sheets	46
3.13 Simulation of the stretch forming operation	46
3.14 Measurement of the major and minor diameter of the ellipse and forming limit diagram	46
3.15 Modelling of Blank, Die-Punch-Holder setup	47
Chapter 4 RESULT AND DISCUSSION	48
4.1 Tensile properties	48
4.2 Residual stress of the sheet before and after annealing	51
4.3 Taguchi analysis	53
4.4 ANOVA results	56
4.5 Micro hardness testing result before annealing of welded sheets	56
4.6 Microstructure of the different parts of the FSW non-annealed sheet	58
4.6.1 Microstructure of the different parts of the FSW non-annealed sheet	59
4.6.2 Microstructure of the different parts of the FSW annealed sheet	60
4.7 FLD sample dome height	61
4.8 Formability of annealed and non-annealed FSW sheets	63
4.9 FEA Results	65
Chapter 5 CONCLUSIONS	72
REFERENCES	74

LIST OF FIGURES

Figure No.	Caption	Page No.
Figure1.1	Growth of Aluminium in car body application	5
Figure 1.2	Social and global environmental requirements for automobile	6
Figure 1.3	Countermeasures of low fuel consumption	7
Figure 1.4	Standard of selection of sheet materials for autobody	8
Figure1.5	Deformation behaviour of metal sheet in press-forming and corresponding properties as related to formability	9
Figure 1.6	Application of a TWB in inner door panel for an automobile	10
Figure1.7	Stress-strain curves for single crystals of various orientations. Crystal D, having one active slip system, shows work hardening stages I, II and III. In the multi slip orientations A-C, the material goes directly into stage II.	11
Figure 1.7	Phase diagram showing the solubility of Mg and Si as a function of temperature represented by the phase Mg ₂ Si.	12
Figure 1.8	Modified sketch of strength evolution during artificial ageing of an AlMgSi-alloy	13
Figure 1.9	Effect of annealing on the structure and mechanical property changes of a cold-worked metal	14
Figure 1.10	Three incompressible flow fields: a) rigid body rotation, b) uniform translation, c) ring vortex, d) combination of the three flow fields.	17
Figure 1.11	Scheme of tool parameters	17
Figure 1.12	Circles deformed into ellipses in different modes of deformation	20
Figure 1.13	A typical forming limit diagram	20
Figure 3.1	Tensile testing specimen as per ASTM-E8M standard	33

Figure 3.3	Tensile testing specimen cut from the annealed and non-annealed sheet	33
Figure 3.4	Friction Stir Welding Machine	35
Figure 3.5	Friction Stir Welding of AA5083-O and AA6082-O	38
Figure 3.6	1 st angle projection of the FSW tool	38
Figure 3.7	Mounted Friction Stir Welded specimen	39
Figure 3.8	polishing station and Microscope	40
Figure 3.9	Duramin 40 Micro-Hardness tester	41
Figure 3.10	Output screen of the hardness measurement	42
Figure 3.11	computerized Laser marking setup along with its operation	42
Figure 3.12	LASER marked specimen along with the parameter control screen	43
Figure 3.13	Laser cutting machine	43
Figure 3.14	Laser cut samples for formability test	44
Figure 3.14	Punch-Die-Blank Holder setup in a 100 Ton hydraulic press	44
Figure 3.15	Dome height measurement with the help of Vernier height gauge	45
Figure 3.16	Measurement of major and minor diameter of the ellipse	46
Figure 3.17	Assemble of the parts required for formability test	47
Figure 4.1	True Stress vs True Strain plot	47
Figure 4.2	True Stress vs True Strain plot	48
Figure 4.3	True Stress vs True Strain plot	49
Figure 4.4	True Stress vs True Strain plot	50
Figure 4.5	True Stress vs True Strain plot	50
Figure 4.6	Residual Stress measurement before and after the Friction Stir Welding	51
Figure 4.7	Residual Stress vs Transverse Distance to the weld bead	51
Figure 4.8	Debye ring mapping to evaluate residual stresses in the bend samples using Cos α	52
Figure 4.9	Graphical plot of mean of S/N ratios -TTS and TRS for UTS	52

Figure 4.9	Graphical plot of mean of S/N ratios -TTS and TRS for % Elongation (S)	54
Figure 4.10	Micro-hardness Testing report	55
Figure 4.11	Hardness distribution on a cross-section of a Friction Stir Welded non-annealed sheet	57
Figure 4.12	Hardness distribution on a cross-section of a Friction Stir Welded annealed sheet	58
Figure 4.13	Microstructure of AA5083	58
Figure 4.14	Microstructure of AA6082	59
Figure 4.15	Microstructure of weld bead	59
Figure 4.16	Microstructure of AA5083	59
Figure 4.17	Microstructure of AA6082	60
Figure 4.18	Microstructure of weld bead	60
Figure 4.19	Sheet after forming operation	60
Figure 4.20	clustered column representation of the annealed and non-annealed sheets during experimentation	61
Figure 4.21	clustered column representation of the annealed and non-annealed sheets during FEA simulation	62
Figure 4.22	Forming limit Diagram of AA5083-O and AA6082-O annealed sheet	62
Figure 4.23	Forming limit Diagram of AA5083-O and AA6082-O non-annealed sheet	63
Figure 4.24	combined Forming limit Diagram of AA5083-O and AA6082-O	63
Figure 4.25	Forming limit Diagram of AA5083-O and AA6082-O after annealing	64
Figure 4.26	Forming limit Diagram of AA5083-O and AA6082-O after annealing	65
Figure 4.27	Variation of Von-Mises stress at different points across the width, (b) Contours of formed sheet for a punch profile radius of 100mm	65

Figure 4.28	Variation of Von-Mises stress at different points across the width, (b) Contours of formed sheet for a punch profile radius of 100mm	66
Figure 4.29	Variation of Von-Mises stress at different points across the width, (b) Contours of formed sheet for a punch profile radius of 100mm	66
Figure 4.30	Variation of Von-Mises stress at different points across the width, (b) Contours of formed sheet for a punch profile radius of 100mm	66
Figure 4.31	Variation of Von-Mises stress at different points across the width, (b) Contours of formed sheet for a punch profile radius of 100mm	67
Figure 4.32	Variation of Von-Mises stress at different points across the width, (b) Contours of formed sheet for a punch profile radius of 100mm	67
Figure 4.33	Variation of Max. In-Plane Strain at different points across the width, (b) Contours of formed sheet for a punch profile radius of 100mm	67
Figure 4.34	Variation of Max. In-Plane Strain at different points across the width, (b) Contours of formed sheet for a punch profile radius of 100mm	68
Figure 4.35	Variation of Max. In-Plane Strain at different points across the width, (b) Contours of formed sheet for a punch profile radius of 100mm	68
Figure 4.36	Variation of Max. In-Plane Strain at different points across the width, (b) Contours of formed sheet for a punch profile radius of 100mm	68
Figure 4.37	Variation of Max. In-Plane Strain at different points across the width, (b) Contours of formed sheet for a punch profile radius of 100mm	69
Figure 4.38	Variation of Max. In-Plane Strain at different points across the width, (b) Contours of formed sheet for a punch profile radius of 100mm	69

Figure 4.39	Variation of Min. In-Plane Strain at different points across the width, (b) Contours of formed sheet for a punch profile radius of 100mm	69
Figure 4.40	Variation of Min. In-Plane Strain at different points across the width, (b) Contours of formed sheet for a punch profile radius of 100mm	70
Figure 4.41	Variation of Min. In-Plane Strain at different points across the width, (b) Contours of formed sheet for a punch profile radius of 100mm	70
Figure 4.42	Variation of Min. In-Plane Strain at different points across the width, (b) Contours of formed sheet for a punch profile radius of 100mm	70
Figure 4.43	Variation of Min. In-Plane Strain at different points across the width, (b) Contours of formed sheet for a punch profile radius of 100mm	71
Figure 4.44	Variation of Min. In-Plane Strain at different points across the width, (b) Contours of formed sheet for a punch profile radius of 100mm	71

LIST OF TABLES

Table No.	Caption	Page No.
Table 3.1	Chemical composition of AA5083 and AA6082	32
Table 3.2	Process parameters and their levels	36
Table 3.3	Standard L ₉ Orthogonal Array	36
Table 3.4	Experimentation control log using Orthogonal Array L ₉	37
Table 3.5	Specification of the Friction Stir Welding machine	38
Table 3.6	Specification of Friction Stir Welding Tool	39
Table 3.7	Specification of LASER cutting machine	44
Table-4.1	mechanical properties of AA5083-O	48
Table-4.2	mechanical properties of AA6082-T6	49
Table-4.3	mechanical properties of AA6082-T6 at different annealing temperature	51
Table 4.4	Nomenclature for the term used in Residual Stress plot	52
Table 4.5	Experimental Results for the Ultimate Tensile Strength, % Elongation (S) and % Elongation (I)	53
Table 4.6	S/N ratio for different experimental run	53
Table 4.7	The average of the signal to noise ratios for UTS	54
Table 4.8	average of the signal to noise ratios for % Elongation (S)	54
Table 4.9	The average of the signal to noise ratios for % Elongation (I)	55
Table 4.10	Optimum values of the Input parameters and their optimized values	56
Table 4.11	Analysis of variance for TTS and TRS	56
Table 4.12	FLD Sample Dome height	61

CHAPTER 1

INTRODUCTION

Tailored Welded Blank (TWB) is prepared by welding two or more blanks having same or different thickness of different mechanical properties or coatings in a single plane prior to forming. TWB allows the design engineers to combine and locate material's best properties within the part where they are needed. This offers the optimum characteristics by combining the required properties of the blanks and enables the design to be perfectly engineered. It has become an essential mass production technology which reduces the weight of the finished products by eliminating number of reinforcements and stiffeners. [1] According to the Corporate Average Fuel Economy 2025 (CAFE) regulations in the United States, first enacted by the U.S. Congress in 1975, in the wake of the Arab Oil Embargo and were intended to improve the average fuel economy of cars and light trucks (trucks, vans and sport utility vehicles) produced for sale in the United States) mass optimization for components and subsystems can be achieved by using of low density ultra-high strength alloys, such as aluminium alloys, which provides good formability and crashworthiness. Low density and high specific energy absorption performance and good specific strength are its most important properties. Aluminium is also resistant to corrosion and can be recycled to its pure form. [2] To prepare a TWB, it is quite cumbersome to weld Aluminium blanks by conventional welding processes. Friction stir welding (FSW) came with the solution regarding joining aluminium alloys as a solid-state joining process [3]. Noor Zaman Khan et al. 2017 had studied the mechanical and microstructural behaviour of friction stir welded similar and dissimilar blanks of different aluminium alloys, reveals high hardness due to grain refinement at the stirring zone with a sustainable joint efficiency. [4] The FSW process incorporates joining by material locking [5] due to its stirring mechanism. FSW, being a solid-state joining process, avoids the various defects due to formation of porosity, blow holes, poor solidification etc. The excessive plastic deformation at elevated temperature during FSW produces equiaxed recrystallized grains which are responsible for the higher strength and lower formability of the weld zone [6]. To enhance the formability of the Tailor Welded Blanks, warm forming is a better option.

1.1 ALUMINIUM ALLOYS

The unique combinations of properties provided by aluminium and its alloys make aluminium one of the most versatile, economical, and attractive metallic materials for a broad range of uses—from soft, highly ductile wrapping foil to the most demanding engineering applications. Aluminium alloys are second only to steels in use as structural metals. Aluminium has a density of only 2.7 g/cm³, approximately one-third as much as steel (7.83 g/cm³). One cubic foot of steel weighs about 490 lb; a cubic foot of aluminium, only about 170 lb. Such light weight, coupled with the high strength of some aluminium alloys (exceeding that of structural steel), permits design and construction of strong, light weight structures that are particularly advantageous for anything that moves—space vehicles and aircraft as well as all types of land- and water-borne vehicles. Aluminium resists the kind of progressive oxidization that causes steel to rust away. The exposed surface of aluminium combines with oxygen to form an inert aluminium oxide film only a few ten-millionths of an inch thick, which blocks further oxidation. And, unlike iron rust, the aluminium oxide film does not flake off to expose a fresh surface to further oxidation. If the protective layer of aluminium is scratched, it will instantly reseal itself. The thin oxide layer itself clings tightly to the metal and is colourless and transparent—invisible to the naked eye. The discoloration and flaking of iron and steel rust do not occur on aluminium. Appropriately alloyed and treated, aluminium can resist corrosion by water, salt, and other environmental factors, and by a wide range of other chemical and physical agents. The corrosion characteristics of aluminium alloys are examined in the section “Effects of Alloying on Corrosion Behaviour” in this article.

Aluminium surfaces can be highly reflective. Radiant energy, visible light, radiant heat, and electromagnetic waves are efficiently reflected, while anodized and dark anodized surfaces can be reflective or absorbent. The reflectance of polished aluminium, over a broad range of wave lengths, leads to its selection for a variety of decorative and functional uses. Aluminium typically displays excellent electrical and thermal conductivity, but specific alloys have been developed with high degrees of electrical resistivity. These alloys are useful, for example, in high-torque electric motors. Aluminium is often selected for its electrical conductivity, which is nearly twice that of copper on an equivalent weight basis. The requirements of high conductivity and mechanical strength can be met by use of long-line, high-voltage, aluminium steel-cored reinforced transmission cable. The thermal conductivity of aluminium alloys, about 50 to 60% that of copper, is advantageous in heat exchangers, evaporators, electrically heated appliances and utensils, and automotive cylinder heads and radiators. Aluminium is nonferromagnetic, a property of importance in the electrical and electronics industries. It is nonpyrophoric, which is important in applications involving inflammable or explosive-materials handling or exposure. Aluminium is also non-toxic and is routinely used in containers for food and beverages. It has an attractive appearance in its natural finish, which can be soft and lustrous or bright and shiny. It can be

virtually any colour or texture. The ease with which aluminium may be fabricated into any form is one of its most important assets. Often it can compete successfully with cheaper materials having a lower degree of workability. The metal can be cast by any method known to foundrymen. It can be rolled to any desired thickness down to foil thinner than paper. Aluminium sheet can be stamped, drawn, spun, or roll formed. The metal also may be hammered or forged. Aluminium wire, drawn from rolled rod, may be stranded into cable of any desired size and type. There is almost no limit to the different profiles (shapes) in which the metal can be extruded. Different types of Aluminium alloys are described below:

1xxx Series. Aluminium of 99.00% or higher purity has many applications, especially in the electrical and chemical fields. These grades of aluminium are characterized by excellent corrosion resistance, high thermal and electrical conductivities, low mechanical properties, and excellent workability. Moderate increases in strength may be obtained by strain hardening. Iron and silicon are the major impurities.

2xxx Series. Copper is the principal alloying element in 2xxx series alloys, often with magnesium as a secondary addition. These alloys require solution heat treatment to obtain optimum properties; in the solution heat-treated condition, mechanical properties are similar to, and sometimes exceed, those of low-carbon steel. In some instances, precipitation heat treatment (aging) is employed to further increase mechanical properties. This treatment increases yield strength, with attendant loss in elongation; its effect on tensile strength is not as great. The alloys in the 2xxxseries do not have as good corrosion resistance as most other aluminium alloys, and under certain conditions they may be subject to intergranular corrosion. Therefore, these alloys in the form of sheet usually are clad with a high-purity aluminium, a magnesium-silicon alloy of the 6xxx series, or an alloy containing 1% Zn. The coating, usually from 2 to 5% of the total thickness on each side, provides galvanic protection of the core material and thus greatly increases resistance to corrosion. Alloys in the 2xxxseries are particularly well suited for parts and structures requiring high strength-to-weight ratios and are commonly used to make truck and aircraft wheels, truck suspension parts, aircraft fuselage and wing skins, structural parts, and those parts requiring good strength at temperatures up to 150 °C (300 °F). Figure 1 shows the relationships between some of the more commonly used alloys in the 2xxx series.

3xxx Series. Manganese is the major alloying element of 3xxx series alloys. These alloys generally are non-heat-treatable but have about 20% more strength than 1xxx series alloys. Because only a limited percentage of manganese (up to about 1.5%) can be effectively added to aluminium, manganese is used as a major element in only a few alloys. However, one of these, the popular 3003 alloy, is widely used as a general-purpose alloy for moderate-strength applications requiring good workability.

4xxx Series. The major alloying element in 4xxxseries alloys is silicon, which can be added in sufficient quantities (up to 12%) to cause substantial lowering of the melting range without producing brittleness. For this reason, aluminium-silicon alloys are used in welding wire and as brazing alloys for joining aluminium, where a lower melting range than that of the base metal is required. Most alloys in this series are non-heat treatable, but when used in welding heat-treatable alloys, they pick up some of the alloying constituents of the latter and so respond to heat treatment to a limited extent. The alloys containing appreciable amounts of silicon become dark grey to charcoal when anodic oxide finishes are applied and hence are in demand for architectural applications. Alloy 4032 has a low coefficient of thermal expansion and high wear resistance; thus, it is well suited to production of forged engine pistons.

5xxx Series. The major alloying element in 5xxx series alloys is magnesium. When it is used as a major alloying element or with manganese, the result is a moderate-to-high-strength work hardenable alloy. Magnesium is considerably more effective than manganese as a hardener, about 0.8% Mg being equal to 1.25% Mn, and it can be added in considerably higher quantities. Alloys in this series possess good welding characteristics and good resistance to corrosion in marine atmospheres. However, certain limitations should be placed on the amount of cold work and the safe operating temperatures permissible for the higher-magnesium alloys (over ~3.5% for operating temperatures above ~65 °C, or 150 °F) to avoid susceptibility to stress-corrosion cracking. Figure 2 shows the relationships between some of the more commonly used alloys in the 5xxx series.

6xxx Series. Alloys in the 6xxx series contain silicon and magnesium approximately in the proportions required for formation of magnesium silicide (Mg_2Si), thus making them heat treatable. Although not as strong as most 2xxx and 7xxx alloys, 6xxx series alloys have good formability, weldability, machinability, and corrosion resistance, with medium strength. Alloys in this heat-treatable group may be formed in the T4 temper (solution heat treated but not precipitation heat treated) and strengthened after forming to full T6 properties by precipitation heat treatment. Figure 3 shows the relationships between some of the more commonly used alloys in the 6xxx series.

7xxx Series. Zinc, in amounts of 1 to 8%, is the major alloying element in 7xxxseries alloys, and when coupled with a smaller percentage of magnesium results in heat-treatable alloys of moderate to very high strength. Usually other elements, such as copper and chromium, are added in small quantities. Dilute additions of scandium also improve properties. 7xxx series alloys are used in airframe structures, mobile equipment, and other highly stressed parts. Higher strength 7xxx alloys exhibit reduced resistance to stress corrosion cracking and are often utilized in a slightly overaged temper to provide better combinations of strength, corrosion resistance, and fracture

toughness. Figure 4 shows the relationships between some of the more commonly used alloys in the 7xxx series.

8xxx series alloys constitute a wide range of chemical compositions. For example, improved elevated-temperature performance is achieved through the use of dispersion-strengthened Al-Fe-Ce alloys (e.g., 8019) or Al-Fe-V-Si alloys (e.g., 8009) made by powder metallurgy processing. Lower density and higher stiffness can be achieved in lithium-containing alloys (e.g., 8090). The latter alloy, which is precipitation hardenable, has replaced medium-to-high strength 2xxx and 7xxx alloys in some aircraft/aerospace applications (e.g., helicopter components).

1.2 ALUMINIUM ALLOYS APPLICATION IN AUTOMOBILE BODY PARTS

The social and global environmental requirements for automobile have become strict and difficult to accomplish. They are natural resource saving, lower energy consumption, countermeasures against environment pollution and driving safety in addition to comfortable driving conditions. Especially the low energy consumption for energy saving and exhaust volume reduction of CO₂ gas against the global warming issue is an urgent and problem. The efficiency improvement of engine and driving system, the reduction of running resistance and the weight reduction of autobody are main countermeasures to lower fuel consumption. Concerning the weight reduction, the size down of autobody, the change of body structure and the replacing of conventional body materials with lighter weight ones are available ways.

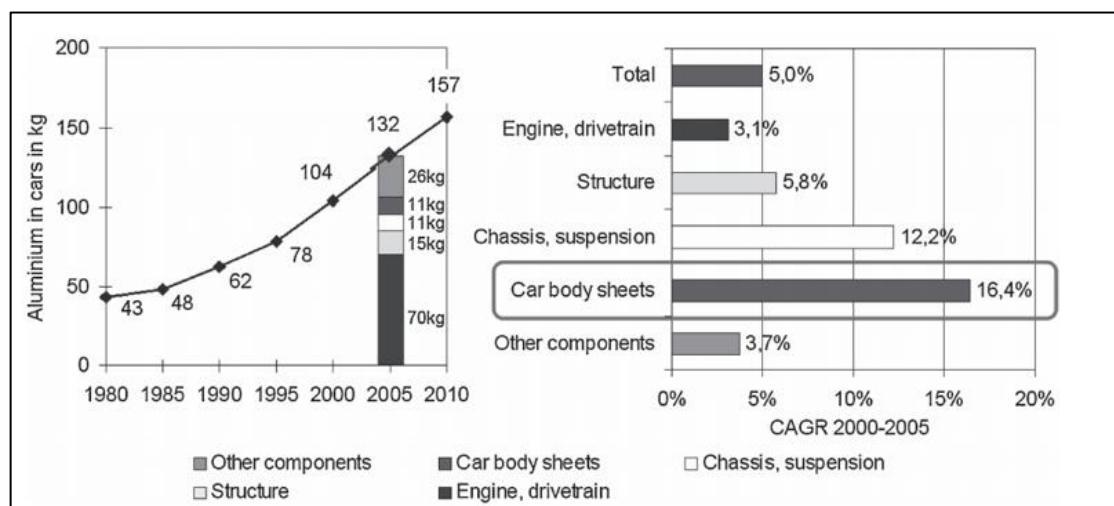


Figure 1.1 Growth of Aluminium in car body application

The size down of automobile is the best way for weight reduction, but the size has a tendency to become larger because of ensuring the safety and customers' demand. Furthermore, the installation of air-conditioner and other accessories makes a car heavier. Regarding passenger car,

the change of body structure from frame type to frameless monocoque body resulted in weight reduction. Japanese automobile companies started to apply high strength steel sheets (HS) practically to outer panels of autobody with two oil crises as a turning point. Afterward several kinds of HS with good formability were developed and the use ratio of HS has increased more and more. In order to achieve the weight reduction for the new and severe regulation of fuel consumption it is necessary to replace conventional materials with new lighter weight materials. In this report the present status of development and application of sheet materials for weight reduction of autobody is introduced and the problems of these materials in sheet forming are discussed.

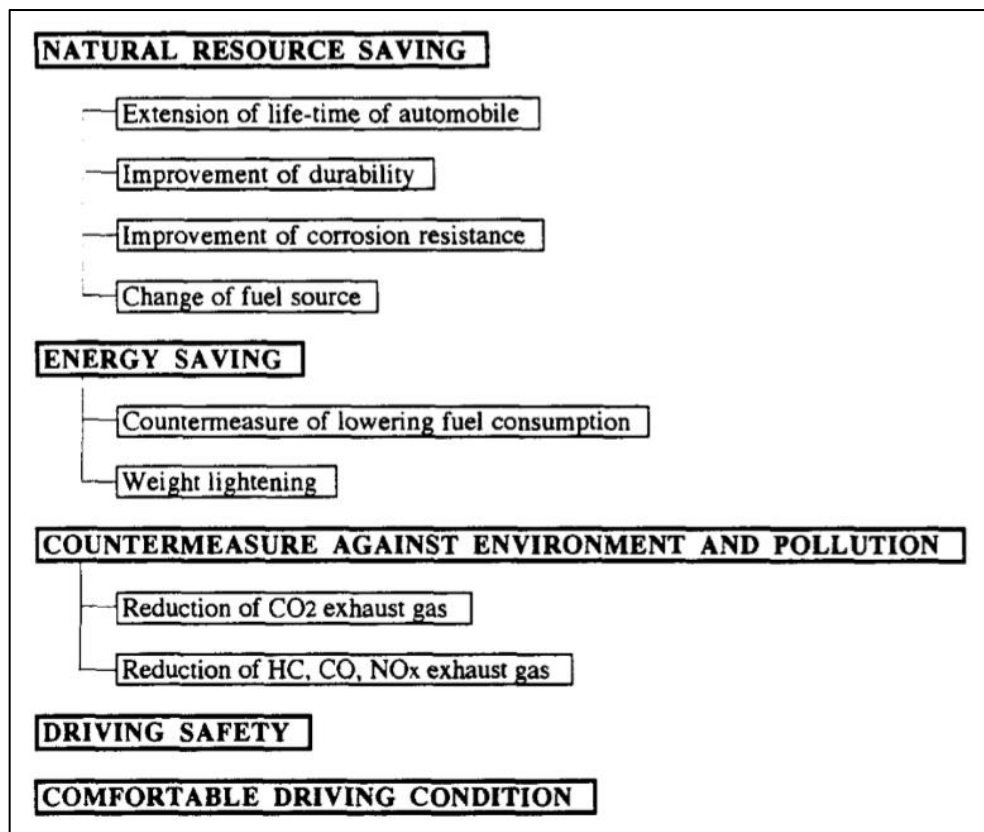


Figure 1.2 Social and global environmental requirements for automobile

The efficiency improvement of engine and driving system, the reduction of running resistance and the weight reduction of autobody are main countermeasures to lower fuel consumption.

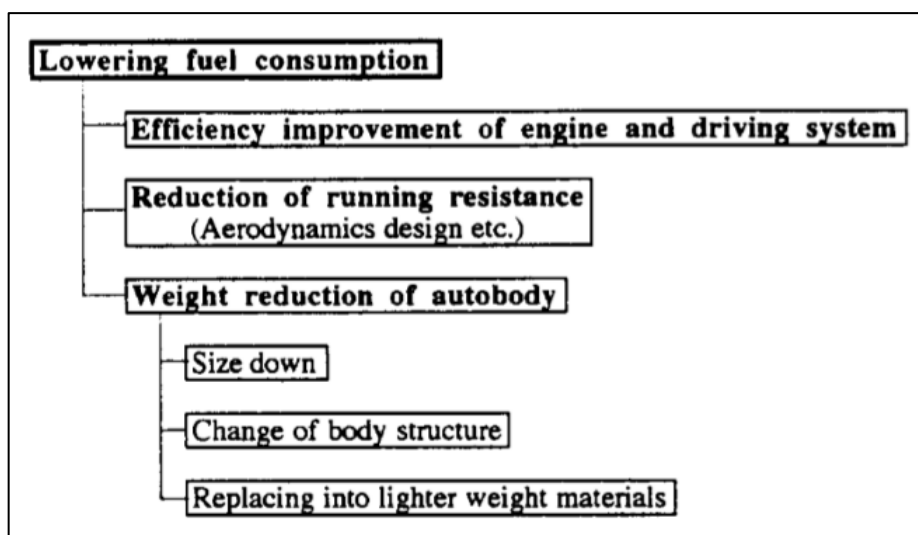


Figure 1.3 Countermeasures of low fuel consumption

1.3 SHEET MATERIALS FOR WEIGHT REDUCTION OF AUTOBODY

Practical application of aluminium alloys to automobile is expected so much as lighter weight material. The application of aluminium alloys to engine cylinder and wheel is advanced, and the average weight ratio of aluminium parts is 5 to 7 % of total weight of mass-produced passenger cars in Japan. With regard to skin panels the use of aluminium alloy sheets to autobody parts have been increased since the first application of Al-Mg-Zn alloy in 1985. Some separable components such as hood (both outer and inner), front fender and sun-roof panels of several passenger cars are made of aluminium alloy sheets. But as the price of aluminium alloy sheets is more expensive than steel sheets, aluminium alloys are applied only to special types of passenger cars. A car which white body is fully made of aluminium alloys have been on the market. The application of extruded shapes of aluminium alloys to structural parts, moreover, is under development

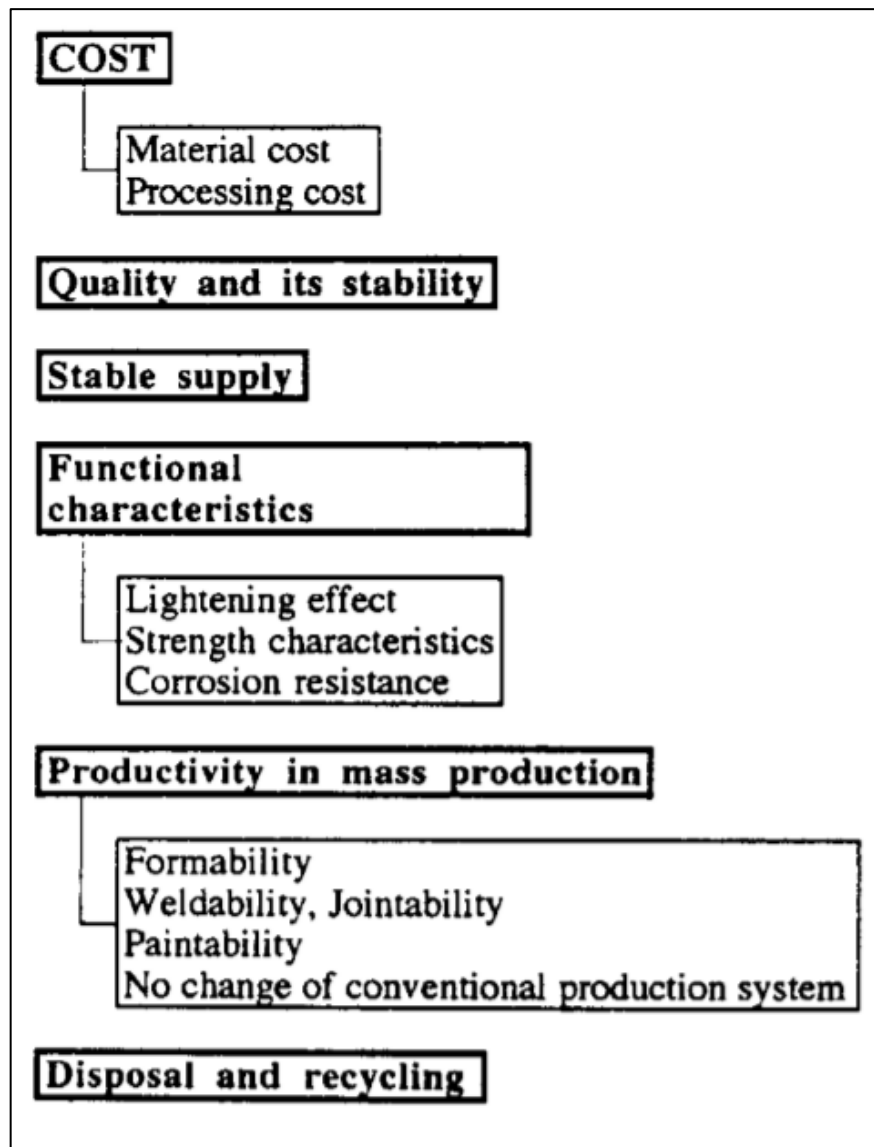


Figure 1.4 Standard of selection of sheet materials for autobody

Each of these materials have their own advantages and disadvantages. 1) cost of materials and processing, 2) quality and its stability, 3) stable supply, 4) functional characteristics such as lightening effect, strength and so on, 5) productivity in processes as forming, welding and so on, and 6) disposal and recycling after disuse. Even from the viewpoint of formability of sheet materials, there are many indices of material properties for selecting. In press forming of large-sized complicated parts such as automotive skin panels, it is necessary to examine various unfavourable phenomena during forming process and to evaluate the overall effect of material properties and forming techniques on forming performance. According to the examination of forming defects and their countermeasures in press shop, Yoshida proposed to distinguish the fitting behaviour, the shape fixation and the fracture behaviour for better understanding of deformation behaviour of metal sheets [7]. Corresponding to this, the formability of sheet metal

should be evaluated by three properties, fitability, shape fixability and fracture resistance, which compose the overall formability.

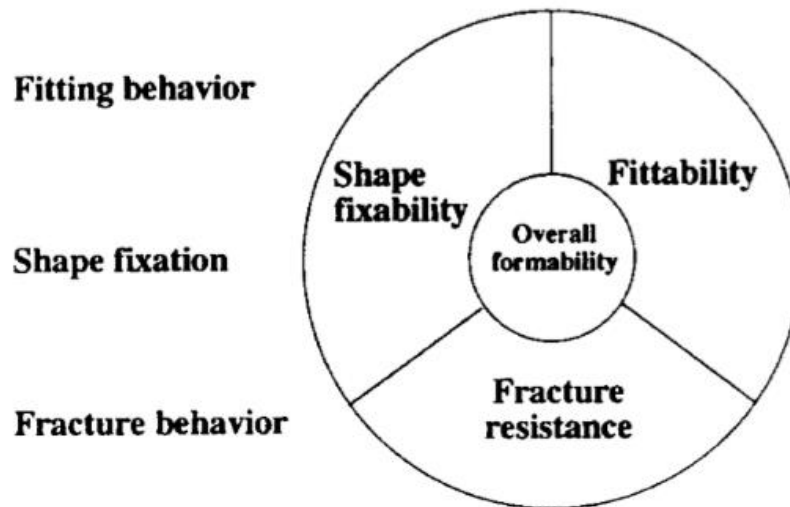


Figure1.5 Deformation behaviour of metal sheet in press-forming and corresponding properties as related to formability [7]

The fracture resistance means the formability in a narrow sense. The formability based on fracture resistance is classified into deep drawability, stretch ability, stretch flange ability and bendability [7]. The fittability means the deviation degree of a formed part from the designed shape, in other words, the degree of geometrical shape defect as wrinkle and surface deflection. The fixability means the fixation degree of shape and size of a formed part after stamping. In the actual stamping springback and small surface deflection appear by the elastic recovery due to the release of residual stresses, the influencing factors of material properties on main unfavourable phenomena observed in forming operation [8]. The sheet metals should be selected from the viewpoint of overall formability.

1.4 ALUMINIUM ALLOYS APPLICATION IN TWBS

Aluminium has already established itself in the car industry for many years. The current trend in automotive and aerospace industry is to develop such a design which will minimize weight of the vehicle results in less consumption of energy and environmental effect of future vehicle [8]. It is used for body structures, closures and exterior attachments such as cross beams, doors and bonnets. Pure aluminium bodies have been developed and implemented. They are mainly used for luxury cars such as Audi A8, and some niche vehicles, such as BMW Z8, because of their comparatively high material and production cost. Nevertheless, Aluminium offers many

advantages and new possibilities and will play an increasingly role for the car industry in future. The application of TWBs for vehicle parts is subjected to a wide area of demands, depending on specific requirements. Among other things, this includes economic effectiveness, safety, recyclability and lightweight performance. The example of application of a TWB made of aluminium alloys with two different thicknesses is shown in Fig.3.

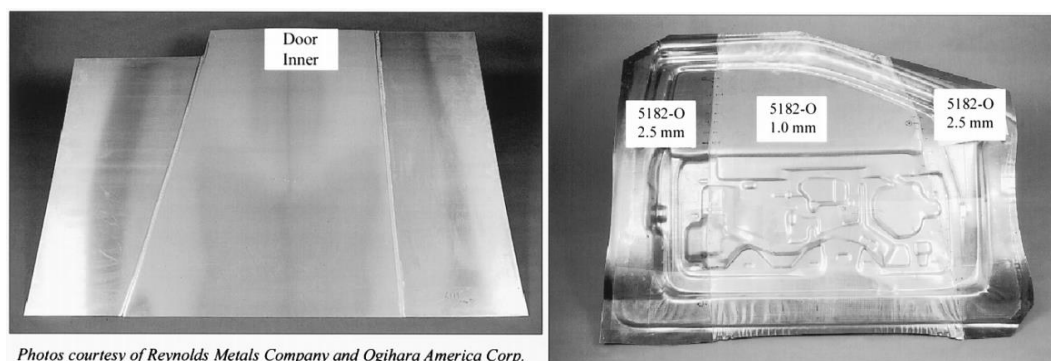


Figure 1.6 Application of a TWB in inner door panel for an automobile [8]

1.5 CHARACTERISTICS OF ALUMINIUM ALLOY SHEETS

Aluminium alloys for autobody use are mainly three types of alloying element composition. Heat-treatable 2000 series Al-Cu alloys, 6000 series Al-Mg-Si alloys and non-heat-treatable 5000 series Al-Mg alloys have been used in autobody. In USA 2000 series Al-Cu alloys are used with 5000 series Al-Mg alloys, but in Japan 2000 series alloys have not been applied because of poor anti-corrosion resistance. The features of mechanical properties of aluminium alloys for stamping use are in general as follows; 1) Strength level (YP, TS) is lower than that of steels 2) Elastic constant (Young's modulus), E, is about one-third of steel 3) Elongation, particularly local elongation, is small 4) Discontinuous deformation phenomena such as yield-point elongation and jerky flow due to P-L effect exist 5) Plastic anisotropy, r value, is low (under 1.0) 6) Relatively soft and easy to be damaged on the surface For the reasons above-mentioned, it can be estimated that aluminium alloy sheets are hard-formable materials in press forming with respect to steel sheets. In aluminium companies' new kinds of alloy sheets with high strength and high elongation for autobody use are being developed, especially Al-Mg 5000 series alloys. Figs. 26 and 27 show the relationships between total elongation and tensile strength (TS) of aluminium alloys developed recently for autobody parts by Japanese aluminium companies. For 5000 series Al-Mg alloys the total elongation ranges up to 36 % and TS ranges up to 300 MPa. For 6000 series Al-Mg-Si the total elongation ranges up to 32 % and TS ranges up to 290 MPa.

1.6 WORK HARDENING OF ALUMINIUM ALLOYS

Work hardening, also known as strain hardening or deformation hardening, is a phenomenon where the strength of a material increases during plastic deformation. In this section, first a

description of the impacts of work hardening on the material response. Work hardening is strongly related to the interactions between individual dislocations and between dislocations and barriers in the material.

1.6.1 Stages of work hardening

The work hardening behaviour of a material is most often displayed through its stress-strain curve from which the various stages of work hardening can be identified. Let us first consider a single crystal that is strained in a direction that activates only one slip system, crystal D in Fig.4. In the beginning, the deformation occurs by so-called easy glide, represented by stage I in the stress-strain curve. Since the dislocations slip on only one slip system, there are no barriers to dislocation motion other than the internal friction between the atomic planes and any possible pre-existing obstacles. After some deformation, slip will begin to occur on other slip systems as well (multislip), and as the dislocations on intersecting slip planes start to interact with each other, their mobility will be limited and the strength of the material will increase. This stage II of work hardening that we now enter is linear, and it is characterised by a steep rate of order $G/200$. The transition from stage I to II, and the slope of stage II, are strongly dependent on the crystal orientation. If the crystal is oriented so that several slip systems are active from the start, stage I may not even appear, as in crystals A, B and C in Fig.4. During stage II of deformation the dislocation density will increase rapidly. But as the distance between the dislocations becomes sufficiently small, they will start to annihilate each other, or recover. The dynamic recovery phenomenon will reduce the storage rate of dislocations, and the hardening rate decreases.

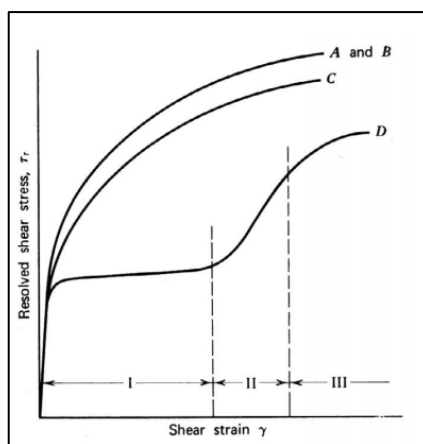


Figure 1.7 Stress-strain curves for single crystals of various orientations. Crystal D, having one active slip system, shows work hardening stages I, II and III. In the multi slip orientations A-C, the material goes directly into stage II. [9]

This is pictured by the non-linear region of the stress-strain curve, stage III, in Fig. 4. Beyond stage III follows a linear stage IV of low hardening rate, and in some cases, e.g. in super purity aluminium at room temperature and commercial purity aluminium above around 100°C, a stress saturation (hardening rate=0) is reached. The work hardening behaviour is sometimes presented by the work hardening rate (θ) as a function of stress. Figure 1.7 shows such a diagram for polycrystals of copper tested in torsion at various temperatures. It is well established that the hardening rate of FCC-metals and alloys increases with decreasing temperature [10] scales with the transition stress between stage III and IV, i.e. where the scaling parameter a is typically of size 0.1 for fcc-metals.

1.6.2 Precipitation strengthening

Precipitation hardening is the most important mechanism in strengthening of the AlMgSi alloys. The small particles are distributed in the relatively ductile matrix which increases the overall mechanical properties. Precipitation hardening or age hardening is formed by solution treating and quenching where second phases is in solid solution at elevated temperature. The second phase particles precipitate upon quenching and aging at a lower temperature. This phase must be soluble at an elevated temperature and it must exhibit decreasing solubility with decreasing temperature for the precipitation hardening to occur. In the case of AlMgSi-alloys, the second phases consist of the main alloying elements Mg and Si. A phase diagram showing the solubility of Mg and Si as a function of temperature represented by the Mg_2Si phase are presented in Figure 5.

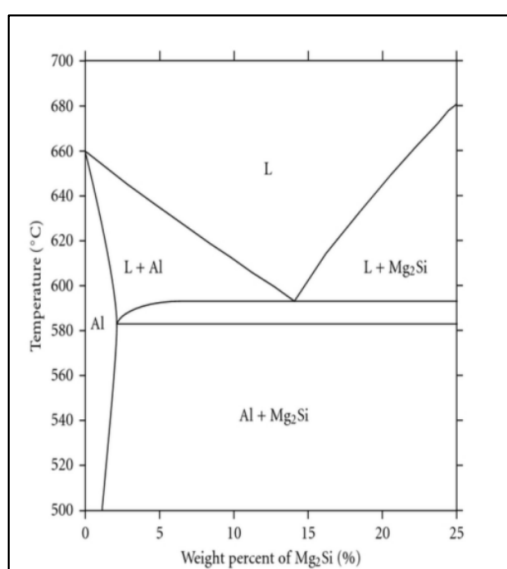


Figure 1.7 Phase diagram showing the solubility of Mg and Si as a function of temperature represented by the phase Mg_2Si . [11]

The precipitation hardening process is carried out in several steps. First the alloy is heated to temperature above the solvus temperature. This is to produce a homogenous solid solution α . The dissolving of the alloying elements enables dissolution of the second phase and eliminates segregations such as dislocations and grains in the alloy. After the alloy is set in the solubilization temperature, quenching of the alloy by air or water limits diffusion of atoms toward potential nucleation sites, and an unstable supersaturated solid solution α_{SS} is formed due to decreased solubility with decreasing temperature. The supersaturated alloy can then be subjected to artificial ageing. In this stage, the alloy is heated below the solvus line usually in the temperature range from 160-200 °C.

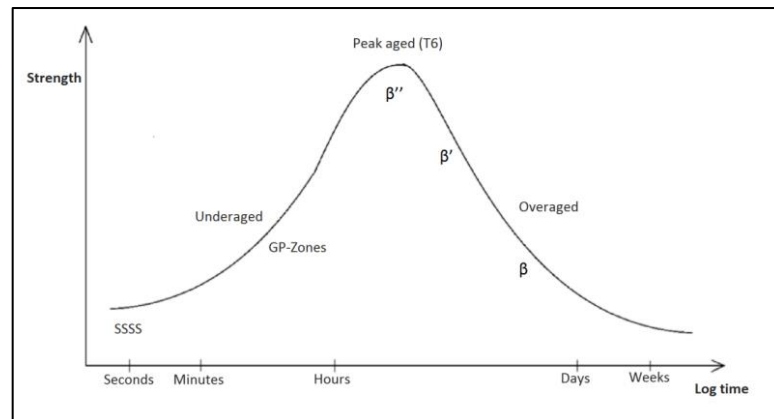


Figure 1.8 Modified sketch of strength evolution during artificial ageing of an AlMgSi-alloy

This allows atoms to diffuse at short distances. Due to the unstable α_{SS} phase, the second phase atoms diffuse at several nucleation sites that lead to controlled dispersion of particles. Typical precipitation sequence for AlMgSi-alloys is given in Equation 4 while the composition and the shape of the precipitates. The strengthening effect of the precipitates depends on the particles resistant to dislocation movement. The hardest phase for the aluminium 6xxx series is the β'' and Figure 6 shows the strength evolution with ageing time of 6xxx-alloys. [12]

1.6.3 Annealing

When any metal is being cold worked, grains are stretched, deformed, rises dislocation and imperfections which makes the material stronger but less ductile. Reduction of ductility is undesirable in metal forming operations. To achieve a softer material cold-worked metal is heated inside a furnace. If the material is heated for a long time, the cold worked metal goes through several changes such as (1) recovery (2) recrystallization, and (3) grain growth

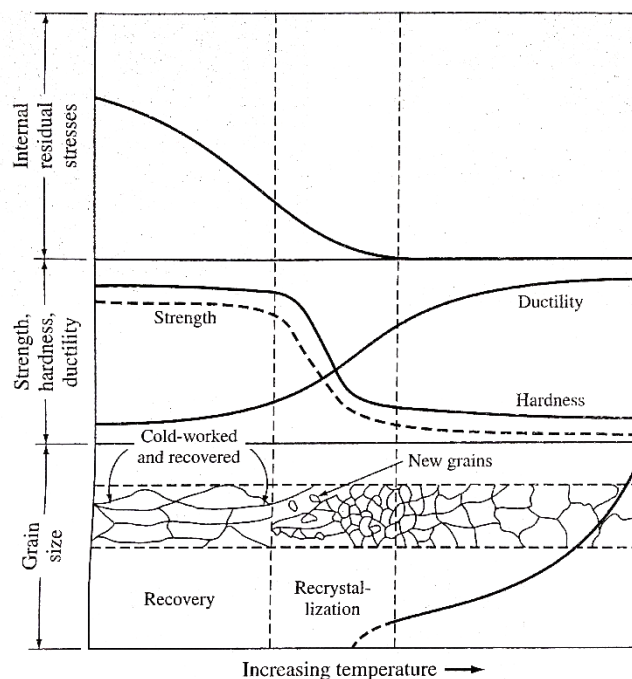


Figure 1.9 Effect of annealing on the structure and mechanical property changes of a cold-worked metal

Fig. shows the effect of temperature on mechanical properties of the materials. This reheating treatment which softens the material called annealing. When a material is being cold-worked strain-energy is absorbed in the material due to plastic deformation which leads to increase in internal energy of the material. Due to this reason internal energy of a strain-hardened material is always higher than an un-strained one.

When a cold-worked material is reheated below recrystallization temperature i.e. in recovery temperature range, internal stresses/ residual stresses get relieved. During recovery dislocations rearrange themselves into a lower energy configuration level with the help of supplied thermal energy. Due to recovery of materials sub-grain boundaries are produced having a low-angle grain boundary called as polygonization which precedes recrystallization. Internal energy becomes lower due to recovery as dislocations are annihilated and arrange themselves into lower energy state results in slightly reduction in strength but significant increase in ductility.

In recrystallization cold-worked structure is completely replaced by the new recrystallized grains. Primary recrystallization occurs by two principal mechanisms (1) an isolated nucleus can expand with a deformed grain (2) an original high angle grain boundary can migrate into more highly deformed region of the metal.

Annealing process consists of three stages (1) heating to predetermined temperatures (2) soaking temperature (3) cooling to the room temperature. Time is an important parameter in this process.

During heating and cooling temperature gradient exists between inside and outside of the furnace which depends on the size and the geometry of the work piece.

1.7 FUNDAMENTAL PRINCIPLES OF FRICTION STIR WELDING

The two phenomena involved in FSW process are the heating by the tool friction on the material and the material flow due to the tool stirring. Experiments and numerical models are intensely used to improve the understanding of these phenomena. However, numerical approach gives access to phenomena difficult to estimate by experiment. Predictive simulations should take into account the following topics: coupled friction/heat generation, plastic flow and slip surface development and finally heat and material flow [13]

1.7.1 Heat generation

Although FSW energy input is about the same or smaller than arc welding [14], the heat is distributed over a wider zone by the shoulder contrary to a focused arc. Moreover, the intimate contact between the sample and the backing plate acts as a heat sink and dissipates efficiently the heat. Consequently, FSW is considered as a cold-welding process leading to low residual stress level and distortion. Heat is mostly generated by the friction between the tool shoulder and the surface of the piece, followed by the high plastic work and the pin friction. Throughout literature, various percentage of the pin contribution to the heating process are available: 2% and 51% [15]. However, a general trend adopts a contribution lower than 5%. The contribution of each component of the process (shoulder friction, pin friction and plastic work) on the heating is clearly underlined by Dong et al. for AA6061 T6 welding [16]. Fig. 1 shows the heat production due to friction alone plastic work alone and combined friction/plastic work. In the case of friction alone, the temperature under the shoulder (about 350°C) is close to the one under the pin (300°C). However, this temperature is distributed on a larger surface, which causes a higher energy input. Moreover, the heating generated by the pin is close to the surface backing where the heat extraction is maximum. These two phenomena confirm the primary contribution of shoulder friction on the heat generation in the FSW process. In the case of plastic work alone, the global temperature is relatively low (about 100°C under the tool) compared to friction heating (250°C), except under the pin where the strain is higher. This simulation confirms the main role of friction on the heating. Finally, when the two phenomena are combined the global temperature under the tool is around 250°C with local hotter zones under the shoulder and the pin (>350°C).

The heat input by the shoulder friction may be calculated [17]. As shown in this equation, the power input increases with the increase of friction coefficient, the forging force (i.e. the normal load acting by the tool), the rotational speed and the shoulder diameter.

$$q_0 = \frac{4}{3} \pi^2 \mu P N R^3$$

q_0 : net power (W), μ : friction coefficient between the piece and the tool, P : pressure distribution (MPa), N : rotational speed (rpm), R : surface radius (mm).

The friction in front of the tool generates a plastic-like zone, which is then moved around the tool and deposited on the retreating side. This process is considered continuous along the workpiece. However, if melting occurs in front of the tool due to an excessive heating, less friction is generated due to the slip between the tool and the molten metal. As the temperature decreases, the material returns to a solid state and vice versa. This phenomenon may limit the use of high tool rotations and therefore the use of high welding speeds.

1.6.1 Material flow

The complex flow around the FSW tool can be decomposed into three simpler flow components (i) The first one may be considered as a cylinder of the welded material in rigid body rotation separated from the rest of the weld by a cylindrical shearing surface, i.e. a surface of velocity discontinuity (see Fig.7.a). This rotating cylinder is conceived as attached to the FSW tool and its rotational speed is equal to that of the tool spindle. Its boundaries expand toward the tool shoulder to take into account the shoulder shape. Moreover, its thickness slightly increases on the retreating side to accommodate the metal transfer to the rear of the pin as the pin moves. In the case of thinner materials, this cylinder may be defined as a conical region to take into account the shorter pin length. The shearing surface is therefore located between the shoulder corner and the pin bottom. (ii) The second flow component is a homogeneous and isotropic flow field equal and opposite to the welding speed (see Fig. 7.b). This uniform translation is usually called “extrusion movement” by analogy to the same manufacturing process. (iii) The third component is a ring vortex flow encircling the tool and bringing metal up on the outside, in at the shoulder, down on the inside and out again on the lower regions of the pin (see Fig. 7.c). This flow is driven by the threads and/or flutes on the pin and can be reversed if the direction of the threads or the tool rotation is reversed. This vertical motion is clearly underlined by tracer experiments [18], with 4 threads along the pin length, a marker is exposed to about 18 cycles around the pin. This generally leads to the disruptions and dispersion of the marker. As shown in Fig. 7.d, the combination of these three flows results in the formation of straight-through and vortex currents depending on the location. The material close to the advancing side travels in the rotating cylinder for a longer arc and is exposed to the axial flow of the ring vortex for a longer time. Consequently, the vortex current brings the metal to the bottom of the weld. Hence, vortex current residues are released to the advancing side in order to conserve the material. On the other hand, the straight through current occupies the retreating side as the metal in this region is exposed to the ring vortex for a

short time. The relative amount of straight-through and vortex currents apparently fluctuates, perhaps due to an alteration in shear vs. friction slip on the shoulder surface [19],[20].

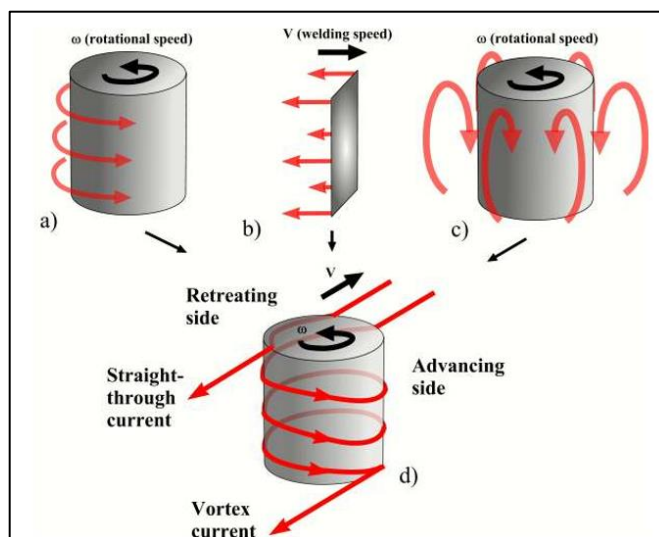


Figure 1.10 Three incompressible flow fields: a) rigid body rotation, b) uniform translation, c) ring vortex, d) combination of the three flow fields.

Tool parameters

As seen in the previous chapter, the quality of FSW joints are significantly affected by the welding parameters. The rotational speed of the shoulder-pin assembly, the welding speed, the downward forging force and finally the tool design must be optimized to obtain a sound and homogeneous weld [21]. This chapter attempts to summarize the different designs and tool parameters that can alter the characteristics of a FSW joint: shoulder diameter, pin size and shape (see Fig. 6).

Shoulder diameter and shape

Shoulder size is the primary source of energy input. Since the heat input is a function of the shoulder radius to the third power and only linearly depends on the applied forge force and the rotational speed, the achievement of a sound weld is strongly dependent on the tool size [22], [23]. Moreover, Z-axis forge force is also a function of the shoulder radius [24].

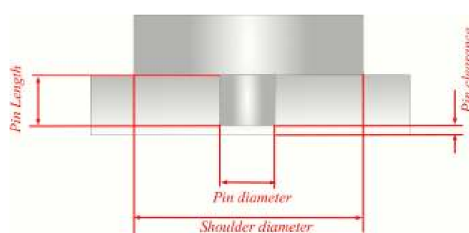


Figure 1.11 Scheme of tool parameters

Fig.8 shows various shoulder diameters as a function of sheet thickness for 30 different set-ups reported in the literature (aluminium samples in butt configuration from 1 to 8.3-mm thick). A clear trend is observed: the shoulder diameter is about 2.3 times the sample thickness plus a constant of 7 mm. When the thickness increases, more energy input is necessary, this is obtained by the design of a bigger shoulder. However, Reynolds and Tang observed that essentially equivalent welds may be made using a range of tool geometry, proving that the FSW process is relatively robust. Fig. 8 may also confirm that: for a given sample thickness, the range of shoulder diameters may be high. In the case of a smaller shoulder, the reduction in heat generation is balanced by a higher rotational speed.

Pin size and shape

The pin diameter is approximatively equal to the sheet thickness for thickness from 1 to 8.3 mm. Moreover, the minimum pin diameter is about 3 mm. Again, the range of the pin diameters may be high. For example, for 8-mm thick plate welding, pin diameters from 8 to 13 mm leads to defect-free welds. Reynolds et al. examined the influence of pin diameters from 8 to 12 mm on the X-axis force (i.e. along the welding direction) and the specific weld energy. For this range of tool geometries, pin diameter did not appear to influence the required x-axis force and the specific weld energy.

The difference between the pin length and the sheet thickness (defined in Fig. x). This value does not take into account the tool plunge during the process. This clearance is important to secure sufficient plastic deformation in the root of the weld. A pin clearance of 0 to 0.5 mm for thickness range of 1 to 8.3 mm has been reported in the literature, all these values leading to full penetrated welds. If the clearance is too small, this generates an unbonded area in the root and an early fracture during tensile or bend deformation will appear [25]. It should be noticed that a null value of pin clearance is generally avoided as it may cause pin damage due to the tool plunge during the welding. An important parameter in FSW tool design is the ratio of dynamic volume (volume swept by the pin during rotation) to static volume (volume of the pin itself). Increasing this ratio results in a reduction in the formation of voids in the welds and allows the

surface oxide to be more effectively disrupted and dispersed within the microstructure [26]. In conventional FSW, the dynamic/static ratio can be increased via the use of re-entrant features, flutes, threads and/or flats machined into the pin [27]. The presence of flats on the pin acts as the cutting edge of a cutter. Thereafter, the material is trapped in the flats and released behind the tool promoting thorough mixing. The extreme extension of this principle is the friction skew stir technique Exploitation of the dynamic/static ratio may be highlighted by the footprint technique.

The polar plot of the force footprint shows the force vector experienced by the tool during each revolution.

Optimum tool rotational speed

results in optimum heat input, formation of finer grains with increased plastic flow adequate bonding. Higher the value of tool rotational speed, higher will be the heat input and slow cooling rate. It causes metallurgical transformation such as solubilisation, reprecipitation and coarsening of the precipitates. Lower tool rotational speed causes less frictional heat generation, higher cooling rate, less plastic flow and inadequate bonding, results in coarser grain formation.

Low welding speed

results in high power density responsible for developing coarse grain in stirring zone. Increased welding speed ensures perfect tool work interaction, sufficient plastic flow and formation of fine grains. Lack of bonding takes place if welding speed exceeds the optimum value. Optimum axial load results in confinement of material within the cavity offers least heat dissipation rate.

Optimum direct axial load

plasticised material from leading edge to trailing edge and remains confined in weld cavity. Loss of heat takes place within the cavity. An increase in axial load results in more frictional heat generation, material is lost due to excessive rubbing of tool shoulder and base plate resulting decreased cross-sectional area. More heat loss takes place due to removal of material of base plate with decreased availability for heat for weld formation.

1.8 FORMING LIMIT DIAGRAM

A forming limit diagram often called Forming Limit Curve (FLC) used to predict the forming behaviour of the sheet metal. This graph predicts the failure region of the material. In order to perform Forming Limit Diagram experiment, circular marks are placed on the sheets. Then the sheet is deformed in a press. prior to forming Blank holder keeps the sheet in place and provides material locking to ensure proper deep draw. When the blank gets locked at a predetermined pressure, punch moves towards the sheet and deforms the sheet. When the sheet gets stretched, circles get deformed and results into an ellipse.

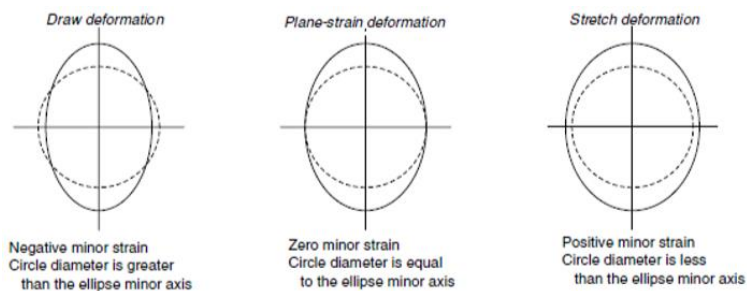


Figure 1.12 Circles deformed into ellipses in different modes of deformation

Let the initial diameter of the circle is d_1 and the final diameter of the deformed circle i.e. ellipse becomes d_{2minor} (minor diameter of the ellipse) and d_{2major} (major diameter of the ellipse). Principle strains can be found out in the form of major strain in the direction of the major axis of the ellipse is $\ln(d_{2major}/d_1)$ and the minor strain is $\ln(d_{2minor}/d_1)$. These values at failure and necking gives the failure and necking condition, strain values away from the necking gives the safe condition. A plot of the combination of major and minor strain of failure, necking and safe zone gives forming limit diagram, also known as Keeler-Goodwin diagram.

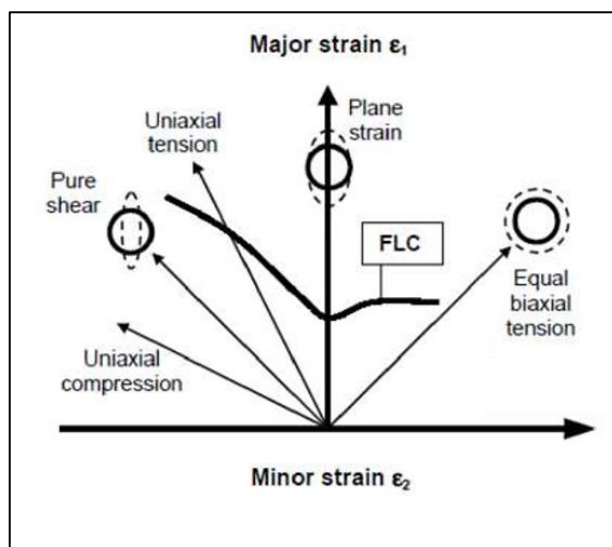


Figure 1.13 A typical forming limit diagram

The above shown curve shows the limit up to which the forming operation can be done without necking or fracture. The strain data above the curve represents the failure regions. The curve on the left-hand side indicates limit strains measured from the samples which have been deformed under combined tension and compression. The curve on the right-hand side indicates the limiting strains measured from the samples which have been deformed under biaxial tension. The major strain value when the minor strain is zero indicates plain strain condition.

1.8.1 Important material parameters which affect formability

The mechanical properties which affects the formability of sheet metals are strain hardening exponent, anisotropy and thickness of the material.

Strain Hardening exponent

Strain hardening exponent indicates the ability of a material to distribute strain uniformly when stretched in tension. So, it has large influence on the right-hand side of the FLD. The forming limit in plain strain increases with increase in strain hardening exponent. If n is reduced by cold working then the biaxial tension region becomes very small. Thus, cold working reduces the n value and hence reduces the formability.

Anisotropy

The normal anisotropy (\bar{R}) and planar anisotropy (ΔR) influences drawability and earing of the sheets during deep drawing [28]. R value represents the ratio of true strain in width to true strain in thickness.

Thickness

Higher thickness of the sheet offers higher formability. Higher limiting strains occur at the necking zone due to higher thickness of the sheet metal[29]. The neck shape depends upon the strain rate sensitivity index (m) of the material. Necks are more gradual in materials having a higher m . Aluminium alloy with smaller m , have much sharper necks. With sharper neck, the thickness effect is likely to be less significant[30].

CHAPTER 2

REVIEW OF LITERATURE AND OBJECTIVES OF THE PRESENT WORK

2.1 LITERATURE REVIEW

A Steuwer et al (2006) [31] studied the residual stress distribution in dissimilar friction stir welds using neutron and synchrotron X-ray diffraction as a function of tool rotation and traverse speed. In all of the welds measured the region around the weld line was characterised by significant tensile residual stress fields which were balanced by compressive stresses in the parent material. The largest stresses occurred in the longitudinal direction being typically two to three times the stresses in the transverse direction. In most cases, the peak tensile residual stresses were found at the edge of the tool shoulder approaching the local room temperature yield stress. The exception is at low rotation speed (280 rpm) on the AA5083 side of the weld where the stress peaks at the weld line. For the age-hardening alloy AA6082, a direct correlation of the position and magnitude of the peak tensile stress and the welding parameters was found. It should be noted that the relatively small size of the welded plates permitted an analysis of the residual stress state without dissecting the welds. As a result, stress relief will not have occurred. This may partially explain why the stresses measured in the current case are relatively high compared to studies on sectioned samples [8] and more in agreement with data from larger weld sections [32].

Z. Feng et al (2000) [33] studied residual stresses in aluminium friction stir welds. The specimens were 6 mm thick plates friction stir welded in the butt joint configuration at two welding speeds, 279 and 787 mm/min, respectively. The experimentally determined residual stresses show a symmetric double-peak profile across the weld centre line, with the peaks located in the middle of the heat-affected zone. The maximum tensile stress, which is in the longitudinal direction, is 130 and 200 MPa, respectively. It is shown that the difference in the residual stress is due to a change in the microstructure and stress relaxation that occurred as a result of the longer heating time associated with the low welding speed.

Hashimoto et al. [34] demonstrated that for a given aluminium alloy, high strength friction stir welds are obtained when the welding speed falls within a processing window. When the welding speed is too high, surface and sub-surface defects form, lowering the notch tensile strength in the weld zone. At low welding speed, the notch tensile strength is negatively affected by the formation of a softened zone.

L.-E. Svensson et al (1999) [35] studied that for Al-6082 friction stir welds, whose hardness profile resembles that of the Al-6061-T6, fracture occurs in the softest region outside the weld zone. On the other hand, for 5083 aluminium alloys, whose hardness exhibits hardly any variation across the weld, fracture was found mostly in the weld zone.

Detailed studies by North et al. (1999) [3] found that the notch tensile strength, in fact, scales with the width of the softened zone and when a small softened zone is produced, the notch tensile strength of the joint approaches that of the base metal.

Fatigue tests by Bussu and Irving [36] showed that the region of minimum hardness is also where most of the fatigue cracks were initiated. Thus, from microstructure point of view, higher welding speed produces friction stir welds with improved mechanical properties, so long as defects are not formed.

Paik et al (2008) [37] studied the use of high strength aluminium alloys in the ship building industry. They found that the benefit of using aluminium rather than steel include its lighter in weight, which helps increase cargo capacity and reduce power requirements, excellent corrosion resistance and low maintenance.

Mahoney et al (1998) [38] studied the mechanical properties of FSW aluminium alloys and compared with the mechanical properties of the parent material, which helps in finding the way of changing the behaviour of the parent material after friction stir welding.

Thomas et al. (2002) [39] studied the application of FSW technologies for ship building, design and construction and indicated that it is capable of reducing construction costs and welding distortion and improving durability in comparison with fusion welding.

Peel et al. (2003) [40] investigated the mechanical properties and residual stresses of a FSW aluminium 5083 test specimen, and concluded that these properties are governed by the thermal input rather than by the mechanical deformation caused by the FSW tool.

Kramer et al. (2007) [41] studied fusion welding process and friction stir welding process and concluded that FSW seems to be more attractive because of its solid-state low temperature working environment.

L. Dubourg et al. [15] studied FSW tool design, properties and application and concluded that the design of the tool shoulder-pin system influences significantly joint quality and reduces the loads during the process.

P.J. Withers et al. (2006) [40] studied the effect of tool traverse and rotation speeds on the residual stresses are quantified for welds between non-age-hardening AA5083 and age-hardening AA6082 and compared to single alloy joints made from each of the two constituents. The residual stresses have been characterised non-destructively by neutron diffraction and synchrotron X-ray diffraction. The region around the weld line was characterised by significant tensile residual stress fields which are balanced by compressive stresses in the parent material. The rotation speed of the tool has been found to have a substantially greater influence than the transverse speed on the properties and residual stresses in the welds, particularly on the AA5083 side where the location of the peak stress moves from the stir zone to beyond the edge of the tool shoulder.

)

L Fratini et al. (2006) [42] presented the results of a wide range of experiments on T parts. First, friction stir welding process engineering has been developed with the aim of determining the specific process parameters that make up the soundness of the obtained T parts. Then the performance of the obtained T-joints has been compared with T-joints obtained by metal inert gas welding and extruded T-parts. The parts have been tested utilizing a customized bending test with the aim of highlighting their behaviour both in elastic and plastic fields.

The effect of processing parameters on mechanical and microstructural properties of AA6082 joints produced by friction stir welding was analysed in the present study by P. Cavaliere et al. (2007). [43] Different welded specimens were produced by employing a fixed rotating speeds of 1600rpm and by varying welding speeds from 40 to 460mm/min. The joints mechanical properties were evaluated by means of tensile tests at room temperature. In addition, fatigue tests were performed by using a resonant electro-mechanical testing machine under constant amplitude control up to 250Hz sinusoidal loading. The fatigue tests were conducted in axial control mode for all the welding and rotating speeds used in the present study. The microstructural evolution of

the material was analysed according to the welding parameters by optical observations of the jointed cross-sections and SEM observations of the fractured surfaces were done to characterize the weld performances.

M.P. Miles et al. (2005) [44] investigated Friction stir welding (FSW) as a method for joining dissimilar-aluminium alloys 5182-O, 5754-O, and 6022-T4. These alloys are used in automotive applications in which parts consisting of dissimilar welded combinations of these alloys may be of interest. This study focuses on the formability of friction-stir-welded, dissimilar-alloy pairs of essentially the same gage, in order to investigate the mechanical properties that can be obtained using this approach. Testing showed that the properties of welded 5182/5754 alloy pairs retained reasonably good formability compared to base material performance. However, the 5182/6022 and 5754/6022 alloy pairs had significantly reduced formability compared to the base material properties, with failures occurring in the heat-affected zone (HAZ) of the 6022 or in the weld nugget itself. However, this level of formability was not much worse than that of monolithic, friction-stir-welded 6022.

In the present study, L. Reg investigated mechanical properties of friction stir welded aluminium alloys are examined experimentally. Tensile testing is undertaken on dog-bone type test specimen for aluminium alloys 5083 and 5383. The test specimen includes friction stir welded material between identical alloys and also dissimilar alloys, as well as unwelded (base) alloys. Mechanical properties of fusion welded aluminium alloys are also tested and compared with those of friction stir welded alloys.[41]

X.L. Wang et al. (2000) [45] studied neutron diffraction study of residual stresses in 6061-T6 aluminium friction stir welds. The specimens were 6 mm thick plates friction stir welded in the butt joint configuration at two welding speeds, 279 and 787 mm/min, respectively. The experimentally determined residual stresses show a symmetric double-peak profile across the weld center line, with the peaks located in the middle of the heat-affected zone. The maximum tensile stress, which is in the longitudinal direction, is 130 and 200 MPa, respectively. It is shown that the difference in the residual stress is due to a change in the microstructure and stress relaxation that occurred as a result of the longer heating time associated with the low welding speed.

Min-Su Han et al. (2009) [46] studied the mechanical characteristics for friction stir welding (FSW) of 5083-O Al alloy were evaluated. The results show that in FSW at 800 r/min and 124 mm/min, a weld defect is observed at the start point. However, the button shape at the end point is good and the stir zone has a soft appearance. At 267 mm/min, a void occurs at the button. A slight weld defect and rough stir zone are seen both at the start and end points at 342 mm/min. Moreover, at the bottom, a tunnel-type void is observed from an early stage to the end point, and at 1 800 r/min, a weld defect can be found from an early stage to the end point. These defects are rough with imperfect joining due to excessive rotation speed and high physical force. Weld fractures relative to rotational and travel speeds are observed at the stir zone. The optimum FSW conditions are a welding speed of 124 mm/min and a rotational speed of 800 r/min.

H. Hayashi et al. (1994) [7] introduce the present status of the application of these materials to autobody parts and discuss the problems on forming these materials from the point of material characteristics and forming techniques. In order to solve social demands to automobile such as weight reduction for energy saving and environmental preservation, newly-developed sheet materials have been applied to autobody parts. The characteristics of high strength steels, coated steels, steel-plastic laminates and aluminium alloys were reviewed and problems in forming processes were discussed. New types of sheet materials with good formability have been developed for automotive panels, but there still many problems remain to be solved in order to promote the extended practical application of these materials.

Jun Liu et al. (2009) [47] investigated and compared during high temperature tensile tests to study their formability. The results of tensile tests and microstructures were shown, which indicated the deformation properties under different conditions. Both alloys exhibited relatively weak strain hardening effects especially at relatively lower strain rates. Furthermore, the highest strain rate sensitivity index (m value) was obtained, and the peak of percent elongation-to-failure also coincided with the ranges of highest m value. The flow stress coupled with the dynamic grain growth was related with the temperatures and strain rates. The grains appeared to be coarser in the deformed samples.

P.F. Bariani et al. (2013) [48] investigate the feasibility of producing sheet components by stamping AA5083 sheets at elevated temperature and strain rate. Laboratory tensile and Nakajima-type tests were carried out to evaluate the material flow stress, ductility and fracture limits sensitivity to temperature and strain rate, and therefore to determine the optimal combination of process parameters assuring both maximum formability and effective post-

deformation mechanical properties. Industrial trials were conducted on an automotive component to validate the laboratory results.

J. Liu et al. (2010) [49] studied the non- superplastic grade of 5083 aluminum alloy (AA5083) sheets with thickness of 3 mm was employed in a superplastic-like forming process, which is a combination of drawing (mechanical pre-forming) and superplastic forming (blow forming). Experimental trials were conducted to verify the possibility of improving the forming rate and lowering the process temperature. The blank was firstly pre-formed during the mechanical pre-forming phase. As a result, some part of material along the flange area was introduced inside the deformation cavity in advance of the blow forming phase. Secondly, argon gas was applied on the sheet, which would be deformed to come into contact with the inner die surface at the end of pressure cycle. It took only 8 min for the blow forming phase, and the process achieved an almost fully formed part at 400°C. The minimum thickness occurred at the inward corners, and the maximum thinning of the formed part was 54%. Grain growth and cavitation were found from the microstructure observations.

D.E. Cipoletti et al. (2008) [50] studied the influence of heterogeneity in grain boundary sliding resistance on the constitutive behaviour of AA5083 during high-temperature deformation with the help of simulations assumed a uniform resistance to sliding on all grain boundaries. Molecular dynamic simulations indicate that sliding resistance is strongly sensitive to the character of the boundary: high angle boundaries have resistance up to an order of magnitude lower than low angle boundaries. To investigate the effects of this heterogeneity, finite element simulations are used to compute the influence of the fraction of freely sliding boundaries f in a polycrystal on its creep response and operative deformation mechanisms. Our computations show that (i) The critical strain rate at which the deformation mechanism transitions from GBS to DC varies from $2 \times 10^{-5} \text{ s}^{-1}$ to 10^{-3} s^{-1} as f is increased from 20% to 100%. (ii) The stress exponent in the GBS regime decreases from approximately 3.25 to 1.5 as f increases from 0% to 100%. The stress exponent in the DC regime is less sensitive. (iii) The flow stress at a strain rate of 10^{-4} s^{-1} (GBS regime) increases from 6MPa to 14MPa as f varies from 100% to 0%; in contrast the flow stress at strain rate of 0.01 s^{-1} increases from 33MPa to 42MPa (DC regime). (iv) A sudden increase in GBS and a corresponding reduction in flow stress occur as f is increased from 67% to 77%, suggesting the presence of a percolation threshold. (v) A second (but smaller) increase in grain boundary sliding occurs when f is increased from 39% to 46%. Microstructures with $f=39\%$ appear to contain at least one grain which is completely surrounded by sliding resistant boundaries; microstructures with $f=46\%$ do not. We speculate that the blocked grains may act as

reinforcing particles. (vi) The flow stress and deformation mechanism are determined by the fraction of freely sliding grains, and are not sensitive to the detailed spatial distribution of sliding resistance in the polycrystal.

L. Leotoing et al. (2008) [51] studied the strain rate influence on AA5083 formability with the characterization of material behaviour of an aluminium alloy 5083 at high temperatures. To describe its visco-plastic behaviour, Swift's hardening law is used and the corresponding parameter values are identified. Then, two different approaches are introduced to construct FLDs (forming limit diagrams) of this alloy sheet and evaluate the effect of the rate sensitivity index on its formability. The first one is theoretical (the M-K model), and an algorithm is developed to calculate the limit strains by this model. In the second approach, the Marciniak test is simulated with the commercially available finite-element program ABAQUS. Based on FEM results, different failure criteria are discussed and an appropriate one is chosen to determine the onset of localized necking. With the material behaviour data corresponding to AA5083 at 150 °C, parametric studies are carried out to evaluate the effect of the strain rate sensitivity index. The comparison of results by these two approaches shows the same tendency that an improvement of the formability with increasing strain rate sensitivity is observed. Finally, by consideration of the compensating effects of the strain hardening and rate sensitivity indices, the FLDs of this sheet at 150, 240 and 300 °C are determined and compared. Results show that the formability of AA5083 seems not to be improved up to a certain temperature (between 240 and 300 °C), above this temperature, the formability is greatly enhanced.

M. Simoncini et al. (2014) [52] studied the effect of FSW parameters, tool configuration and sheet positioning on the mechanical properties, microstructure and post-welding formability to evaluate the advantages offered by the new welding methodology, the experimental results obtained using the double-side friction stir welding were compared with those given by the conventional process. The conventional FSW joints show ultimate tensile strength and elongation higher than those exhibited by the DS-FSW joints.

K. S. S. Kumar et al. (2016) [53] the formability of AA6082 alloy to manufacture parabola cups using single point incremental forming (SPIF) process. The finite element analysis has been carried out to model the single point incremental forming process using ABAQUS software code.

Formability of steel and aluminium alloys in hot stamping and cold die quenching processes is studied in this research. Viscoplastic-damage constitutive equations are developed and determined from experimental data for the prediction of viscoplastic flow and ductility of the materials. The determined unified constitutive equations are then implemented into the commercial Finite Element code Abaqus/Explicit via a user defined subroutine. [54]

Xi Luan et al. (2016) [55] Forming limit diagrams (FLDs) of AA6082 at warm/hot stamping conditions. The tests were carried out at various temperatures from 300°C to 450°C and forming speeds ranging from 75 mm/s to 400 mm/s. The strain was visualized and measured using ARGUS software provided by GOM. The results clearly show that the formability of AA6082-T6 sheet metal, in terms of the limit major strain, increased by 38.9% when the forming temperature was increased from 300°C to 450°C at a speed of 250 mm/s, and increased by 42.4% when the forming speed was decreased from 400 mm/s to 75 mm/s at a temperature of 400°C. It was verified that hot stamping is a promising technology for manufacturing complex-shaped components. In this work, a new test rig was designed and manufactured, and the FLDs of the high strength aluminium alloy AA6082 in the T6 condition were experimentally determined using formability tests. The effects of forming temperature and forming speed on the formability were thoroughly investigated representing warm/hot stamping processes. The FLDs under different conditions were obtained.

J. Liu et al. (2015) [56] studied an advanced forming technology, solution Heat treatment, Forming and in-die Quenching (HFQ®), has been employed to form AA6082 tailor welded blanks (TWBs). In comparison with conventional stamping of TWBs, the mechanical properties and formability of AA6082 laser TWBs could be improved under the HFQ forming condition. The TWB was divided into three physical zones, i.e. base metal, heat affected zone (HAZ) and weld zone, based on the hardness distribution. It was found that the degraded hardness of the weldment can be restored after HFQ forming. TWBs of AA6082 with different thickness ratios of 2 (2–1 mm), 1.3 (2–1.5 mm) and 1 (1.5–1.5 mm) were used to study the TWB thickness ratio effects on the forming behaviour. Hemispherical punch dome tests on the TWBs with varying thickness ratios demonstrated different formabilities, and indicated increased displacement of the weld line with increasing thickness ratio. Finite element (FE) modelling was adopted to analyse the weld line movement and strain distributions during HFQ.

S. Mohamed et al. (2012) [57] studied a set of coupled viscoplastic constitutive equations for deformation and damage in hot stamping and cold die quenching of AA6082 panel parts. The equation set can be used to predict viscoplastic flow and plasticity-induced damage of AA6082 under hot forming conditions. Deformation and damage depend upon a coupled set of evolving internal state variables, e.g. dislocation density, which in turn is affected by thermally activated and deformation-dependent recrystallisation and recovery. A phenomenological description of damage is derived based on the expected physical scaling with temperature, strain and strain rate. The resulting equations were implemented in the commercial software ABAQUS. A good agreement between the process simulation and the experimental results has been achieved. This confirms that the physical dependencies in the constitutive equations are correctly formed, and that the equations and FE model can be calibrated and used for hot stamping of AA6082 panel parts. Further, forming process optimisation was carried out using the model to identify the optimal forming parameters for a basic panel part with a circular hole in the middle. The study concludes with a discussion of the potential impact of the constitutive model, experimental characterisation and modelling results on AA6082 panel parts manufacture.

2.2 RESEARCH GAP & MOTIVATION

Automobile industries are ever improving on the verge of providing luxury coupled with safety and fuel economy to the demands of the mankind. The overall adopted changes in the materials used in automotive body panels due to the required formability and crashworthiness provide a challenge to the design engineers. Higher weight of a vehicle leads to its higher fuel consumption. It is necessary to select a material and design it in such a way that it exhibits better safety and fuel economy when employed in automotive components.

Now a days, steels and Aluminium alloys are top choices for automobile and aerospace components due to the design, manufacturing ease and favourable mechanical properties offered. Aluminium is one of the lightest engineering metals, having superior strength to weight ratio to that of steel. Aluminium alloys are being employed in an ever-increasing number of applications by utilizing various combinations of its advantageous properties such as strength, lightness, corrosion resistance, recyclability and formability.

Tailor Welded Sheets are fabricated by joining two sheets of same thickness or different properties. In Friction stir welding weld bead plays an important role in forming of the sheets. Due to the solid state joining by plastic deformation of the materials strain hardening takes place, hardness increases, ductility decreases. So, this study is based on the search for the solution to increase the formability of the Friction Stir Welded sheets. Increased formability enables the material to be formed up to a relatively higher limit. It means the material can sustain load with having a higher strain. This will enhance the formability of the material.

CHAPTER 3

METHODOLOGY

In the present study experimentation and numerical investigation has been carried out to validate the outcomes, which has been discussed in this chapter sequentially. Tensile testing followed by design of Experiments i.e. ANOVA analysis, Friction Stir Welding and its fixture, Annealing, Residual stress and Micro-Hardness measurements, Stretch Forming, Finite Element Analysis and Forming limit diagram has been described in this study.

3.1 MATERIAL SELECTION

Two aluminium alloys AA5083 and AA6082, each of 2 mm thickness have been selected for the study. AA5083-O and AA6082-T6 has been procured. Aluminium alloy 5083 has extensive application in sheet metal forming operations [47], Shipbuilding [58], Rail cars, Vehicle bodies, Tip truck bodies, Mine skips and cages, Pressure vessels. Aluminium alloy 6082 has its various application such as High stress applications, Trusses, Bridges, Cranes, Transport applications[59]. Chemical composition of both the materials have been shown in Table.3.1

Table 3.1 Chemical composition of AA5083 and AA6082

Alloy	Mg	Si	Mn	Cu	Cr	Zn	Ti	Fe	Al
AA5083	4.0-4.9	0.4	0.40-1.00	0.10	0.05-0.25	0.25	0.15	0.40	Remainder
AA6082	0.6-1.20	0.70-1.30	0.40-1.00	0.10	0.25	0.20	0.10	0.50	Remainder

3.2 TENSILE PROPERTIES

Uniaxial tensile testing was carried out as per ASTM-E8M standard. AA5083 and AA6082 specimens were prepared having a gauge length of 25 mm. H50KS Bench-top Uniaxial tensile testing machine having a maximum capacity of 50 KN was used to perform the tests with a crosshead speed of 2.5mm/min.

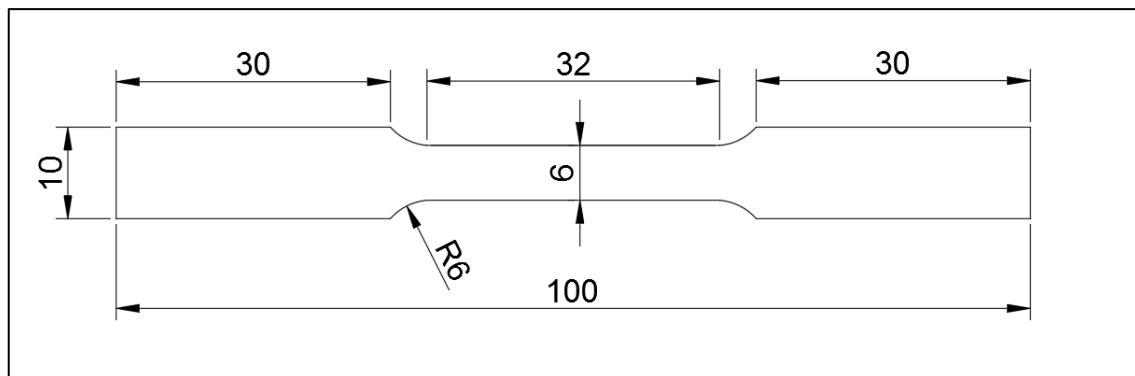


Figure 3.1 Tensile testing specimen as per ASTM-E8M standard

The force measuring system in this UTM is a full strain gauge load cell of Z-Beam construction for use in tension and compression. These interchangeable load cells are available from the maximum capacity of the load frame, down to 5N and include self-identifying connectors. The force measuring resolution is 1/320000 of load cell capacity over the full range (nominal) $\pm 0.5\%$ of the indicated load from 2 to 100% of load cell capacity and $\pm 1\%$ down to 1% of the load cell capacity and force sampling rate is 200 Hz (nominal).

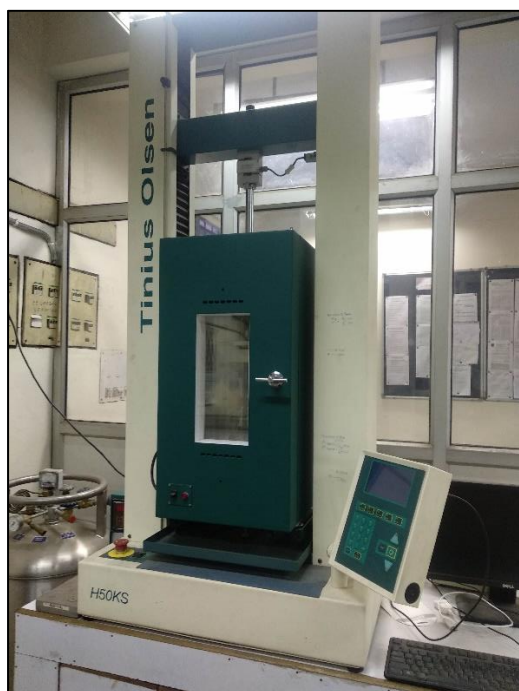


Figure 3.2 Universal Tensile testing machine and the crossheads

Extension measuring system of this machine consists of precision encoder operated directly from the crosshead driving ball screw for readout of extension (position) with an extension resolution of 0.001 mm of the full crosshead travel and extension accuracy of ± 0.01 mm or 0.05% without any load. Crosshead drive system is operated by precision ball screw drive operated by a DC servo motor and 32-bit motor controller. Speed accuracy of the machine is $\pm 0.05\%$ of the set

speed. This machine is rated at 500 Watt at 220/240 Volts, 50/60 Cycle, Single Phase and designed to be operated from 0 to 38°C with a non-condensing atmosphere of 10 to 90% Relative Humidity.

3.3 FINDING OF ANNEALING TEMPERATURE OF AA6082-T6

To find out the annealing temperature of AA6082-T6 pilot experiments were carried out at different temperatures. Tests were carried out at 250°C, 300°C, 350°C, 400°C. To carry out the experiments, muffle furnace was used. Dehydrated sand was used to prevent oxidation during annealing. Each AA6082-T6 sheets were put inside the sand chamber for continuous heating up to desired temperature inside the furnace followed by 2 hours of soaking time and chamber cooling had been provided to the materials. After annealing, sheets were gone through tensile testing for optimum strength and percentage elongation. Desired annealing temperature was found out through a thorough study of the mechanical properties of the annealed sheets.

3.4 ANNEALING OF AA6082-T6 SHEETS

Aluminium sheets were annealed prior to Friction Stir Welding. Each AA6082-T6 sheet was fully annealed at 300°C with 2 hrs of soaking time followed by chamber cooling. Exterior temperature was maintained at 25°C.

3.5 PILOT EXPERIMENT TO GET THE OPTIMUM SPEED, FEED FOR FSW

Friction Stir Welding was carried out to join AA6082-O and AA5083-O sheets. Pilot experiments were carried out to get the required input welding parameters for desired mechanical property of the welded joint. The input parameters for welding are tool travel speed, tool rotational speed, tool pin to shoulder diameter.

Input parameters are detailed below:

Tool travel speed = 20mm/min, 25mm/min, 30mm/min

Tool rotational speed = 700 rpm, 800 rpm, 900 rpm

Tool pin depth = 1.5 mm

Ratio of tool pin to shoulder diameter = 5

3.5.1 Analysis of the input data for FSW and Tensile properties of Weld beads

Input parameters play a key role in friction stir welding and weld quality. A sound weld is necessary to get desired formability of the welded sheets. Pilot experiment consists of 9 combinations of tool travel speed and tool rotational speed and 9 combinations have their own welded sheets. All the welded sheets are tested in universal tensile testing machine for the material property of the weld bead.

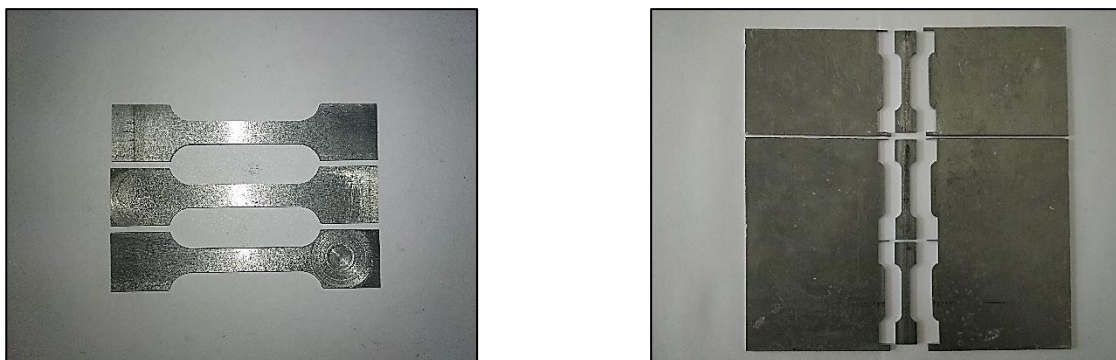


Figure 3.3 Tensile testing specimen cut from the annealed and non-annealed sheet

The best weld was chosen based on the desired strength and % elongation with the help of Taguchi and one-way ANOVA technique. An orthogonal array of L_9 was implemented to get the optimum process parameters for the desired response [60]

3.5.2 Taguchi Method

To carry out the FSW process well and in efficient manner pilot experiments were carried out having 2 sets of independent variables, each having three levels. The independent variables are Tool Travel Speed and Tool Rotational Speed. The outcomes or the dependent parameters are Ultimate tensile Strength, % Elongation (Longitudinal direction), and %Elongation (Transverse direction). To find the optimum input parameters an Orthogonal Array (L_9) was designed. Finally signal-to-noise ratio was measured on the basis of larger is better to get the optimum parameters.

Design of Experiments

In this study a series of experimentation has been carried out to predict the optimum result in the form of UTS and % Elongation, which has been discussed below.

Output Parameters: UTS, %Elongation (S), %Elongation (I)

Input Parameters: Tool Travel Speed, Tool Rotational Speed

Objective Function: Larger is Better

S/N Ratio for the function: $-10\text{Log}_{10}(\text{sum}(Y^2)/n)$

Where, “n” is the “Sample Size” and “Y” is the “output parameters in that run”

Table 3.2 Process parameters and their levels

	Notation	Levels of factors		
Tool Rotational Speed	TRS	700	800	900
Tool traverse speed	TTS	20	25	30

The appropriate Orthogonal array which has been used for this experimentation has been shown in Table 3.3.

Design Summary

Taguchi Array L₉(3²)

Factors: 2

Runs: 9

Columns of L₉(3⁴) array: 1 2

Table 3.3 Standard L₉ Orthogonal Array

Experimental run	Control Factors and Levels	
	1	2
1	1	1
2	1	2
3	1	3
4	2	1
5	2	2
6	2	3
7	3	1
8	3	2
9	3	3

Matrix experiment was carried out on the basis of probable combination of the input parameters. Total 9 experiments were carried out to get the signal-to-noise ratio.

Table 3.4 Experimentation control log using Orthogonal Array L₉

Experimental run	Tool Traverse Speed	Tool Rotational Speed
1	20	700
2	20	800
3	20	900
4	25	700
5	25	800
6	25	900
7	30	700
8	30	800
9	30	900

Experimentally measured values of UTS, %Elongation (S) and %Elongation (I) have been used as responses and as per objective function larger is Better control function was used to get the signal-to-noise ratio. The average of the signal to noise ratios for UTS, %Elongation (S) and %Elongation (I) are also calculated.

Analysis of Variance is used to calculate response data of each parameter in the Orthogonal Array experiment. Analysis of variance (**ANOVA**) is a collection of statistical models and their associated estimation procedures (such as the "variation" among and between groups) used to analyse the differences among group means in a sample.

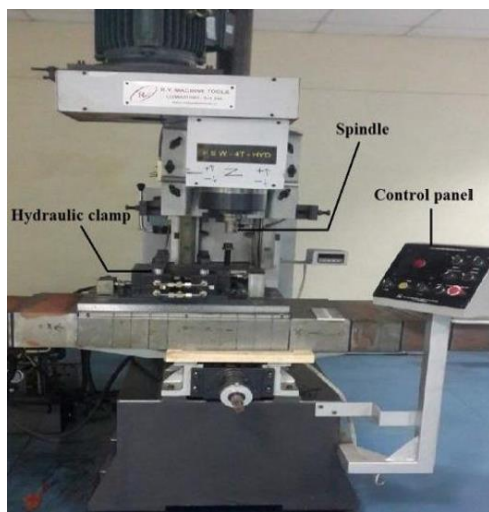
3.6 FRICTION STIR WELDING OF AA5083-O AND AA6082-O

3.6.1 Friction Stir Welding machine

Friction Stir Welding technique has been used to fabricate the Tailor Welded Blanks. “R V machine tools, FSW 4T-HYD”, as shown in Table-x was used to weld the sheet metals. This machine is having hydraulic actuated bed movement in “X” and “Z” directions and manual in “Y” direction. The movement of the machine bed and machine head is controlled by a control panel. It is also having an option to tilt its head up to 7 degree in both the sides only on “ZX” plane. The feed of the table and vertical movement of the spindle head can be changed by valve regulator.

Table 3.5 Specification of the Friction Stir Welding machine

Power	11 KW
Rotational Speed	3000 rpm
Clamp type	Hydraulic actuated
Load capacity	25 KN

**Figure 3.4** Friction Stir Welding Machine

Before welding both the sheets were in annealed fully annealed condition. AA5083-O was placed on the advancing side and AA6082-O on the retreating side as shown in figure 3.5.

**Figure 3.5** Friction Stir Welding of AA5083-O and AA6082-O

3.6.2 Friction Stir Welding Tool

Friction Stir welding tool plays the key role to join the sheets. While moving through the sheets it plastically deforms both the sheets and mixes-up the material from both the sheets. So, the technique of mixing is a major factor in this welding process. In this study single tool was used, details of which is given in Table-3.6.

Table 3.6 Specification of Friction Stir Welding Tool

Tool material	H13 Steel
Tool Hardness	59 HRC
Shoulder diameter	15 mm
Shoulder Profile	Cylindrical
Pin diameter	5 mm
Pin Profile	Cylindrical
Pin length	1.5 mm

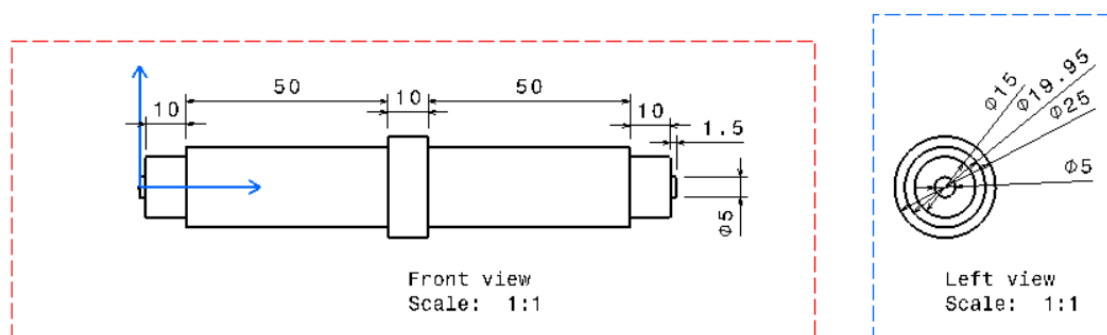


Figure 3.6 1st angle projection of the FSW tool

3.6.3 Process Parameters

Process parameters for the friction stir welding had been decided after a pilot experiment keeping the tool geometry and tool material constant. Process parameters are Tool rotational speed, Tool travel speed keeping the tool penetration to the material constant for each and every welding. Prior to set the process parameters for all the welding, a pilot experiment was carried out

3.7 ANNEALING OF WELDED SHEETS

This study incorporates comparison of formability of annealed and non-annealed Friction Stir Welded sheets. So, half of the total welded sheets were gone through annealing process. Welded sheets were annealed at 300°C inside the muffle furnace with a 2 hrs soaking temperature. Sheets were kept inside the de-hydrated sand bath while going through the annealing process. The annealed sheets were taken out from the chamber when chamber temperature becomes less than 60°C.

3.8 TENSILE PROPERTIES OF ANNEALED AND NON-ANNEALED WELDED SHEETS

Uniaxial Tensile properties of annealed and non-annealed sheets had been checked for the confirmation of the material properties of the sheets. Tensile specimen according to the ASTM-E8M standard had been prepared and tested on the previously detailed Universal Tensile Testing machine of 50KN capacity. yield strength, yield stress, percentage elongation, Ultimate Tensile strength and Ultimate Tensile testing Force was recorded from the machine output.

3.9 MICROSTRUCTURE PREPARATION OF THE SPECIMEN

Microstructure preparation of the specimen incorporates multiple steps such as mounting of the specimen, Dry polishing, Wet polishing and Etching. Different steps are discussed accordingly.

3.9.1 Mounting of the specimen

Mounting is necessary to make the specimen for proper gripping and positioning. Cold mounting or embedding is when a resin is mixed with a hardener (or accelerator) to provide the mounting compound, and then the polymerization process take place to form the block. In some cases, this process gives-off heat. However, this heat generation can be controlled by the use of ice or cool air blow setting.



Figure 3.7 Mounted Friction Stir Welded specimen

3.9.2 Polishing

Polishing is a finishing process for smoothening the surface of workpiece by using an abrasive and a work wheel or a leather strop. Polishing is used to enhance the appearance of a workpiece, prevent contamination of instruments, remove oxidation, create a reflective surface. In metallography polishing is used to create a flat, defect free surface for the examination of the microstructure under a microscope

Dry Polishing

Dry polishing was carried out on a polishing station. A series of different grade of emery paper (100,220,320,400,500,600,800,1000,1200,1500,2000,2200) were used for dry polishing.

Wet Polishing

Wet polishing was done on a velvet cloth using alumina powder. It makes the surface more clear for microstructure inspection.



Figure 3.8 polishing station and Microscope

Etching

Etching was done with the help of proper etchant solution for the aluminium. Then the microstructure was observed with the help of a microscope shown in figure 3.8.

3.10 MICRO-HARDNESS MEASUREMENT OF THE FSW SHEET PRIOR AND AFTER ANNEALING

Micro Hardness number was tested on the welded specimen through a line mapping across its cross section. Vickers method to check the hardness of the material was implemented with a hardness scale of HV0.05 with a dwell time of 10 seconds. 100 gm load was applied through a diamond pyramid indenter. The process of measuring micro-hardness incorporates loading, dwell period, unloading then measurement of both the diagonal of the indentation. In detail this micro-

hardness measuring machine composed of six turrets, two of which are indenters and rest of the four are objective lens having different magnification. Figure 3.9 shows the image taken from a camera attached with the head of the instrument.



Figure 3.9 Duramin 40 Micro-Hardness tester

The table or the bed of the instrument has computer-controlled screw operated three axes of motion in “X”, “Y” and “Z” direction. So, to map a line for a series of measurements the specimen has to be fixed on the table, then table finds its required position offset from the periphery of the specimen to locate the starting point for the measurement. Then required indenter comes on the specimen and starts the measurement process explained above.

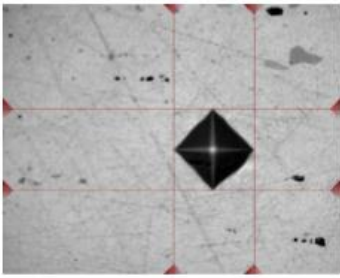
ID	1 (1/1)	
Hardness	90.87 HV0.05	
d1	0.0316 mm	
d2	0.0323 mm	
Position	x: 120.22 mm y: 38.53 mm	
Conversions		
Time	3:16:12 PM	

Figure 3.10 Output screen of the hardness measurement

3.11 PREPARATION OF SPECIMEN FOR STRETCH FORMING OPERATION

Welded sheets were LASER marked with the help of A LASER marking machine. To make the LASER mark samples were kept beneath the laser head and the beam was focused on to the sheets to get proper circles. Circle having a diameter of 5mm was marked on the back side of the sheets. Speed of the operation was set on 500 mm/s with a frequency of 20KHz. The laser marking pattern is shown in the figure 3.11.

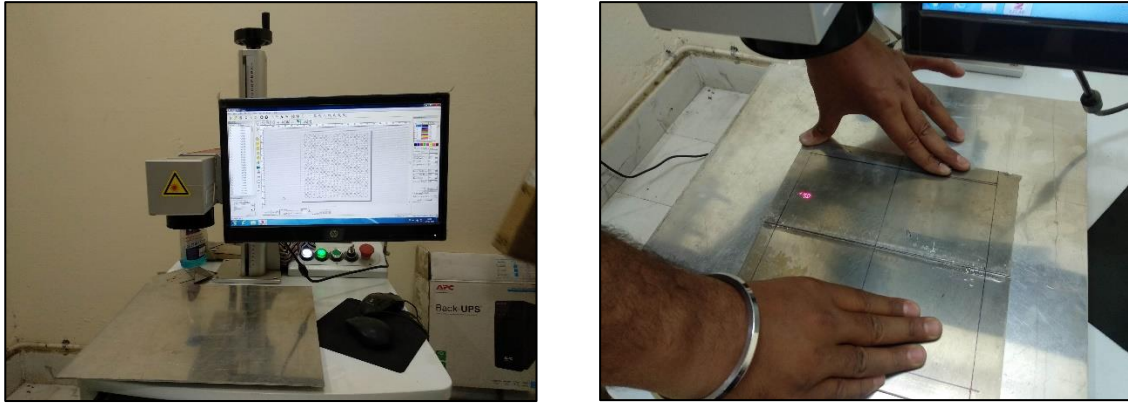


Figure 3.11 computerized Laser marking setup along with its operation

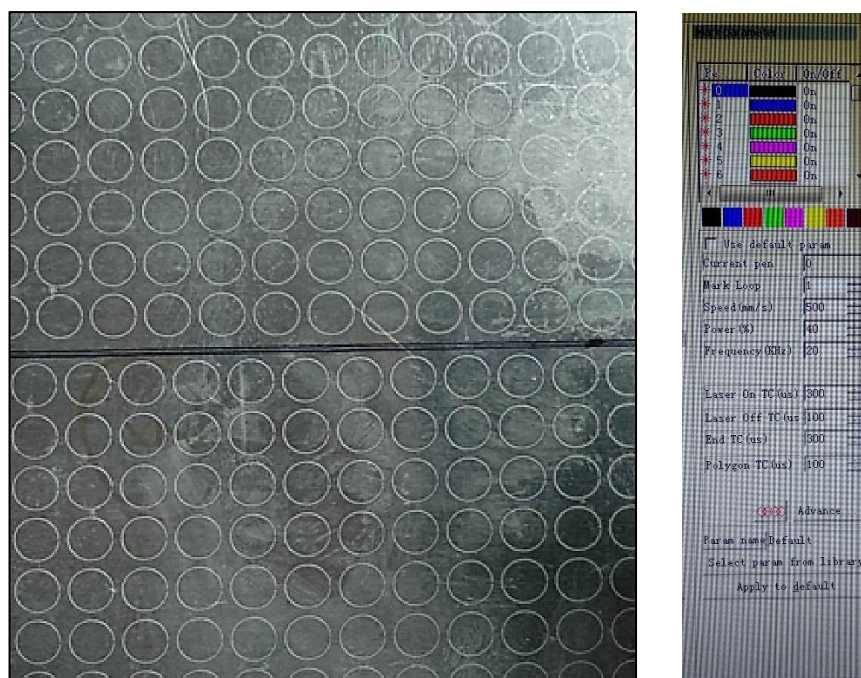


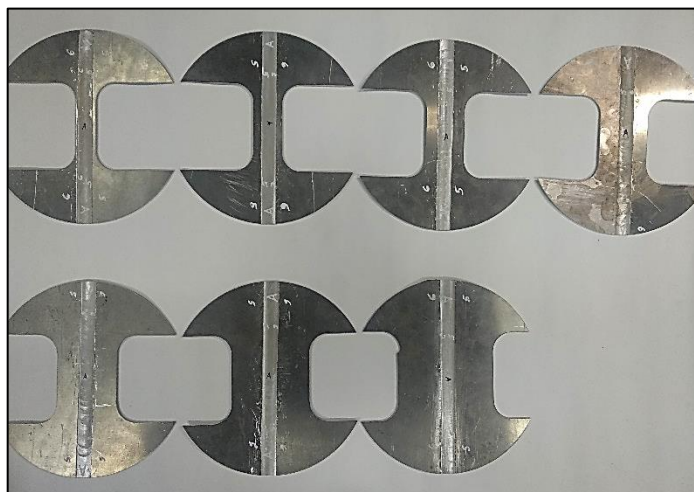
Figure 3.12 LASER marked specimen along with the parameter control screen

3.11.1 Laser cutting of the samples

Samples required to perform the formability test were prepared with the help of a 1 KW hydraulic operated optical fibre laser cutting machine (HSG LASER make). The specification of the machine has been given below:

Table 3.7 Specification of LASER cutting machine

power	1KW
Cutting speed	200mm/s
Nozzle diameter	1.5mm
Laser beam diameter	0.3mm
Bed size	5'x10'
Actuators	Hydraulic operated

**Figure 3.13** Laser cutting machine**Figure 3.14** Laser cut samples for formability test

3.12 DESIGN AND FABRICATION OF DIE-PUNCH-HOLDER SETUP FOR FORMABILITY TEST

The study consists of various experimentation among which stretch forming operation plays a major role to determine the output. Specific punch, Die, Blank Holder was manufactured for the stretch forming operation. 100 mm diameter hemispherical punch was used to perform the tests. The hemispherical punch is made of HCHCR D2 steel having external thread of 35 mm nominal diameter and 3mm of pitch which makes a threaded joint with the master cylinder for the punch movement. HCHCR-D2 steel is Cold Work Steel with High Carbon High Chromium contents. The Quality with high wear resistant and toughness properties due to Vanadium addition of 0.90%. Normally its supply condition is an Annealed and will offer hardness to reach 57-59 HRC. It can be machinable in the annealed condition.

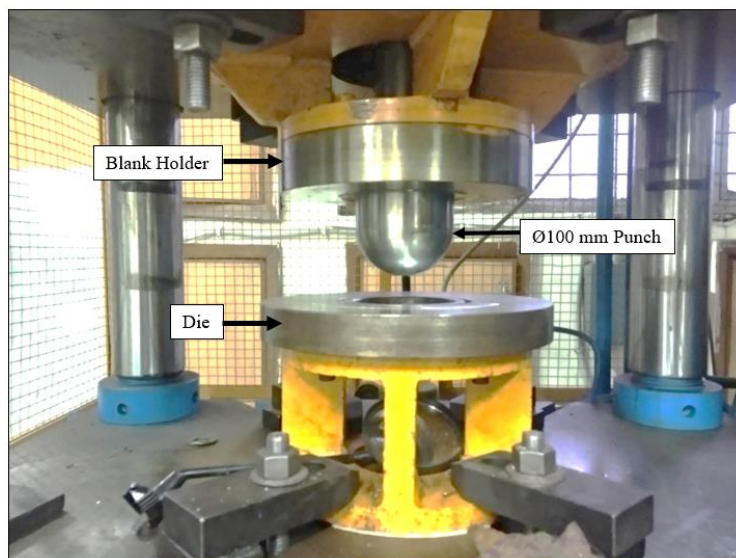


Figure 3.14 Punch-Die-Blank Holder setup in a 100 Ton hydraulic press

3.12.1 Stretch forming operation

Stretch forming operation was carried out in a 100 Ton hydraulic press (FLOWMAKE make). It comprises of photoelectric safety guard at front for safe access. Encoder is provided for the precise stroke measurement and stroke control. Encoder senses through PLC and analogue card and display in touch screen having a least count of 0.1 mm. Load cell for main cylinder is provided to sense the load through PLC and Analog card with Digital display of Load. The Least count is 0.01 Ton. Pressure transmitter is provided to sense the pressure of the main cylinder and blank holder cylinder through PLC and Analog card. At first the Blank Holder moves down and locks

down the sheet with Die. Then punch begins to move in downward direction and draw the sheet prior to fracture.

3.12.2 Dome height measurement of the formed sheets

Dome height of each and every specimen after forming was measured with the help of a Vernier height gauge. The Vernier calliper is having a least count of 0.01mm. the height of the dome was measured manually; care was taken to avoid the measurement errors.



Figure 3.15 Dome height measurement with the help of Vernier height gauge

3.13 SIMULATION OF THE STRETCH FORMING OPERATION

Simulation to check the formability of FSW-annealed and non-annealed sheet has been done on Abaqus/CAE 6.14-2 software. It is a Dassault system designed software to perform engineering tests based on numerical model.

3.14 MEASUREMENT OF THE MAJOR AND MINOR DIAMETER OF THE ELLIPSE AND FORMING LIMIT DIAGRAM

The major diameter and minor diameter of the deformed circle i.e. ellipse is measured with the help of a stereo microscope. The diameter of the circle was of 5mm. based on this initial dimension major and minor strain was measured. Then major strain and minor strain was plotted to get the Forming Limit Diagram.



Figure 3.16 Measurement of major and minor diameter of the ellipse

3.15 MODELLING OF BLANK AND DIE-PUNCH-HOLDER SETUP

Blank was modelled as 3D deformable Shell Planar and Punch, Die, and Blank Holder were designed as 3D discrete rigid. Sketcher tool was used to draw the required blank then blank was partitioned into three segments for AA5083, AA6082 and weld bead. Then materials were added to the software and assigned to the partitioned regions. Then all the parts were meshed with the help of mesh tool through seeding. The element type that was assigned to the blank is S4R (A 4-node doubly curved thin or thick shell, reduced integration, hourglass control, finite membrane strains). Then the parts were assembled as shown in figure 3.17.

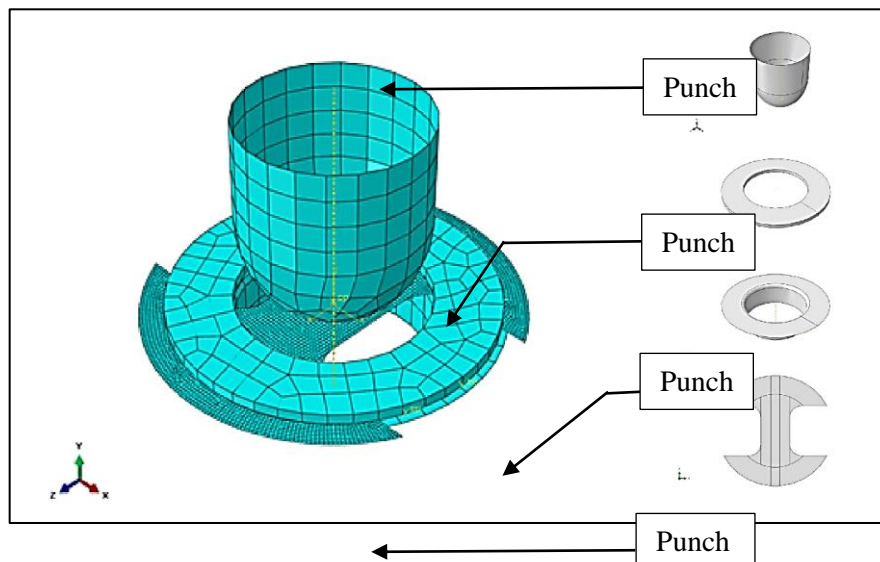


Figure 3.17 Assemble of the parts required for formability test

Dynamic, Explicit solver has been used to execute the simulation. Interaction properties were assigned between the interacting surfaces. The Boundary conditions were given to perform the test virtually.

CHAPTER 4

RESULT AND DISCUSSION

4.1 TENSILE PROPERTIES

AA5083 and AA6082 was selected for experimentation. Tensile specimens as per ASTM-E8M were prepared for the tensile testing. Specimens were cut from 230X230 mm sheet by wire-cut EDM technique. Uniaxial Tensile tests were performed in a 50KN Tensile testing machine. The results which were calculated from the raw data extracted from the machine output are further calculated and displayed sequentially.

Table-4.1 mechanical properties of AA5083-O

Orientation w.r.t. rolling direction (°)	Yield stress (MPa)	UTS (MPa)	% Elongation	Strain Hardening Exponent (n)	Strength coefficient (MPa) (K)
0	196	268	13.2	0.2304	357.95
0	207	262	14.4	0.2178	335.93
0	204	264	13.7	0.2145	334.39
45	176	233	14.4	0.2141	275.17
45	179	228	12.5	0.2222	312.87
45	191	244	12.8	0.2161	326.58
90	203	262	12.9	0.2373	357.21
90	179	238	14	0.2461	313.28
90	202	258	13.7	0.2026	319.13

Engineering Stress-Engineering strain and True Stress-True Strain Curve has been shown in Figure 4.1 and Figure 4.2 respectively.

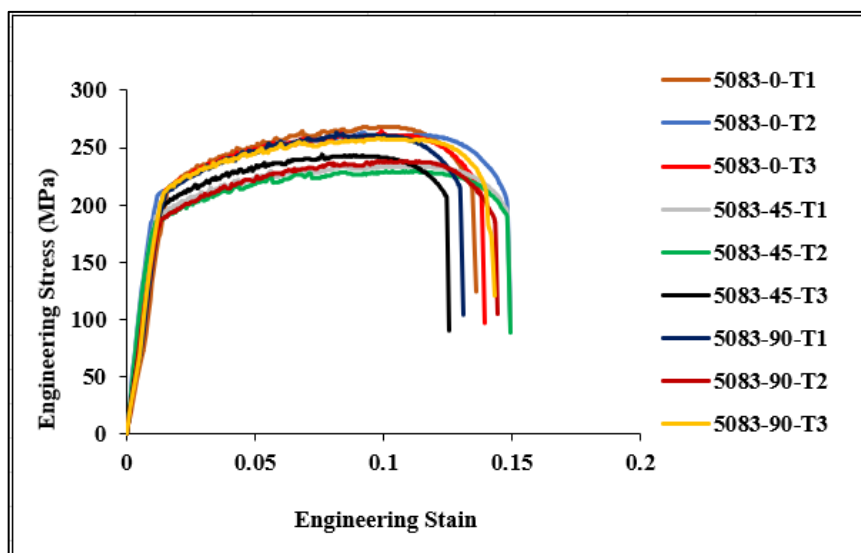


Figure 4.1 True Stress vs True Strain plot AA5083

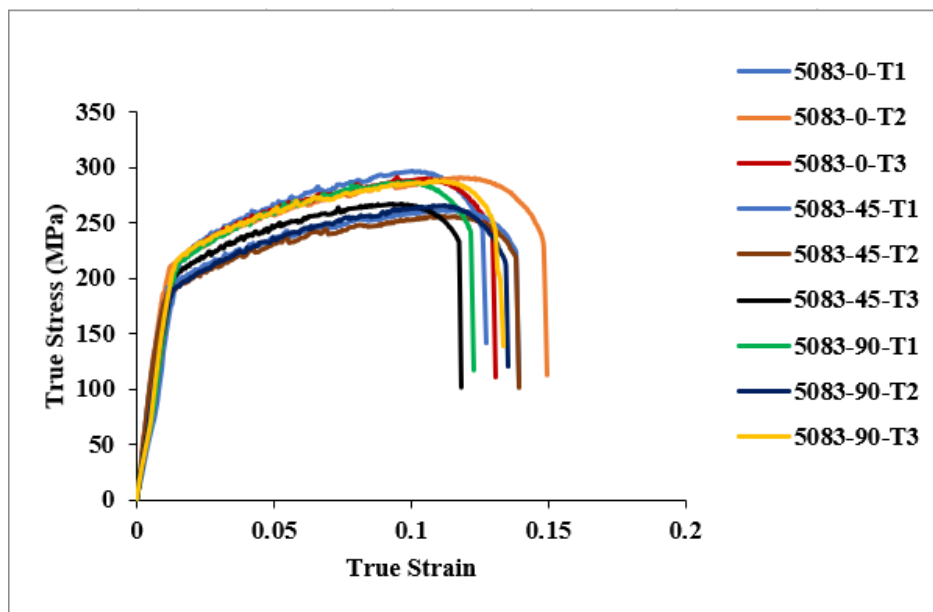


Figure 4.2 True Stress vs True Strain plot AA5083

Mechanical properties of Aluminium alloy 6082-T6 have been shown in Table-4.2. which shows yield stress, Ultimate Tensile Strength, % elongation, strain hardening exponent, and strength coefficient of the material. It shows maximum Ultimate Tensile Strength of 308 MPa at a 90° orientation with the rolling direction.

Table-4.2 mechanical properties of AA6082-T6

Orientation w.r.t. rolling direction (°)	Yield stress (MPa)	UTS (MPa)	% Elongation	Strain Hardening Exponent (n)	Strength coefficient (MPa) (K)
0	238	259	6.25	0.1496	429.8344
0	269	293	8.87	0.1708	501.6487
0	266	295	12.1	0.2628	666.0735
45	197	271	10	0.1532	430.2644
45	249	287	13.8	0.1621	461.6468
45	262	301	13.7	0.1521	472.5294
90	211	286	15.7	0.1575	454.1375
90	256	308	18.8	0.1661	497.7511
90	258	296	16.8	0.1345	448.7653

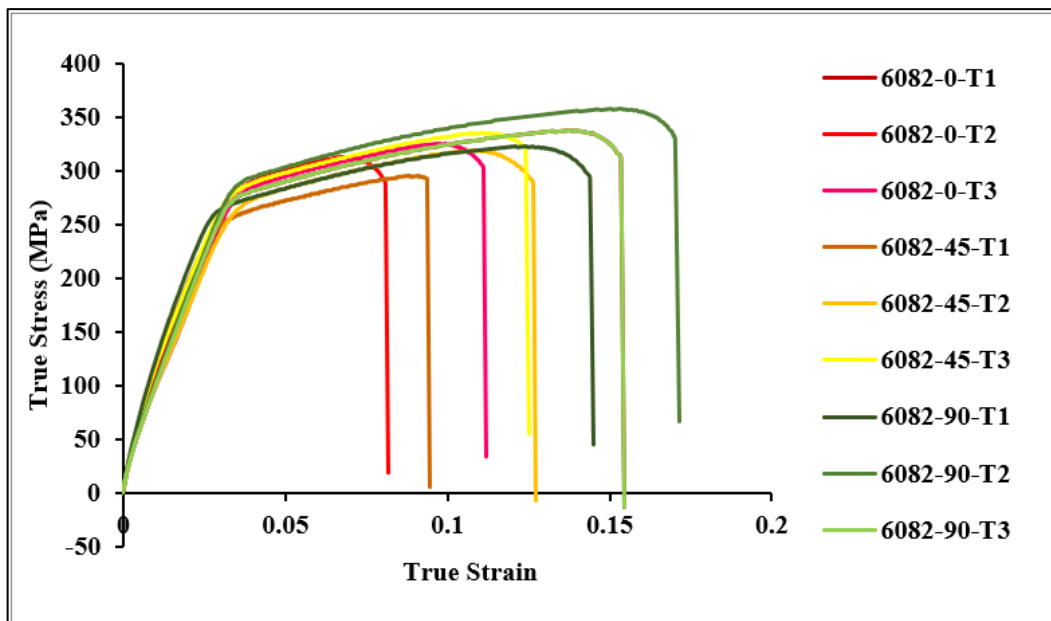


Figure 4.3 True Stress vs True Strain plot AA6082-T6

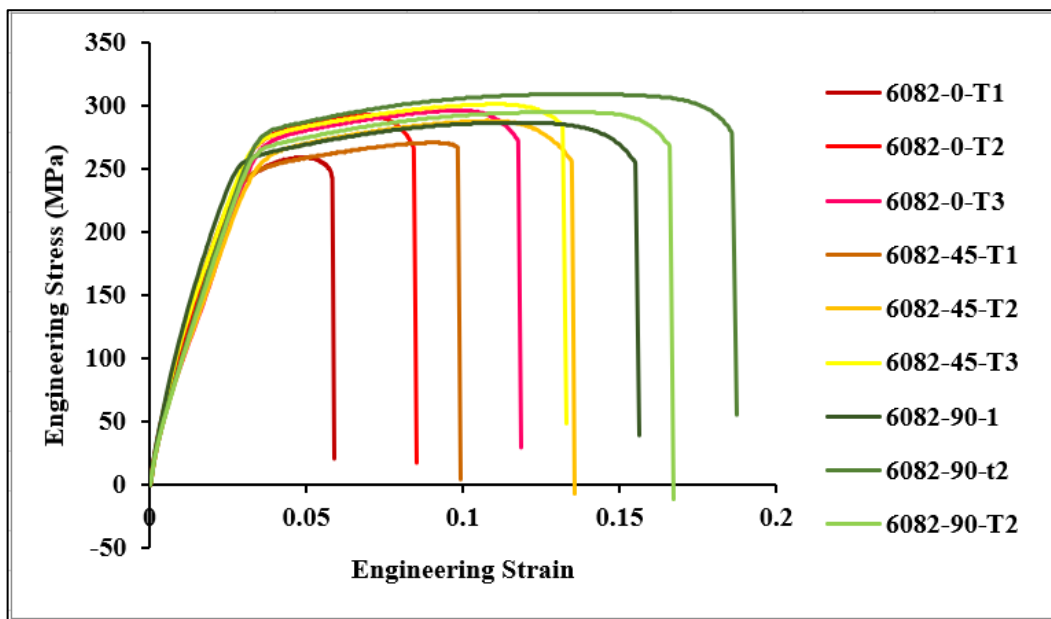


Figure 4.4 True Stress vs True Strain plot AA6082-T6

The mechanical properties for the Aluminium alloy 6082-T6 heat treated at different temperature have been shown below. Among which heat treatment at 300°C shows the optimum result for annealing. Annealing at 300°C shows an Ultimate tensile Strength of 139 MPa with yield stress of 8602 MPa and an elongation of 18.7%. True Stress-True Strain plots have been shown in Figure-4.3.

Table-4.3 mechanical properties of AA6082-T6 at different annealing temperature

Annealing Temperature (°C)	Yield stress (MPa)	UTS (MPa)	% Elongation	Strain Hardening Exponent (n)	Strength coefficient (MPa) (K)
150	225	295	15.5	0.1917	499.82
300	86.2	139	18.7	0.2255	259.95
350	85.1	114	40.8	0.246	205.696
350	75.4	120	18.7	0.2822	239.63
450	68.5	110	25.6	0.2151	190.05

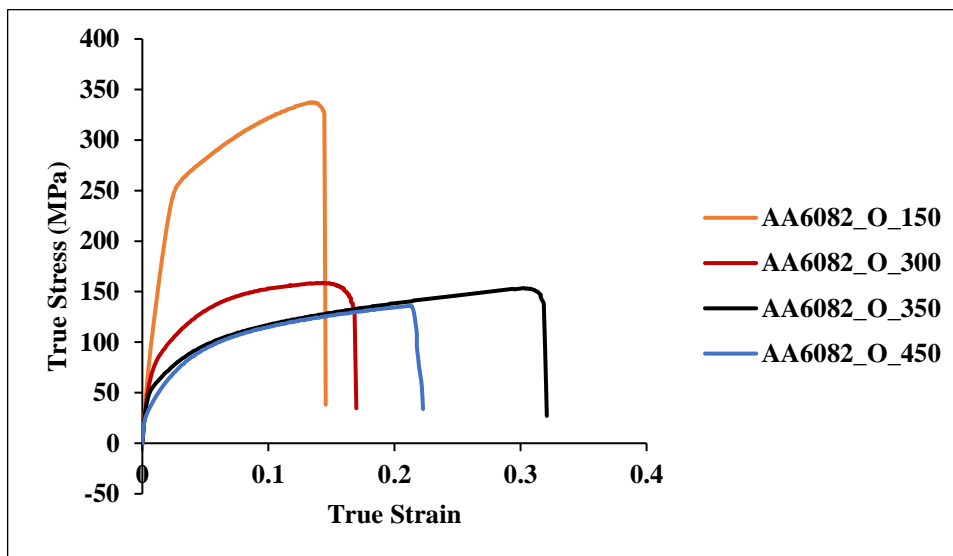


Figure 4.5 True Stress vs True Strain plot

Table -4.3 shows the mechanical properties of AA6082-T6 at different annealing temperature. The best fit to anneal AA6082-T6 sheet is 300°C. At 300°C proper combination of Ultimate Tensile Strength, Yield Strength and percentage elongation is achieved and annealing temperature for AA6082-T6 can be taken as 300°C as it provides best combination of mechanical properties.

4.2 RESIDUAL STRESS OF THE SHEET BEFORE AND AFTER ANNEALING

It is being observed that residual stress has been reduced after the annealing of the Friction Stir Welded sheets. Residual Stress distribution of the annealed and non-annealed sheets are shown in the Figure 4.6. light blue coloured row represents the residual stress of the welded sheet before annealing and yellow coloured row represents the residual stress after annealing. percentage change in residual stress after annealing operation is represented by white row.

Position		-19.5	-16.5	-13.5	-10.5	-7.5	-5	-2.5	0	2.5	5	7.5	10.5	13.5	16.5	19.5
Welded surface	Aluminium(311) 25°	-101	-113	-127	-118	-111	-124	-120	-133	-133	-176	-25	-87	-133	-174	-143
		-5	-4	-5	-4	-3	-29	0	-4	4	-28	12	-9	-12	14	-31
		95.0495	96.46018	96.06299	96.61017	97.2973	76.6129	100	96.99248	103.0075	84.09091	148	89.65517	90.97744	108.046	78.32168
back surface	Aluminium(311) 25°	-40	-30	-64	-57	-78	-119	-113	-84	-21	-31	-58	-141	-110	-54	-90
		-38	-14	-5	-12	-24	-25	-23	2	-3	6	-20	-69	-69	0	-96
		5	53.33333	92.1875	78.94737	69.23077	78.9916	79.64602	102.381	85.71429	119.3548	65.51724	51.06383	37.27273	100	-6.66667

Figure 4.6 Residual Stress measurement before and after the Friction Stir Welding

The position was taken 2.5mm apart from the centre line of the weld bead on both the sides up to 10.5 mm and 3mm apart onwards. The residual stresses were measured on [311] lattice plane of the sheet work piece. The average percentage change in the residual stress on the welded side is 97.15 MPa and 67.47 MPa on the reverse side. The major deformation took place on the welded side as a result of which annealing plays a major role to release the residual stress on the welded side. These values have been plotted in the graph shown in figure-x. where abbreviated terms are given below in Table-4.4.

Table 4.4 Nomenclature for the term used in Residual Stress plot

W_AA_311_RS	Welded surface in 311 plane Residual Stress
B_AA_311_RS	Welded surface in 311 plane Residual Stress
W_AA_311_RS_O	Welded surface in 311 plane Residual Stress
B_AA_311_RS_O	Welded surface in 311 plane Residual Stress

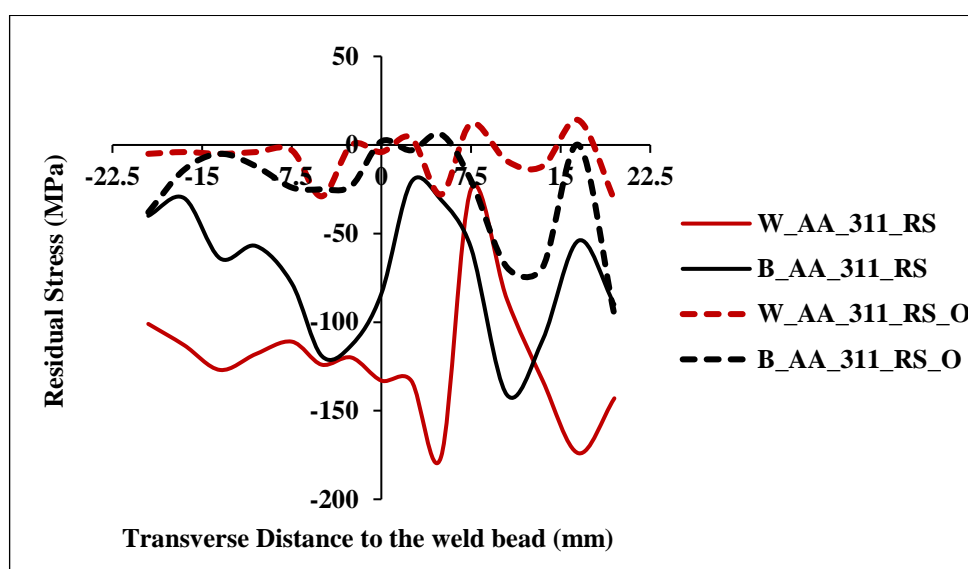


Figure 4.7 Residual Stress vs Transverse Distance to the weld bead

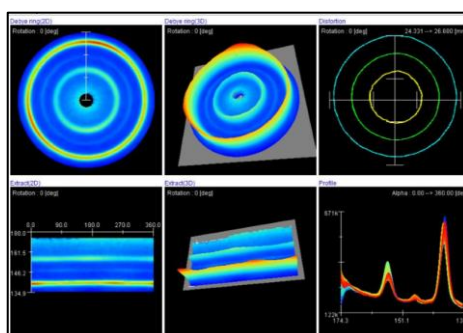


Figure 4.8 Debye ring mapping to evaluate residual stresses in the bend samples using Cosa

4.3 TAGUCHI ANALYSIS

Experimentally measured values of UTS, %Elongation (S) and %Elongation (I) have been shown in the Table 4.5

Table 4.5 Experimental Results for the Ultimate Tensile Strength, % Elongation (S) and % Elongation (I)

Experimental run	Ultimate tensile Strength	% Elongation (Longitudinal)	% Elongation (Transverse)
1	220	22.6	18.0
2	235	24.5	20.4
3	230	20.1	17.5
4	222	20.0	18.9
5	232	26.5	24.2
6	231	17.6	18.0
7	235	24.7	18.2
8	239	26.0	23.0
9	231	18.0	17.5

As per objective function (UTS, %Elongation (S) and %Elongation (I)) larger is Better control function was used to get the signal-to-noise ratio which has been shown in Table 4.6

Table 4.6 S/N ratio for different experimental run

Experimental run	S/N Ratio (dB) for UTS	S/N Ratio (dB) for % Elongation (S)	S/N Ratio (dB) for % Elongation (I)
1	46.8485	27.0822	25.1055
2	47.4214	27.7833	26.1926
3	47.2346	26.0639	24.8608
4	46.9271	26.0206	25.5292
5	47.3098	28.4649	27.6763
6	47.2722	24.9103	25.1055
7	47.4214	27.8539	25.2014
8	47.5680	28.2995	27.2346
9	47.2722	25.1055	24.8608

The average of the signal to noise ratios for UTS is shown in Table 4.7

Table 4.7 The average of the signal to noise ratios for UTS

Level	Tool Travel Speed		Tool Rotational Speed	
	Sum	Avg. S/N ratio	Sum	Avg. S/N ratio
1	141.49	47.16	141.20	47.06
2	141.51	47.17	142.30	47.43
3	142.26	47.42	141.78	47.26

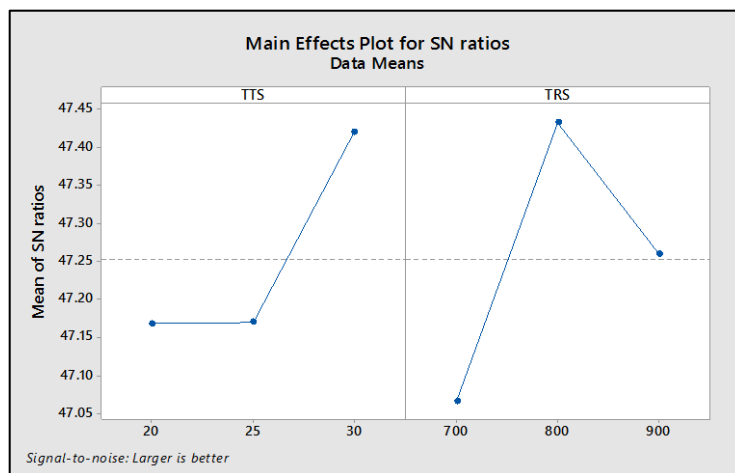


Figure 4.9 Graphical plot of mean of S/N ratios -TTS and TRS for UTS

The average of the signal to noise ratios for % Elongation (S) is shown in Table 4.8

Table 4.8 average of the signal to noise ratios for % Elongation (S)

Level	Tool Travel Speed		Tool Rotational Speed	
	Sum	Avg. S/N ratio	Sum	Avg. S/N ratio
1	80.94	26.98	80.97	26.99
2	79.41	26.47	84.54	28.18
3	81.27	27.09	76.08	25.36

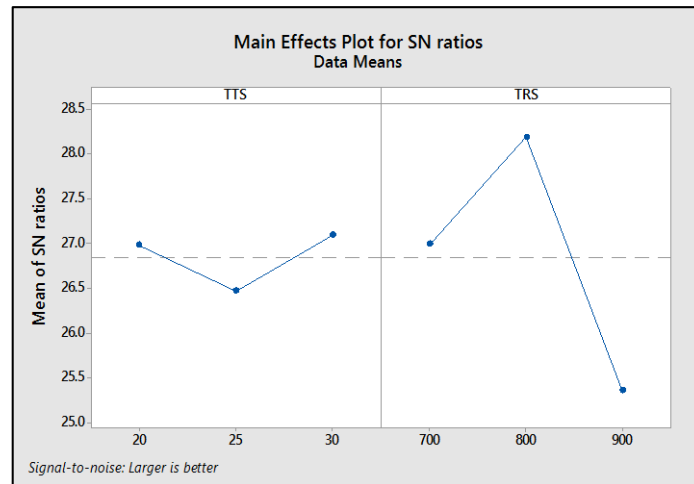


Figure 4.9 Graphical plot of mean of S/N ratios -TTS and TRS for % Elongation (S)

The average of the signal to noise ratios for % Elongation (I) is shown in Table 4.9

Table 4.9 The average of the signal to noise ratios for % Elongation (I)

Level	Tool Travel Speed		Tool Rotational Speed	
	Sum	Avg. S/N ratio	Sum	Avg. S/N ratio
1	76.17	25.39	75.84	25.28
2	78.30	26.10	81.09	27.03
3	77.31	25.77	74.82	24.94

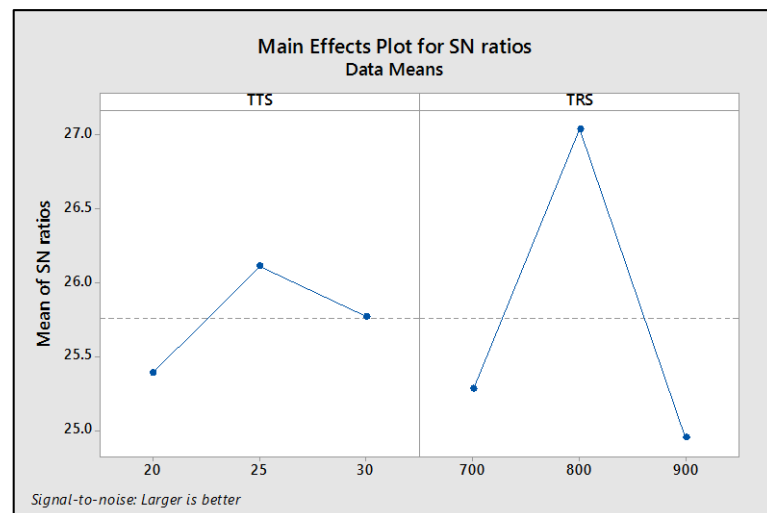


Figure 4.9 Graphical plot of mean of S/N ratios -TTS and TRS for % Elongation (I)

Optimum values of the Input parameters and their optimized values has been shown in Table 4.10

Table 4.10 Optimum values of the Input parameters and their optimized values

Input Parameter	Optimized value
Tool Travel Speed	30 mm/min
Tool Rotational Speed	800 RPM

4.4 ANOVA RESULTS

Analysis of Variance is used to calculate response data of each parameter in the Orthogonal Array experiment. Analysis of variance (**ANOVA**) is a collection of statistical models and their associated estimation procedures (such as the "variation" among and between groups) used to analyse the differences among group means in a sample.

4.4.1 Analysis of Variance

Table 4.11 Analysis of variance for TTS and TRS

Source	DF	Adj SS	Adj MS	F-Value	P-Value
TTS	2	4.516	2.2578	2.48	0.199
TRS	2	41.536	20.7678	22.79	0.007
Error	4	3.644	0.9111		
Total	8	49.696			

The maximum value of SN ratio has been selected to get the optimum mechanical properties.

Welding had been done at 800 rotational speed and 30 mm/min.

4.5 MICRO HARDNESS TESTING RESULT BEFORE ANNEALING OF WELDED SHEETS

Measurement of Hardness in HV0.5 scale has been shown in Figure-x which shows the measurement scale, dwell time for the testing and line mapping used during testing.


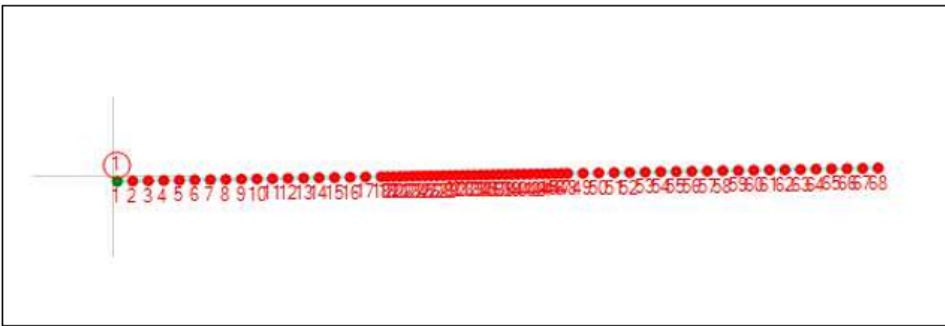
 DELHI TECHNOLOGICAL UNIVERSITY <small>formerly Delhi College of Engineering (under Delhi Act 9 of 2009, Govt. of NCT of Delhi)</small>		DTU Delhi
General Information		
Date	May 23, 2019	
Operator	admin	
Hardness tester type	DURAMIN-40 AC3	
Job Description		
Number	1/1	
Name	TEST	
FSW specimen, 68 points		
Hardness Test Information		
Method	VICKERS	
Hardness scale	HV0.05	
Dwell time	10 sec.	
Test Pattern		
		

Figure4 .10 Micro-hardness Testing report

The Micro-hardness number through line mapping has been plotted in Figure-4.10. the line mapping was done on the cross-section of the FSW sheet of a total length of 25 mm containing 5mm of AA5083, 15 mm weld bead and 5mm of AA6082. Form the graph it can be concluded that the hardness of AA5083-O used in FSW has a higher value of hardness as compare to AA6082-O. The hardness value for AA5083-O parent sheet up to 5 mm has an average value of 91 HV followed by a short lift while entering into the weld bead with an average of 95 HV. The centre region of the weld bead has the highest average hardness of 105 HV due to plastic deformation and interlocking of the material with a strain hardening. Again, the average value of hardness decreases while approaching towards AA6082-O with an average value of 70 HV till the end of the material. Hardness number was also checked after annealing of the welded sheet.

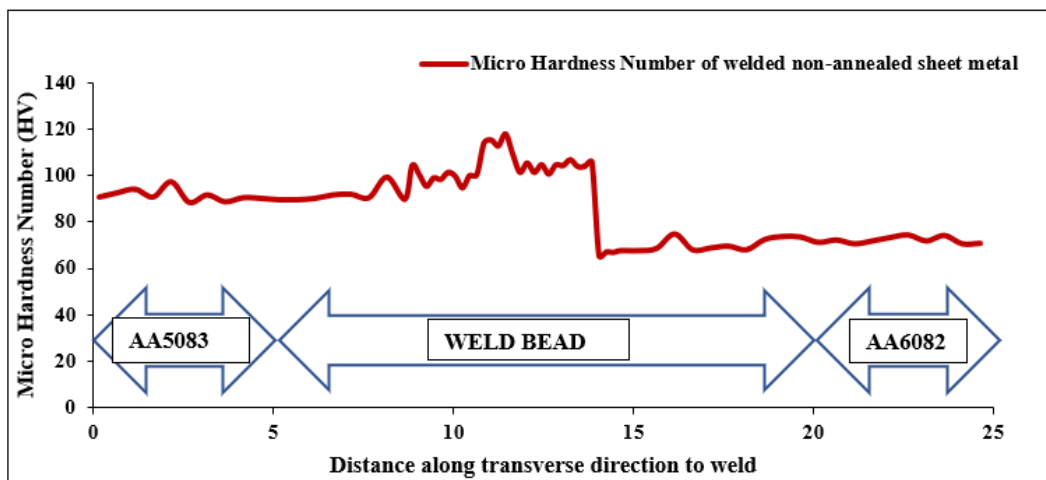


Figure 4.11 Hardness distribution on a cross-section of a Friction Stir Welded non-annealed sheet

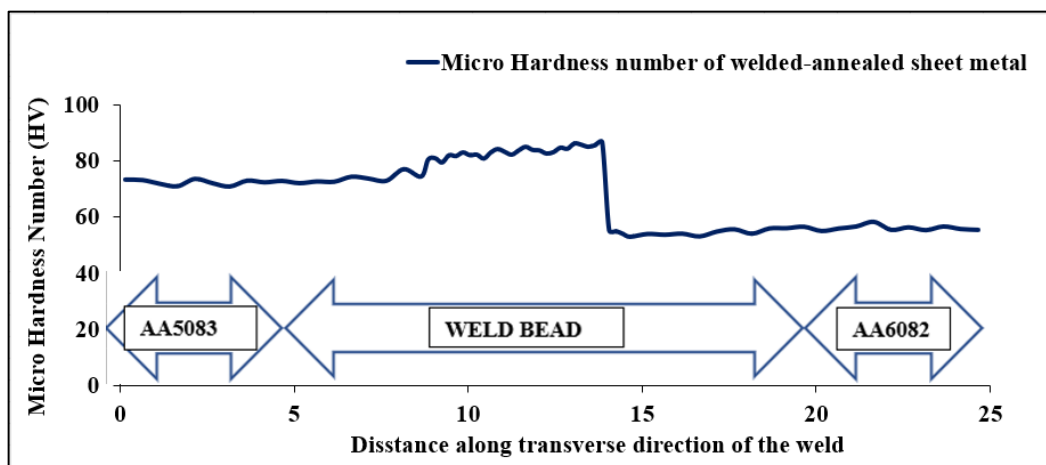


Figure 4.12 Hardness distribution on a cross-section of a Friction Stir Welded annealed sheet

Figure 4.11 shows the hardness data points plot for non-annealed welded sheet and Figure 4.12 shows the hardness data points plot for welded-annealed sheet. It is revealed that the hardness of the welded sheet has been decreased after annealing. Annealed-welded sheet has the average hardness value of 72 HV while entering from AA5083-O side and 74 HV inside the weld bead while approaching, 83 HV at the centre region and 54 HV in the AA6082-O.

4.6 MICROSTRUCTURE OF THE DIFFERENT PARTS OF THE FSW NON-ANNEALED SHEET

Microstructure of the Friction Stir Welded and non-Welded sheets have shown in consecutive Figures below.

4.6.1 Microstructure of the different parts of the FSW non-annealed sheet

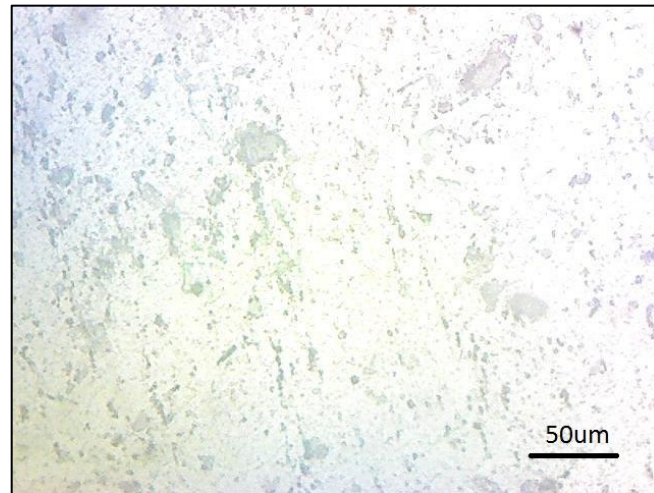


Figure 4.13 Microstructure of AA5083

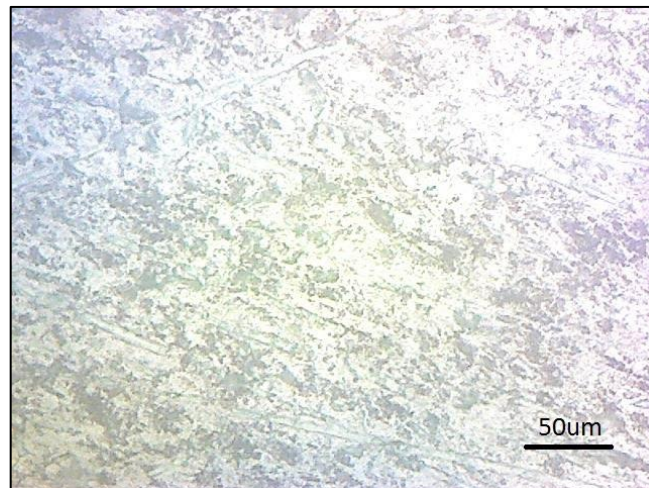


Figure 4.14 Microstructure of AA6082

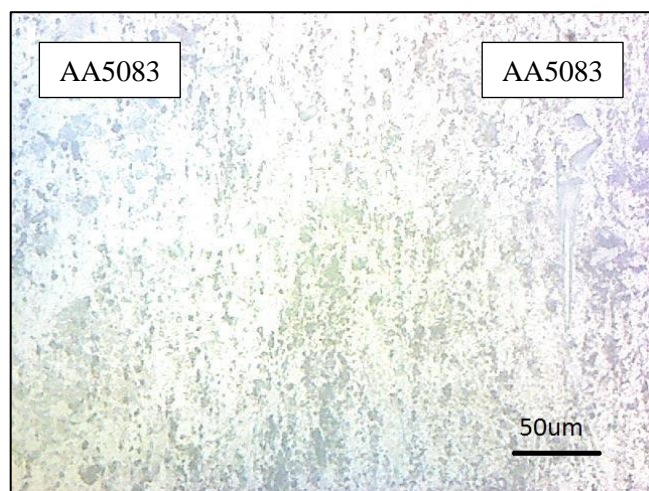


Figure 4.15 Microstructure of weld bead

4.6.2 Microstructure of the different parts of the FSW annealed sheet

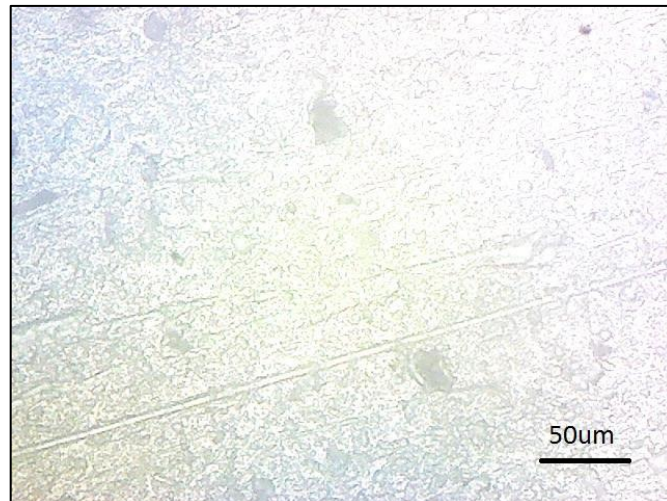


Figure 4.16 Microstructure of AA5083

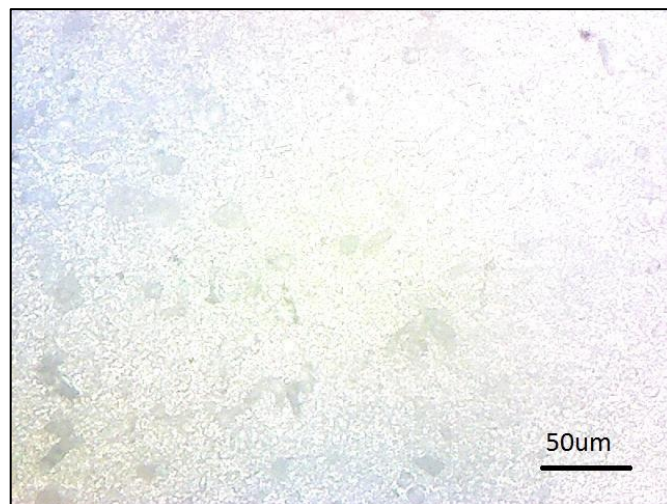


Figure 4.17 Microstructure of AA6082-O

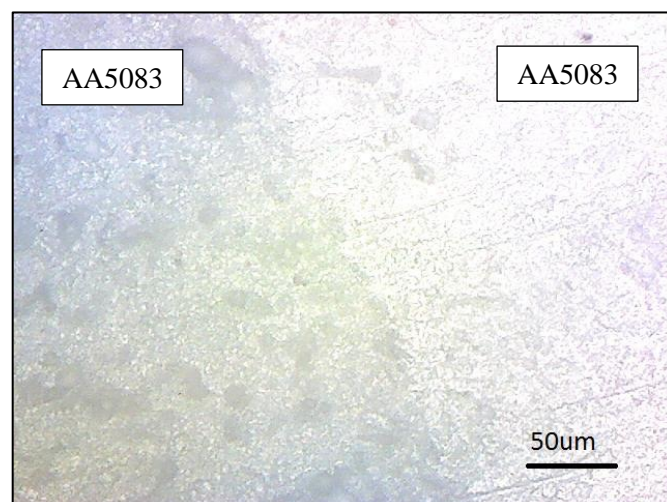


Figure 4.18 Microstructure of weld bead

4.7 FLD SAMPLE DOME HEIGHT

Dome height of the formed sample has been measured with the help of a vernier height gauge and the experimental values and the values from the FEA has been shown in table x. The percentage error between the Experimental and FEA also calculated and shown in the Table.4.12

Table 4.12 FLD Sample Dome height

FSW Annealed sheet			FSW Non-Annealed sheet		
Experimental	FEA	% Error	Experimental	FEA	% Error
21.9	22.19	1.324201	21.16	21.03	0.614367
21.74	21.76	0.091996	20.57	20.17	1.944579
21.43	20.33	5.132991	20.44	18.13	11.30137
20.68	18.3	11.5087	18	16.32	9.333333
17.32	15.8	8.775982	16.98	14.35	15.48881
19.32	17.5	9.42029	15.45	14	9.385113
18	15.74	12.55556	15.5	12.53	19.16129
20.04	19.72	1.596806	17.47	17.5	0.171723

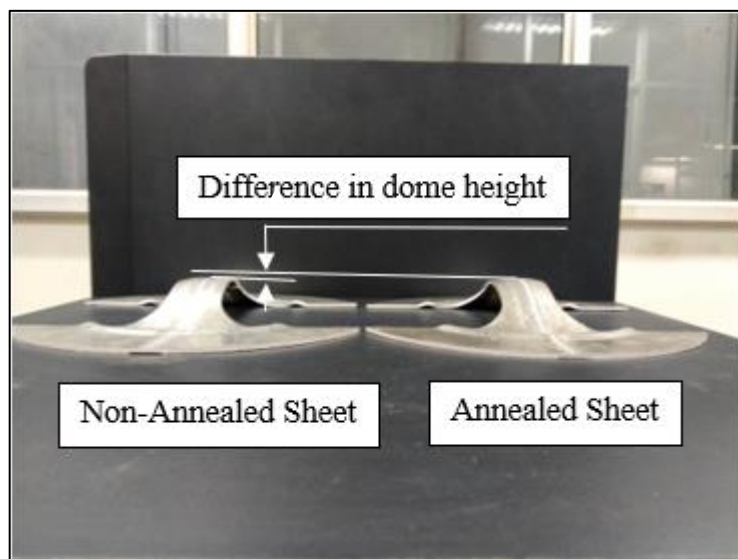


Figure 4.19 Sheet after forming operation

The experimental and FEA values of dome height has been shown in Figure 4.19 as column representation. It shows that sheet undergone annealing process has higher dome height as compare to the sheet which had not gone through annealing process.

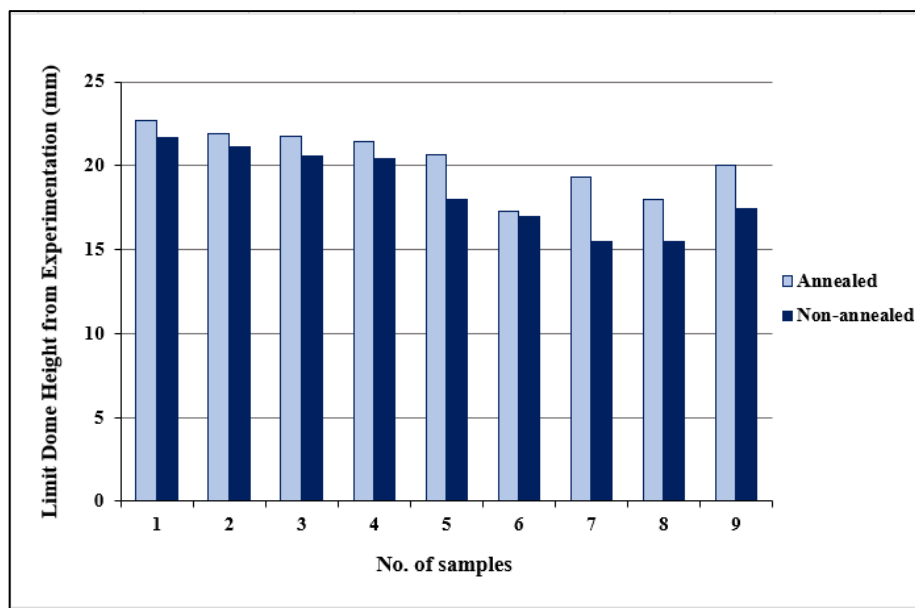


Figure 4.20. clustered column representation of the annealed and non-annealed sheets during experimentation

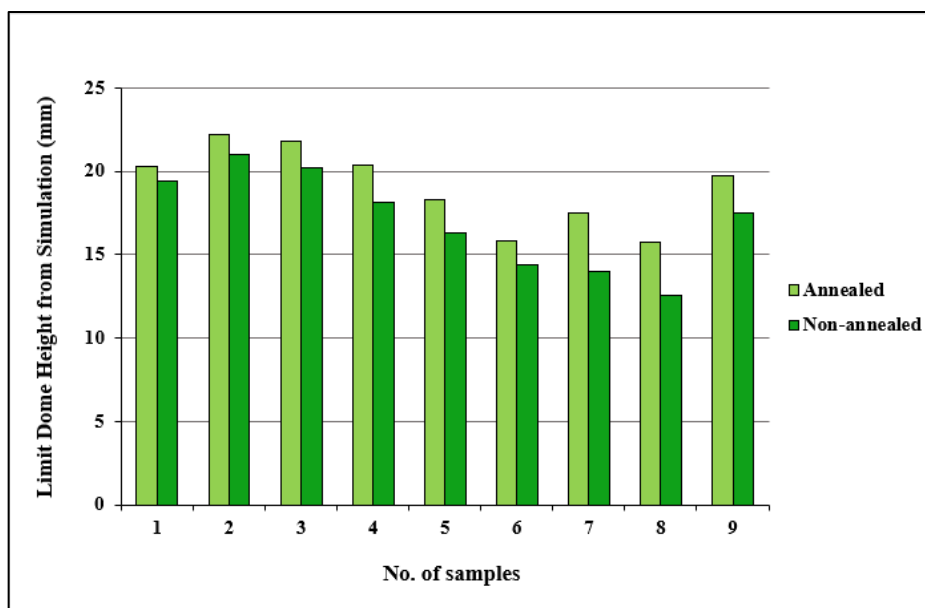


Figure 4.21. clustered column representation of the annealed and non-annealed sheets during FEA simulation

4.8 FORMABILITY OF ANNEALED AND NON-ANNEALED FSW SHEETS

Samples were tested at ambient temperature. Some samples were in non-annealed welded condition and rest are in the annealed condition. Welded sheets were annealed at 300°C with a 2hrs of soaking time. Both types of sheets were tested in a 100Ton hydraulic machine. The experimental result which has been noted down, plotted in Figure x and Figure-y. major and minor strains were measured at the same condition with the testing.

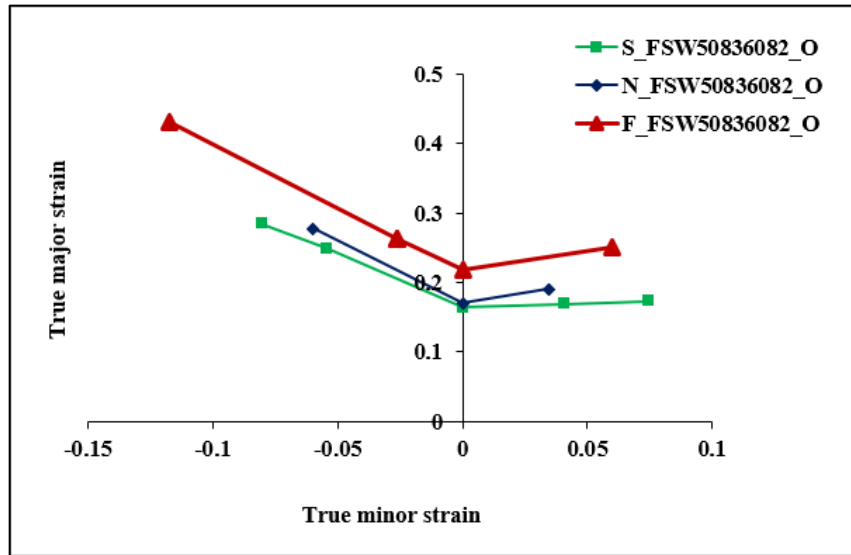


Figure 4.22. Forming limit Diagram of AA5083-O and AA6082-O annealed sheet

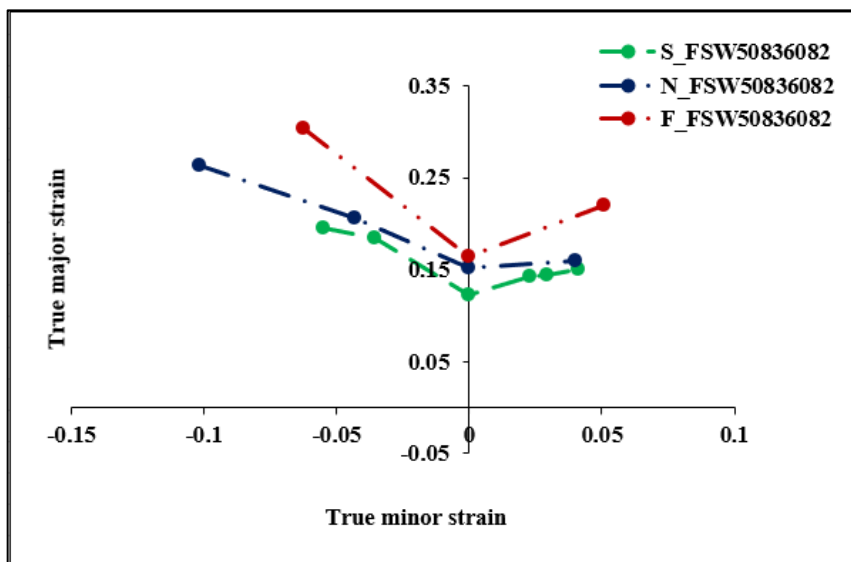


Figure 4.23 Forming limit Diagram of AA5083-O and AA6082-O non-annealed sheet

It has been also observed that, the formability of the annealed sheet has been increased as compare to the non-annealed sheet. After annealing FLD_0 reaches to 0.219 while non-annealed sheets having FLD_0 of 0.1634. FLD_0 is the value of minimum limit strain under plain strain condition (while minor strain becomes zero, i.e. the major strain axis). In all the cases plain strain condition

occurred in 60mm width sheet. The degree of biaxiality has been increased as indicated in the Figure 4.22 and Figure 4.23 by the higher minor limit strain value in both the sheets. Both the graphs for annealed and non-annealed sheets have been combined to get a clearer view regarding the enhancement of the formability after annealing of the Friction Stir Welded sheets, shown in Figure-4.24.

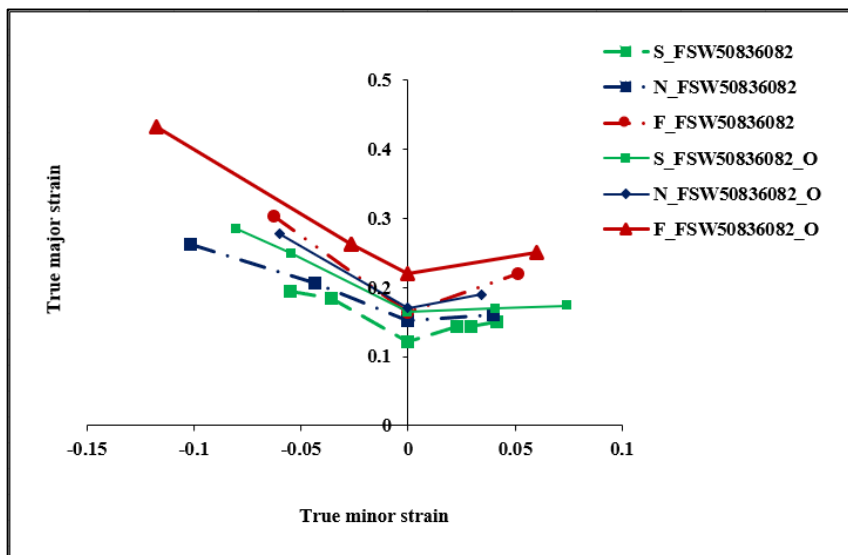


Figure 4.24 combined Forming limit Diagram of AA5083-O and AA6082-O

4.9 FEA RESULTS

Finite element analysis was carried out to predict the result. The scatter plot of the point prior to failure has been plotted down as shown in Figure x and Figure y for annealed and non-annealed sheets respectively. It has been observed that FEA result has a good agreement with the experimental result. Point lies above the experimentally calculated failure curve represents the failure condition, rest of the points in the below of the failure curve is in safe condition.

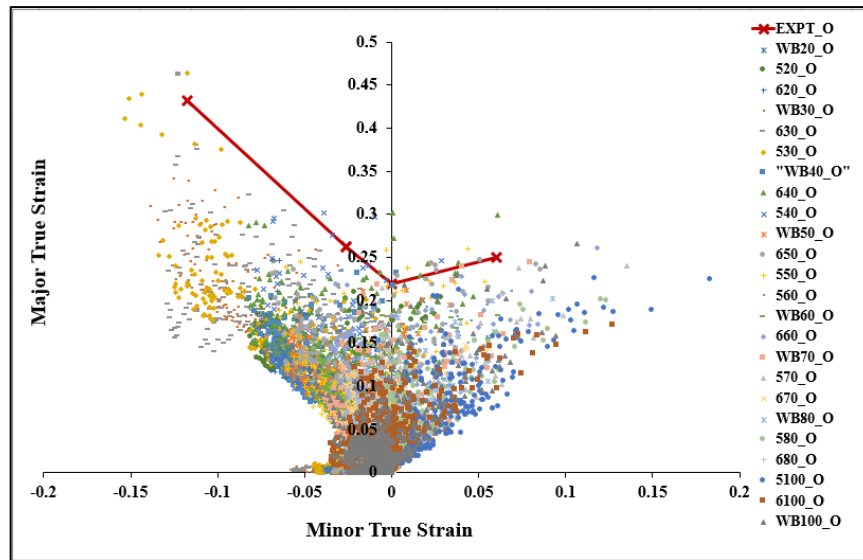


Figure 4.25. Forming limit Diagram of AA5083-O and AA6082-O after annealing

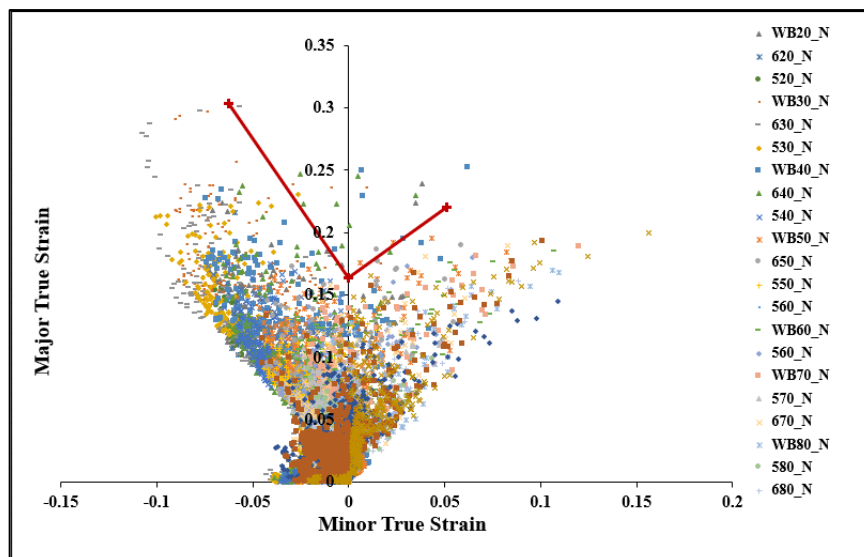


Figure 4.26. Forming limit Diagram of AA5083-O and AA6082-O before annealing

FEA results have been shown in the form of Max. In-Plane Strain, Min. In-Plane Strain and Von-Mises Stress distribution in the sheets. All the data points which have been extracted from the simulation have respective step time according to the experimental process. Distribution of data points have been shown with its respective FEA output.

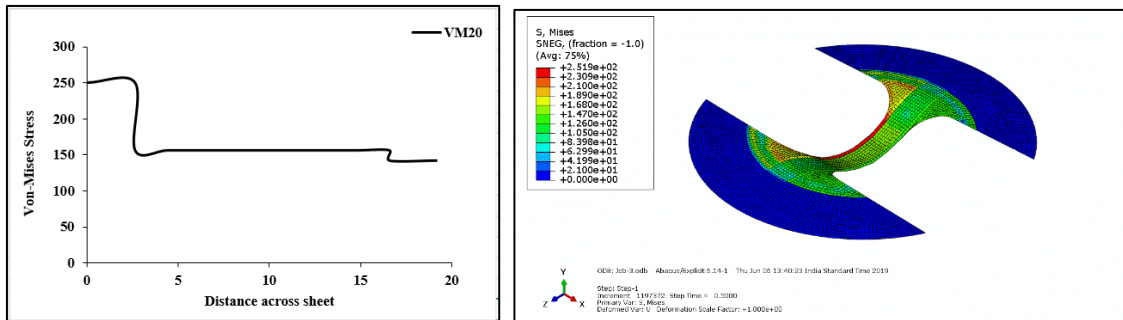


Figure 4.27 Variation of Von-Mises stress at different points across the width, (b) Contours of formed sheet for a punch profile radius of 100mm

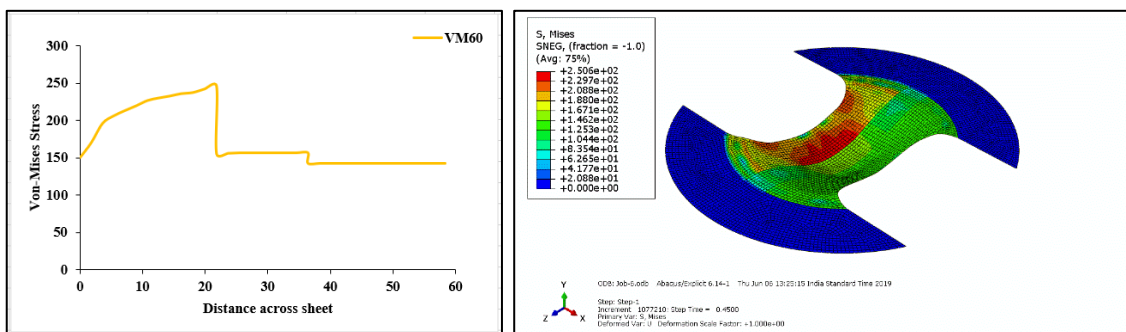


Figure 4.28 Variation of Von-Mises stress at different points across the width, (b) Contours of formed sheet for a punch profile radius of 100mm

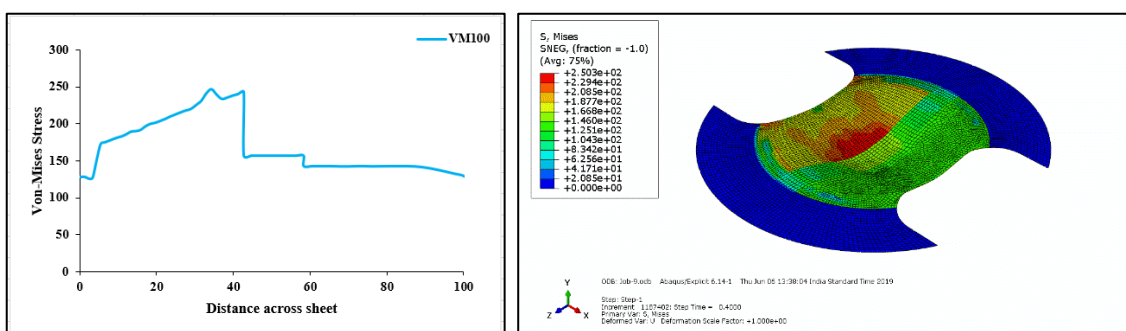


Figure 4.29 Variation of Von-Mises stress at different points across the width, (b) Contours of formed sheet for a punch profile radius of 100mm

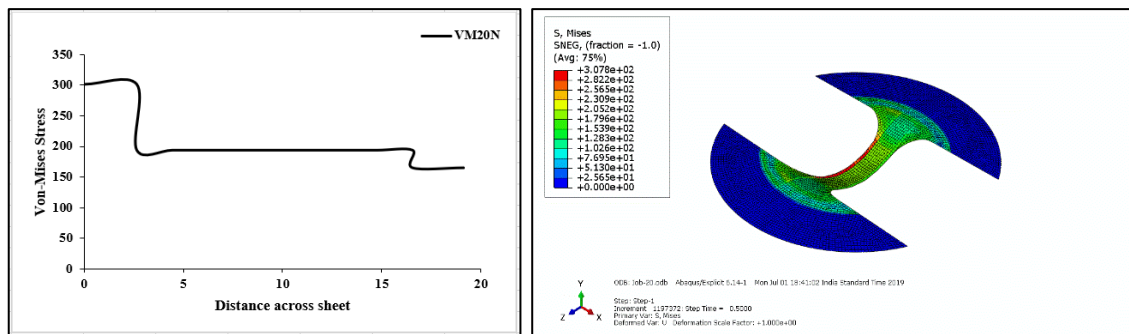


Figure 4.30 Variation of Von-Mises stress at different points across the width, (b) Contours of formed sheet for a punch profile radius of 100mm

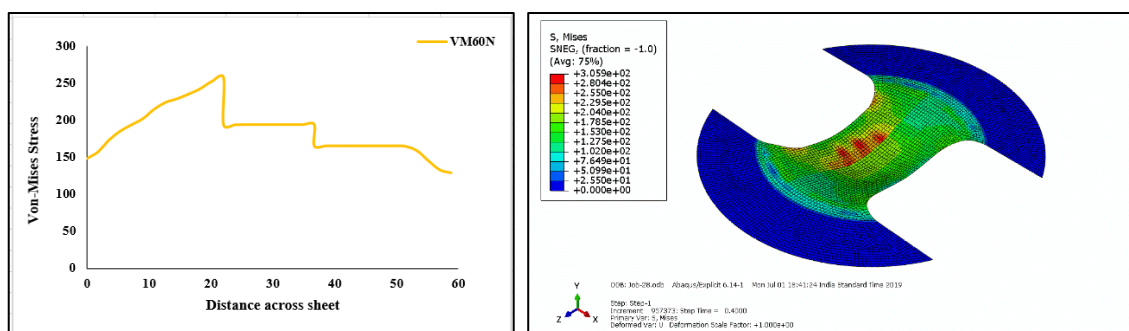


Figure 4.31 Variation of Von-Mises stress at different points across the width, (b) Contours of formed sheet for a punch profile radius of 100mm

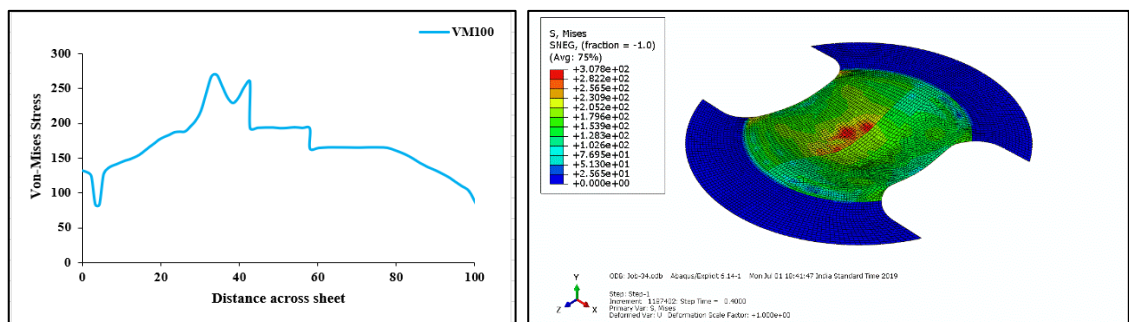


Figure 4.32 Variation of Von-Mises stress at different points across the width, (b) Contours of formed sheet for a punch profile radius of 100mm

Von-Mises Stress-Distance across sheet plot shows that each and every case for both annealed and non-annealed sheets, AA5083 has the higher stress value as compared to AA6082 and the value of stress generated inside the material is higher in case of non-annealed sheets as compared

to annealed sheets. As dome height for the annealed sheets are higher than that of the non-annealed sheets, it implies annealed sheets have more formability than a non-annealed one along with a lower stress value. The following figure shows the Max. In-Plane Principal Strain distribution and Min. In-Plane Principal Strain distribution across the width of the sheets.

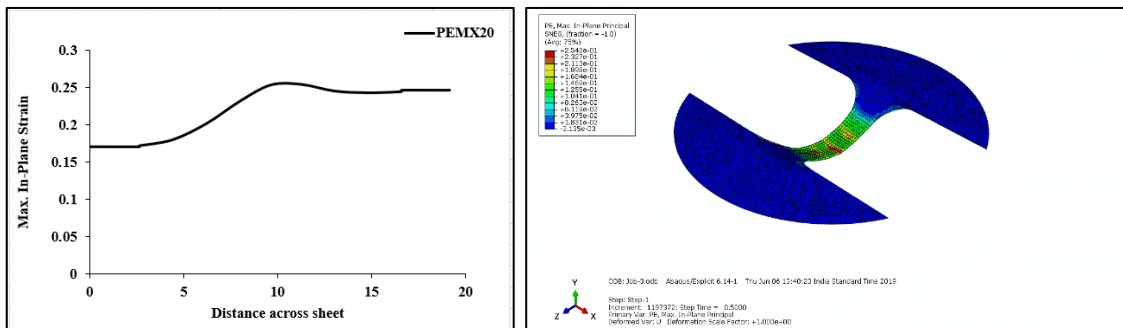


Figure 4.33 Variation of Max. In-Plane Strain at different points across the width, (b) Contours of formed sheet for a punch profile radius of 100mm

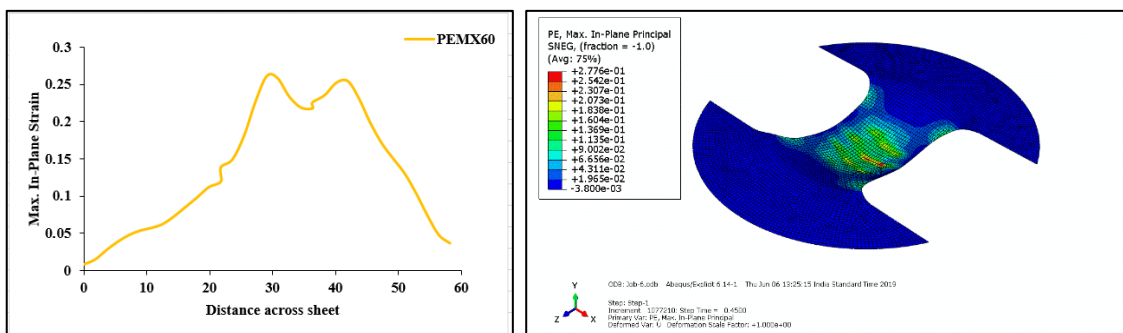


Figure 4.34 Variation of Max. In-Plane Strain at different points across the width, (b) Contours of formed sheet for a punch profile radius of 100mm

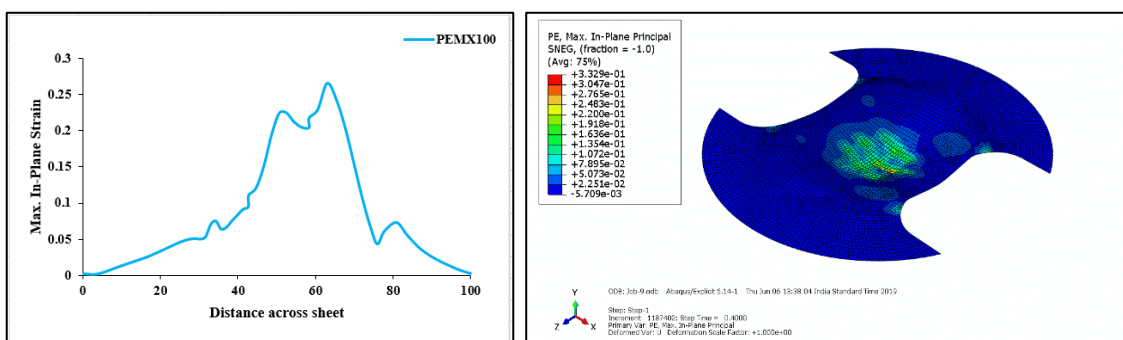


Figure 4.35 Variation of Max. In-Plane Strain at different points across the width, (b) Contours of formed sheet for a punch profile radius of 100mm

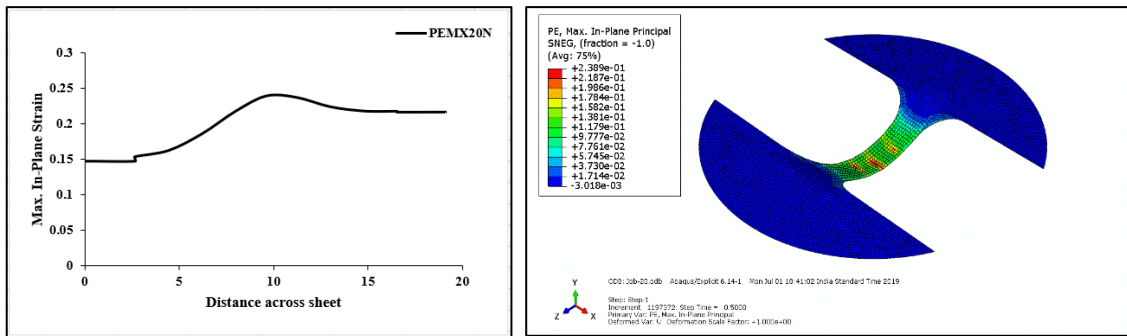


Figure 4.36 Variation of Max. In-Plane Strain at different points across the width, (b) Contours of formed sheet for a punch profile radius of 100mm

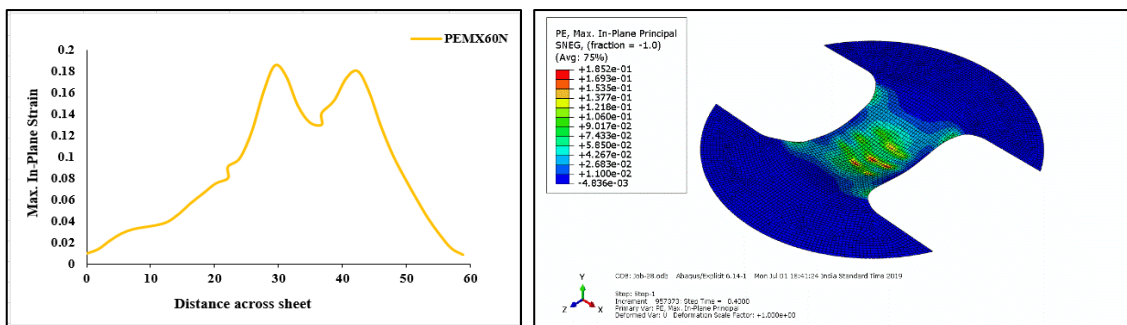


Figure 4.37 Variation of Max. In-Plane Strain at different points across the width, (b) Contours of formed sheet for a punch profile radius of 100mm

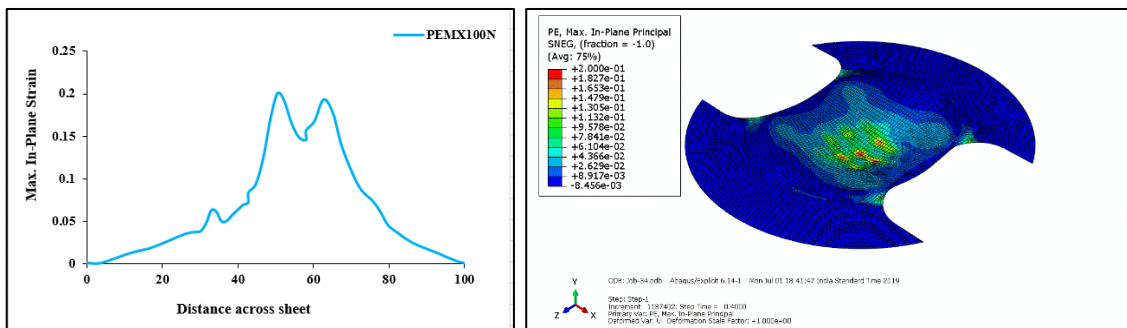


Figure 4.38 Variation of Max. In-Plane Strain at different points across the width, (b) Contours of formed sheet for a punch profile radius of 100mm

FEA representation shows that failure initiates from the right-hand side of the sheet (Side in the positive “X” axis direction.). As right-hand side of the sheet contains AA6082, a softer material, prediction of failure initiation worked properly. Max. In-Plane Principal Strain-Distance across sheet shows that maximum strain occurs at the centre position of the sheet below the punch.

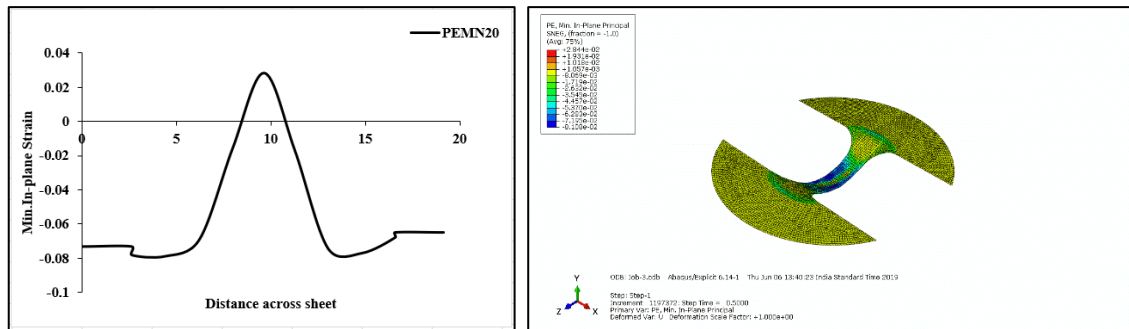


Figure 4.39 Variation of Min. In-Plane Strain at different points across the width, (b) Contours of formed sheet for a punch profile radius of 100mm

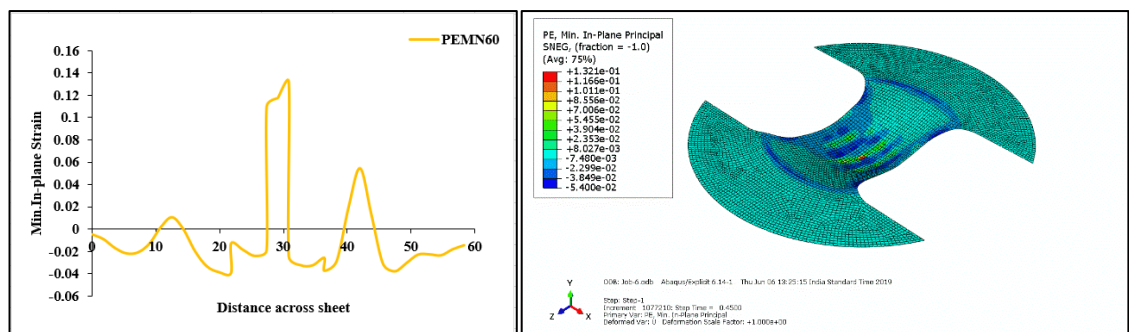


Figure 4.40 Variation of Min. In-Plane Strain at different points across the width, (b) Contours of formed sheet for a punch profile radius of 100mm

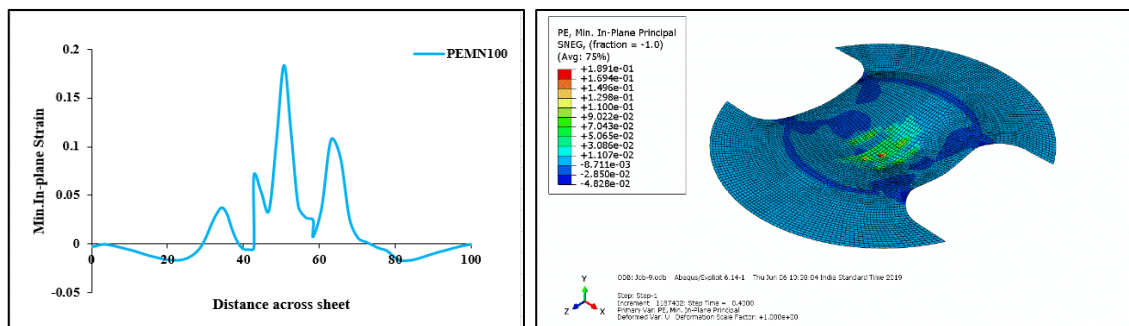


Figure 4.41 Variation of Min. In-Plane Strain at different points across the width, (b) Contours of formed sheet for a punch profile radius of 100mm

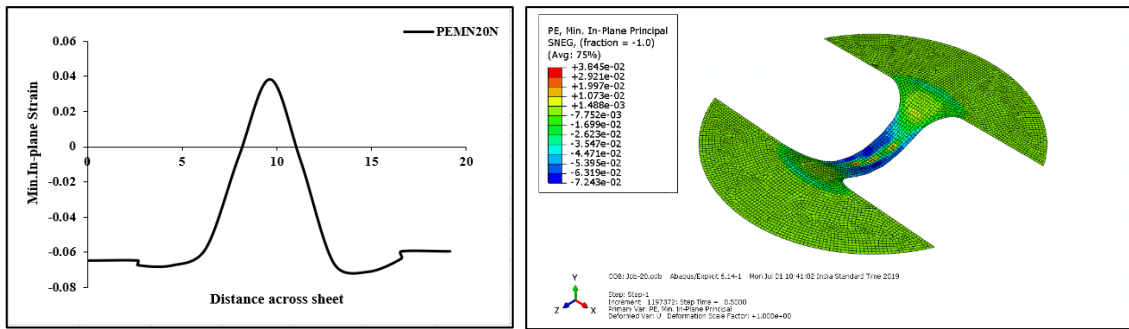


Figure 4.42 Variation of Min. In-Plane Strain at different points across the width, (b) Contours of formed sheet for a punch profile radius of 100mm

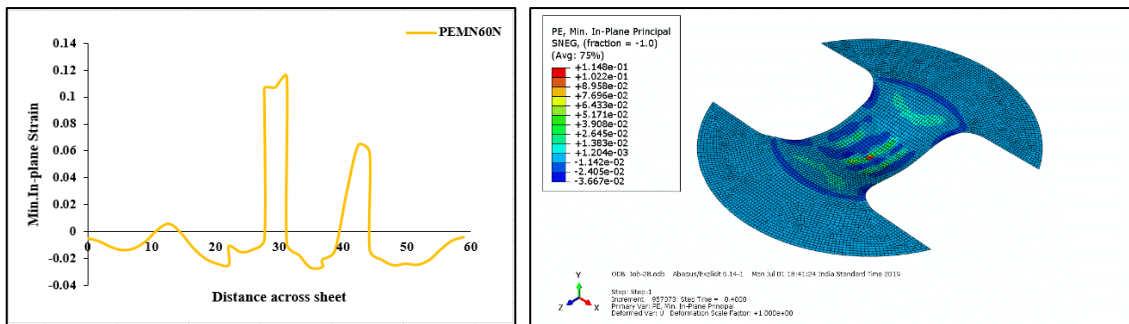


Figure 4.43 Variation of Min. In-Plane Strain at different points across the width, (b) Contours of formed sheet for a punch profile radius of 100mm

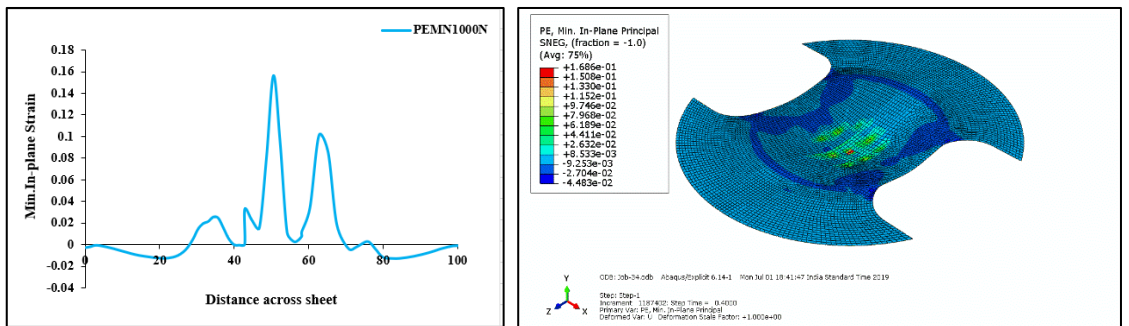


Figure 4.44 Variation of Min. In-Plane Strain at different points across the width, (b) Contours of formed sheet for a punch profile radius of 100mm

Min. In-Plane Principal Strain-Distance across sheet shows that maximum strain occurs at the centre position of the sheet below the punch.

CHAPTER 5

CONCLUSIONS

The present study is based on the investigations on the formability of Tailor Welded Blanks prepared by Friction Stir Welding process. The conclusions which can be drawn from the study are discussed below:

1. Two parent materials AA5083-O and AA6082-T6 were procured. Here AA6082-T6 has the higher strength as compared to AA5083. But after annealing of the AA6082-T6 its strength becomes less than that of AA5083-O.
2. Hardness of the Tailor Welded Blank varies across the sheets. For FSW-non-annealed sheets as well as for annealed one hardness can be represented by decreasing order as Weld bead>AA5083>AA6082. Where FSW-annealed sheet has higher hardness than no-annealed one across the sheet respectively.
3. Residual stress was reduced after annealing of the Friction Stir Welded sheets after annealing. It proves that recovery had been taken inside the welded sheet and reaches to the X-axis.
4. It has been observed that Forming Limit Strains and FLD_0 both are higher in case of FSW-annealed sheets as compare to FSW-non-annealed sheets. Experimental plot depicts that the Forming Limit Curve for FSW-annealed sheets lies above the FLC of FSW-non-annealed sheets.
5. Max. In-Plane Principal and Min. In-plane principal strain increases from the left-hand side to right-hand side seen from the top view. Where LHS contains AA5083-O, a stronger material and RHS contains a softer material AA6082-O.
6. Failure also occurs from the AA6082-O containing region of the drawn sheet which makes sure that strains are higher in the softer material allowing for a partial larger draw limit.
7. Dome height of the FSW-annealed specimen was found to be higher than that of the FSW-non-annealed specimen. It means the material gets stretched more after annealing of the sheets.
8. Experimental and FEA results show a good agreement with each other with having a maximum error of 12.55% in only one case.
9. From the forming limit diagram it can be shown that FEA scatter plot obeys the experimental curve with having few points beyond the failure curve.

10. Von-Mises Stress is higher in case of FSW-non-annealed sheet as compare to FSW-annealed sheet. The stress value is higher in the AA5083 region of the blank than the AA6082. Stress value decreases with the increase of the width.

REFERENCES

- [1] V. Gautam, V. M. Raut, and D. R. Kumar, “Analytical prediction of springback in bending of tailor-welded blanks incorporating effect of anisotropy and weld zone properties,” *Proc. Inst. Mech. Eng. Part L J. Mater. Des. Appl.*, vol. 232, no. 4, pp. 294–306, 2018.
- [2] H. Wallentowitz, R. Dögl, J. Leyers, and T. Parr, “and their Effects on the Automotive Industry,” vol. 105, pp. 24–25, 2003.
- [3] R. S. Mishra and Z. Y. Ma, “Friction stir welding and processing,” *Mater. Sci. Eng. R Reports*, vol. 50, no. 1–2, pp. 1–78, 2005.
- [4] N. Zaman, A. Noor, Z. A. Khan, and A. K. Mukhopadhyay, “Mechanical and microstructural behavior of friction stir welded similar and dissimilar sheets of AA2219 and AA7475 aluminium alloys,” *J. Alloys Compd.*, vol. 695, pp. 2902–2908, 2017.
- [5] E. A. El-danaf and M. M. El-rayes, “Microstructure and mechanical properties of friction stir welded 6082 AA in as welded and post weld heat treated conditions,” *Mater. Des.*, vol. 46, pp. 561–572, 2013.
- [6] D. Avula, R. Kumar, and R. Singh, “Effect of Friction Stir Welding on Microstructural and Mechanical Properties of Copper Alloy,” *World Acad. Sci. Eng. Technol.*, vol. 74, no. February, pp. 214–223, 2011.
- [7] H. Hayashi and T. Nakagawa, “Recent trends in sheet metals and their formability in manufacturing automotive panels,” vol. 46, pp. 455–487, 1994.
- [8] R. W. Davies, G. J. Grant, H. E. Oliver, M. A. Khaleel, and M. T. Smith, “Forming-Limit Diagrams of Aluminum Tailor-Welded Blank Weld Material,” vol. 32, no. February, 2001.
- [9] M. Merklein, M. Johannes, M. Lechner, and A. Kuppert, “Journal of Materials Processing Technology A review on tailored blanks — Production , applications and evaluation,” *J. Mater. Process. Tech.*, vol. 214, no. 2, pp. 151–164, 2014.
- [10] “X + 182,” p. 436, 1993.
- [11] M. . Paridah, A. Moradbak, A. . Mohamed, F. abdulwahab taiwo Owolabi, M. Asniza, and S. H. . Abdul Khalid, “We are IntechOpen , the world ’ s leading publisher of Open Access books Built by scientists , for scientists TOP 1 %,” *Intech*, vol. i, no. tourism, p. 13, 2016.

- [12] G. Mrówka-Nowotnik and J. Sieniawski, "Influence of heat treatment on the microstructure and mechanical properties of 6005 and 6082 aluminium alloys," *J. Mater. Process. Technol.*, vol. 162–163, no. SPEC. ISS., pp. 367–372, 2005.
- [13] H. Wang, P. A. Colegrove, and J. F. Dos Santos, "Numerical investigation of the tool contact condition during friction stir welding of aerospace aluminium alloy," *Comput. Mater. Sci.*, vol. 71, pp. 101–108, 2013.
- [14] Y. J. Chao, X. Qi, and W. Tang, "Heat Transfer in Friction Stir Welding—Experimental and Numerical Studies," *J. Manuf. Sci. Eng.*, vol. 125, no. 1, p. 138, 2003.
- [15] L. Dubourg *et al.*, "Design and properties of FSW tools : a literature review 1- Introduction 2 . Fundamental principles of Friction Stir Welding."
- [16] T. Watanabe, H. Takayama, and A. Yanagisawa, "Joining of aluminum alloy to steel by friction stir welding," *J. Mater. Process. Technol.*, vol. 178, no. 1–3, pp. 342–349, 2006.
- [17] M. M. El-rayes and E. A. El-danaf, "Journal of Materials Processing Technology The influence of multi-pass friction stir processing on the microstructural and mechanical properties of Aluminum Alloy 6082," *J. Mater. Process. Tech.*, vol. 212, no. 5, pp. 1157–1168, 2012.
- [18] M. Guerra, C. Schmidt, J. C. McClure, L. E. Murr, and A. C. Nunes, "Flow patterns during friction stir welding," *Mater. Charact.*, vol. 49, no. 2, pp. 95–101, 2002.
- [19] J. A. Schneider and A. C. Nunes, "Characterization of plastic flow and resulting microtextures in a friction stir weld," *Metall. Mater. Trans. B Process Metall. Mater. Process. Sci.*, vol. 35, no. 4, pp. 777–783, 2004.
- [20] P. Heurtier, M. J. Jones, C. Desrayaud, J. H. Driver, F. Montheillet, and D. Allehaux, "Mechanical and thermal modelling of Friction Stir Welding," *J. Mater. Process. Technol.*, vol. 171, no. 3, pp. 348–357, 2006.
- [21] A. Scialpi, L. A. C. De Filippis, and P. Cavaliere, "Materials & Design Influence of shoulder geometry on microstructure and mechanical properties of friction stir welded 6082 aluminium alloy," vol. 28, pp. 1124–1129, 2007.
- [22] K. Kumar and S. V. Kailas, "The role of friction stir welding tool on material flow and weld formation," *Mater. Sci. Eng. A*, vol. 485, no. 1–2, pp. 367–374, 2008.
- [23] L. H. Shah, S. Walbridge, and A. Gerlich, "Tool eccentricity in friction stir welding: a comprehensive review," *Sci. Technol. Weld. Join.*, vol. 0, no. 0, pp. 1–13, 2019.
- [24] Y. N. Zhang, X. Cao, S. Larose, and P. Wanjara, "Review of tools for friction stir

- welding and processing,” *Can. Metall. Q.*, vol. 51, no. 3, pp. 250–261, 2012.
- [25] D. G. Hattingh, C. Blignault, T. I. van Niekerk, and M. N. James, “Characterization of the influences of FSW tool geometry on welding forces and weld tensile strength using an instrumented tool,” *J. Mater. Process. Technol.*, vol. 203, no. 1–3, pp. 46–57, 2008.
- [26] G. M. D. Cantin, S. A. David, W. M. Thomas, E. Lara-Curzio, and S. S. Babu, “Friction Skew-stir welding of lap joints in 5083–0 aluminium,” *Sci. Technol. Weld. Join.*, vol. 10, no. 3, pp. 268–280, 2005.
- [27] M. Merklein and J. Herrmann, “Effect of a local laser heat treatment on the formability of multi-layered 6000 series aluminum alloys,” *Phys. Procedia*, vol. 83, pp. 560–567, 2016.
- [28] R. Narayanasamy, R. Ponalagusamy, and S. Raghuraman, “The effect of strain rate sensitivity on theoretical prediction of limiting draw ratio for cylindrical cup drawing process,” *Mater. Des.*, vol. 29, no. 4, pp. 884–890, 2008.
- [29] F. Stachowicz, “Formability of aluminium-alloy sheets,” *J. Mech. Work. Technol.*, vol. 13, no. 2, pp. 229–235, 1986.
- [30] P. E. Smith and D. Lee, “SAE TECHNICAL Determination of Forming Limits for Aluminum Alloys,” no. 724, 2018.
- [31] A. Steuwer, M. J. Peel, and P. J. Withers, “Dissimilar friction stir welds in AA5083 – AA6082 : The effect of process parameters on residual stress,” vol. 441, pp. 187–196, 2006.
- [32] T. Yoshida, K. Hashimoto, T. Katayama, and Y. Kuriyama, “Shape control techniques for high strength steel in sheet metal forming,” *Nippon Steel Tech. Rep.*, no. 88, pp. 27–32, 2003.
- [33] “Submitted for publication in ICRS-6 Proceedings,” no. 1, 2000.
- [34] H. Strength, “Stir of High Strength Alloys by Friction Aluminum Welding,” vol. 40, 2000.
- [35] L. Svensson, L. Karlsson, H. Larsson, B. Karlsson, M. Fazzini, and J. Karlsson, “Microstructure and mechanical properties of friction stir welded aluminium alloys with special reference to AA 5083 and AA 6082,” vol. 5, no. 5, pp. 285–296, 2000.
- [36] T. Publications and F. U. Berlin, “No Title,” vol. 402, pp. 1671–1676, 2002.
- [37] J. K. Paik and A. Duran, “Ultimate Strength of Aluminum Plates and Stiffened Panels

- for Marine Applications,” vol. 41, no. 3, pp. 108–121, 2004.
- [38] M. W. Mahoney, C. G. Rhodes, J. G. Flintoff, R. A. Spurling, and W. H. Bingel, “Properties of Friction-Stir-Welded 7075 T651 Aluminum,” vol. 29, no. July, 1998.
- [39] “No Title,” vol. 402, pp. 1543–1548, 2002.
- [40] M. Peel, A. Steuwer, M. Preuss, and P. J. Withers, “Microstructure , mechanical properties and residual stresses as a function of welding speed in aluminium AA5083 friction stir welds,” vol. 51, pp. 4791–4801, 2003.
- [41] L. Reg, “Mechanical properties of friction stir welded aluminum alloys 5083,” 2013.
- [42] P. Measurement, “Proceedings of the Institution of Mechanical Engineers , Part B : Journal of Engineering Manufacture Friction stir welding of AA6082-T6 T-joints : process,” 2006.
- [43] P. Cavaliere, A. Squillace, and F. Panella, “Effect of welding parameters on mechanical and microstructural properties of AA6082 joints,” vol. 0, pp. 364–372, 2007.
- [44] M. P. Miles, D. W. Melton, and T. W. Nelson, “Formability of Friction-Stir-Welded Dissimilar-Aluminum- Alloy Sheets,” vol. 36, no. December, 2005.
- [45] Z. Feng, X.-L. Wang, S. A. David, and P. S. Sklad, “Modelling of residual stresses and property distributions in friction stir welds of aluminium alloy 6061-T6,” *Sci. Technol. Weld. Join.*, vol. 12, no. 4, pp. 348–356, 2007.
- [46] M. Han, S. Lee, J. Park, S. Ko, Y. Woo, and S. Kim, “Optimum condition by mechanical characteristic evaluation in friction stir welding for 5083-O Al alloy,” *Trans. Nonferrous Met. Soc. China*, vol. 19, pp. s17–s22, 2009.
- [47] J. Liu, M. Tan, A. Jarfors, Y. Aue-u-lan, and S. Castagne, “Formability in AA5083 and AA6061 alloys for light weight applications,” *Mater. Des.*, vol. 31, pp. S66–S70, 2010.
- [48] P. F. Bariani, S. Bruschi, A. Ghiotti, and F. Michieletto, “CIRP Annals - Manufacturing Technology Hot stamping of AA5083 aluminium alloy sheets,” *CIRP Ann. - Manuf. Technol.*, vol. 62, no. 1, pp. 251–254, 2013.
- [49] J. Liu, M. Tan, and Y. Aue-u-lan, “Superplastic-like forming of non-superplastic AA5083 combined with mechanical pre-forming,” pp. 123–129, 2011.
- [50] D. E. Cipoletti, A. F. Bower, Y. Qi, and P. E. Krajewski, “The influence of heterogeneity in grain boundary sliding resistance on the constitutive behavior of AA5083 during high-

- temperature deformation,” vol. 504, pp. 175–182, 2009.
- [51] C. Zhang, L. Leotoing, D. Guines, and E. Ragneau, “Theoretical and numerical study of strain rate influence on AA5083 formability,” vol. 9, pp. 3849–3858, 2008.
- [52] M. Simoncini, M. Cabibbo, and A. Forcellese, “Development of double-side friction stir welding to improve post-welding formability of joints in AA6082 aluminium alloy,” vol. 230, no. 5, pp. 807–817, 2016.
- [53] K. S. S. Kumar and A. C. Reddy, “DIE LESS SINGLE POINT INCREMENTAL FORMING PROCESS OF AA6082 SHEET METAL TO DRAW PARABOLIC CUPS USING ABAQUS,” pp. 127–134.
- [54] N. Li, M. S. Mohamed, J. Cai, J. Lin, D. Balint, and T. A. Dean, “Experimental and Numerical Studies on the Formability of Materials in Hot Stamping and Cold Die Quenching Processes,” vol. 1561, pp. 1555–1561, 2011.
- [55] X. Luan, O. El, H. Gao, J. Liu, and L. Wang, “Formability of AA6082-T6 at Warm and Hot Stamping Conditions,” vol. 716, pp. 107–113, 2016.
- [56] J. Liu, H. Gao, O. El Fakir, L. Wang, and J. Lin, “HFQ forming of AA6082 tailor welded blanks,” vol. 05006, 2015.
- [57] M. S. Mohamed, A. D. Foster, J. Lin, D. S. Balint, and T. A. Dean, “International Journal of Machine Tools & Manufacture Investigation of deformation and failure features in hot stamping of AA6082 : Experimentation and modelling,” *Int. J. Mach. Tools Manuf.*, vol. 53, no. 1, pp. 27–38, 2012.
- [58] M. J. F. Marques, “Study of 5083 aluminum alloy for shipbuilding industry after contamination , surface preparation and organic coatings application,” no. January, pp. 0–1, 2014.
- [59] A. Priyadarshini and C. I. Sancheti, “Comparative study of forgeability of as extrude aa6082 and as cast aa6082 alloy,” no. October, pp. 1–6, 2015.
- [60] S. Kumar, S. Kumar, and A. Kumar, “Optimization of process parameters for friction stir welding of joining A6061 and A6082 alloys by Taguchi method,” vol. 227, no. 6, pp. 1150–1163, 2012.